AN ANALYTICAL APPROACH FOR DETERMINATION OF OPTIMAL STATOR/ROTOR SALIENCY NUMBER OF A SWITCHED RELUCTANCE MOTOR

A THESIS SUBMITTED TO
THE GRADUATE SCHOOL OF NATURAL AND APPLIED SCIENCES
OF
MIDDLE EAST TECHNICAL UNIVERSITY

BY

CEM ERKAN KILINÇ

IN PARTIAL FULFILLMENT OF THE REQUIREMENTS
FOR
THE DEGREE OF MASTER OF SCIENCE
IN
ELECTRICAL AND ELECTRONICS ENGINEERING

JANUARY 2020

Approval of the thesis:

AN ANALYTICAL APPROACH FOR DETERMINATION OF OPTIMAL STATOR/ROTOR SALIENCY NUMBER OF A SWITCHED RELUCTANCE MOTOR

submitted by **CEM ERKAN KILINÇ** in partial fulfillment of the requirements for the degree of **Master of Science in Electrical and Electronics Engineering Department, Middle East Technical University** by,

Prof. Dr. Halil Kalıpçılar
Dean, Graduate School of **Natural and Applied Sciences** _____

Prof. Dr. İlkay Ulusoy
Head of Department, **Electrical and Electronics Eng.** _____

Assist. Prof. Dr. Emine Bostancı
Supervisor, **Electrical and Electronics Eng., METU** _____

Prof. Dr. H. Bülent Ertan
Co-Supervisor, **Electrical and Electronics Eng., Atılım University** _____

Examining Committee Members:

Prof. Dr. H. Bülent Ertan
Electrical and Electronics Engineering Dept., Atılım University _____

Assist. Prof. Dr. Emine Bostancı
Electrical and Electronics Eng., METU _____

Prof. Dr. Kemal Leblebicioğlu
Electrical and Electronics Engineering Dept., METU _____

Assist. Prof. Dr. Ozan Keysan
Electrical and Electronics Engineering Dept., METU _____

Prof. Dr. Güngör Bal
Electrical and Electronics Engineering Dept., Gazi University _____

Date: 19.01.2020

I hereby declare that all information in this document has been obtained and presented in accordance with academic rules and ethical conduct. I also declare that, as required by these rules and conduct, I have fully cited and referenced all material and results that are not original to this work.

Name, Surname: Cem Erkan Kılınç

Signature:

ABSTRACT

AN ANALYTICAL APPROACH FOR DETERMINATION OF OPTIMAL STATOR/ROTOR SALIENCY NUMBER OF A SWITCHED RELUCTANCE MOTOR

Kılınç, Cem Erkan
Master of Science, Electrical and Electronics Engineering
Supervisor: Assist. Prof. Dr. Emine Bostancı
Co-Supervisor: Prof. Dr. H. Bülent Ertan

January 2020, 140 pages

The purpose of this study is to seek the optimal stator and rotor saliency number of a switched reluctance motor (SRM) for hybrid electrical vehicle (HEV) applications.

For this purpose, first a previously developed SRM analysis software is investigated to identify possible errors in implementation of both the theory and the coding. Performance prediction method is based on the use of normalized force and permeance data produced via numerical field solution, and a polynomial based interpolation is introduced in the software. This approach is shown to produce accurate results through the comparison of predicted and measured results for the torque-position-current and flux linkage-current-position characteristics.

A detailed user interface has been developed for simulations. Once the study on the software is completed, its performance prediction (such as static torque-position, flux linkage-current, average torque, etc.) accuracy is tested through the comparison of the simulation results and measurements of two different SRMs, which are found to be in good agreement.

Finally, this software is embedded in an optimization procedure based on genetic algorithm to seek the optimal stator (N_s) and rotor (N_r) saliency numbers. The objective function of the optimization is defined as the maximum average torque attainable within specified dimensions. Optimization is done for different allowable pole combinations. Obtained results indicate that increasing N_s/N_r ratio above 18/12 does not yield any torque density improvement for the specified problem. It is also found that about 10 percent improvement in torque density is possible over the motor currently used in this HEV application.

Keywords: Switched Reluctance Motor, Performance Calculation, Design Optimization, Pole Combination

ÖZ

ANAHTARLAMALI RELÜKTANS MOTORUN OPTİMAL STATOR/ROTOR KUTUP SAYISINI BELİRLEMEK İÇİN ANALİTİK BİR YAKLAŞIM

Kılınç, Cem Erkan
Yüksek Lisans, Elektrik ve Elektronik Mühendisliği
Tez Danışmanı: Dr. Öğr. Üyesi Emine Bostancı
Ortak Tez Danışmanı: Prof. Dr. H. Bülent Ertan

Ocak 2020, 140 sayfa

Bu çalışmanın amacı, hibrit elektrikli araç uygulamaları için anahtarlamalı relüktans motorun (ARM) optimal stator ve rotor kutup sayısını araştırmaktır.

Bu amaçla, öncelikle teorinin ve kodlamanın uygulanmasındaki olası hataları belirlemek için daha önce geliştirilmiş bir ARM analiz yazılımı incelenmiştir. Performans tahmin yöntemi, sayısal alan çözümü ile üretilen normalize edilmiş bir kutbu bağlayan akı ve kuvvet verilerinin kullanımına dayanmaktadır ve yazılımda polinom tabanlı bir interpolasyon benimsenmiştir. Bu yaklaşımın öngörülen ve ölçülen sonuçların tork-pozisyon-akım ve bağlayan akı-akım-pozisyon karakteristiklerinin karşılaştırılmasıyla doğru sonuçlar ürettiği gösterilmiştir.

Simülasyonlar için detaylı bir kullanıcı arayüzü oluşturulmuştur. Yazılım üzerinde çalışma tamamlandığında, performans tahmininin (statik tork-konum, bağlayan akı-akım, ortalama tork vb.) doğruluğu, simülasyon sonuçlarının iki farklı ARM üzerinde yapılan deney sonuçlarıyla karşılaştırılmasıyla test edilmiştir ve sonuçların tutarlı olduğu tespit edilmiştir.

Son olarak, bu yazılım optimum stator (N_s) ve rotor (N_r) kutup sayılarını belirlemek için genetik algoritmaya dayanan bir optimizasyona yerleştirilmiştir. Optimizasyonun amaç işlevi, belirtilen boyutlar içerisinde elde edilebilecek maksimum ortalama tork olarak tanımlanmıştır. Optimizasyon, izin verilen farklı kutup kombinasyonları için yapılmıştır. Elde edilen sonuçlar kutup oranının 18/12'nin üzerine artmasının belirtilen problem için herhangi bir tork yoğunluğu artışı sağlamadığını göstermektedir. Ayrıca, bu hibrit elektrikli araç uygulamasında halihazırda kullanılan motora göre tork yoğunluğunda yaklaşık yüzde onluk bir iyileşmenin mümkün olduğu bulunmuştur.

Anahtar Kelimeler: Anahtarlamalı Relüktans Motoru, Performans Hesaplaması, Dizayn Optimizasyonu, Kutup Kombinasyonu

To my loving family and supporting friends

ACKNOWLEDGEMENTS

First of all, I would like to give my deepest and most sincere thanks to my supervisor, Assist. Prof. Dr. Emine Bostancı and my co-advisor, Prof. Dr. H. Bülent Ertan, for being there for me and backing me up at my times of needs. They have been great guides, both for academic and real-life situations. Their continuous support and guidance combined with their wisdom has allowed me to move forward.

I would like to thank Rasul Tarvirdilu Asl for his help throughout the creation of this thesis, who was always there for discussions.

I would like to thank my family for their constant love and support, my father Kamer, my mother Asuman, my brothers Alper and Can. Also many thanks to my sister in law Sevtap and lovely niece Ece for putting smiles on my face.

Lastly, I wish to thank my friends İrem, Canberk, Burçak, Tugay, Alptuğ, Kerem, Valdrin, Victoria, Batuhan and Tanya for their support and belief in me in this process.

TABLE OF CONTENTS

LIST OF TABLES

TABLES

LIST OF FIGURES

FIGURES

LIST OF SYMBOLS

SYMBOLS

A	Area
B	Flux density
D	Outer diameter
e	Self-emf
ep	Excitation period
F	Force
FL	Flux linkage
f	Frequency
f_p	Penalty factor
g	Airgap length
H	Flux intensity
h_r	Rotor pole height
h_s	Stator pole height
I	Current
J	Current density
K	Back-core width to half stator tooth width ratio
k_f	Slot fill factor
L	Inductance
l	Length
MMF	Magnetomotive force
N	Number of turns
N_r	Number of rotor poles
N_s	Number of stator poles
P	Permeance
q	Number of phases

R	Resistance
T	Torque
t	Time
t_r	Rotor tooth width
t_s	Stator tooth width
V	Voltage
W	Energy
W_{rbc}	Rotor back-core width
W_{sbc}	Stator back-core width
x_n	Normalized position
α	Tapering angle
Δ	Difference operator
η	Efficiency
θ	Electrical angle
λ	Tooth pitch
μ	Permeability
ρ	Resistivity
φ	Flux
ω	Angular speed

CHAPTER 1

INTRODUCTION

1.1. Motivation and purpose of the study

The purpose of this study is to create a fast and accurate program to calculate the performance of switched reluctance motors, offer an optimization method to find the best combination of poles in order to maximize torque of switched reluctance motors and to create an interface that a user can easily interact with for calculating the performance and the optimized performance of a switched reluctance motor (which further will be referred to as SRM or SR motor), giving out results in both numerical and graphical form. Furthermore, the aim includes correcting and verifying the previous research and calculations done in this purpose. Variations of permanent magnet motors are being used widely in the industry. However, these motors need rare earth elements as magnets which are both limited in resource and of high value [1]. Thus, a need for cheaper and more sustainable electric motor arises. The switched reluctance motor is a good alternative to these as it does not contain rare earth elements for permanent magnetization, rather it relies on the change in magnetic field as a result of switching on the stator side, as well as having lumped stator windings and no rotor windings [2]. SR motors have not been mainly preferred in industry due to their lack in power density, lower efficiency and higher torque ripple and vibration [3]. However, its power density and efficiency are higher than most other electrical motor types, also it can be operated to have acceptable level of noise and vibration [4]. The aim of the optimization in this research is to find the optimal pole combination value such that the average torque thus the output power of SRM will be maximized in order to have comparable power density to PM motors, also providing a software that will help designing SR motors for various applications where SRM can be used.

1.2. Brief introduction into SR motors

The switched reluctance motor is a DC supplied singly excited (only on the stator side) doubly salient pole electric motor where the change in inductance is the main key to torque (T) production [5]. They differ from stepper motors in the sense that they are designed for continuous operation while stepper motors are designed for position control [6]. The following information under this title can be found in detail in [5, 6] and important points will be summarized here. Slots on stator side are narrow and have concentrated windings, thus allowing the winding procedure to be easy. The winding wires are thinner compared to AC motors designed to be operating under the same voltage, requiring more turns per phase. The winding structure has no phase crossovers. End windings are also shorted and have small end leakage values together with small end resistances. The gaps in between are large enough to let the air cool the motor without having much windage losses, and motor can also be liquid cooled. The rotor side has no windings or permanent magnets on it, making the production easier and leading to a low inertia, and allowing higher rotor temperature values compared to brushless DC motors. Losses are mainly concentrated on the stator side, and it should be noted that stator part is more eligible to be cooled. Low inertia allows a high torque production at starting, without having to deal with the adverse effects of high in-rush currents. Switched reluctance motors can be operated at wide speed ranges, as there is no fixed magnetic flux created on the rotor side as in BLDC motors, the maximum speed is not limited by the supply voltage. When there is a fault occurring in the motor, safety is assured through short circuit current and open circuit voltage being almost zero. Torque production within the SR motor is independent of the polarity of the current (I), allowing a simpler controller circuitry.

Although having the benefits, some of these come with a drawback as well. There being no excitation on the rotor side puts a heavy burden on the stator for excitation, resulting in high per unit copper losses, which is especially a limitation on smaller sized SR motors for the T/I value and efficiency.

The switched reluctance motor also comes with few disadvantages. Main problem is the non-uniformly produced torque having ripples. However, it is still easier to attain a smooth torque in low speeds, where load is very susceptible to torque ripples. This rippled nature can be accompanied by an acoustic noise, which can be a problem especially in cases where ultrasonic switching frequencies are required.

The switched reluctance motor makes use of internal torque multiplication, achieved through higher switching frequency. This increases the converter switching losses and the core losses, however, this allows a better power factor and higher T/I values. The adverse effects are also compensated by the SR motor having a smaller size compared to a same performance AC motor, and at parts of the core of SR machines the flux is unidirectional that helps decrease the hysteresis losses.

1.3. Literature research on the area

There is a lot of research conducted on the prediction of performance of SR motors. [7, 8] focus on increasing torque density of SR motors, [9-12] focus on design optimizations, [13-15] focus on decreasing the torque ripple, [16] focuses on effects of stator and rotor pole ratio coefficients on the efficiency of switched reluctance motors, and [17] focuses on design and performance calculations.

However, this study concentrates on the methods developed at METU by Ertan and his research students.

The approach used in this study for prediction of SR motor performance is based on a set of normalized permeance and force curves. This approach is very useful since the dimensionless data permits prediction of static torque-position-current and flux linkage-current-position curves of any SR motor. As will be demonstrated in this research, it also leads to accurate predictions of motor performance.

It should be noted that once the static torque-position-current curve of a motor is available as well as its flux linkage-current-position curve, SR motor torque at a desired speed can be calculated as a function of its drive parameters such as turn-on angle, conduction period, etc., which is also the method used in Chapter 2 and Chapter 4 of this research.

The normalized data is first introduced in the research conducted by Ertan [18]. Tohumcu and Ertan [19] developed methods for prediction of torque and flux linkage characteristics of any asymmetrically slotted SR motor geometries. This data is later expanded by Beşenek [20] to be used on SR motors with higher values of tooth pitch over air gap length ratio. Mahariq [21] researches on the accuracy of this data through usage of Finite Element Method. Later, a software based on the mentioned approach is developed by Göynük [22]. However, this software was developed in old Pascal language with many currently unsupported libraries and commands used, also being highly unstable and offering just a few variables to be changed for calculations, whose results are not as accurate as desired. It is important to note that the calculations through the software offered by Göynük are only to predict the static torque and flux linkage curves and does not go into further calculating the performance of SR motors. For these reasons, a study was initiated in 2016 by Tarvirdilu [23] to update the calculations and to calculate the performances of SR motors under running conditions. It is important to note that Tarvirdilu's research is done with the inclusion of the research done by Şahin [14] under the light of [13] by Ertan and Leblebicioğlu, which focus on the air gap geometry to minimize the torque ripple in switched reluctance motors. The research by Tarvirdilu [23] does not introduce a user interface, but rather is done by calculations in MATLAB software. However, his research contains the errors mentioned in the statements given on the following page.

1- Incorrect modelling of an asymmetrical SRM into two symmetrically slotted SRMs, the correct method of which having been described by Tohumcu and Ertan [19] in their research and summarized in Section 1.4.2 of this research. The fault in modelling can be seen in Section 2.2.1.
2- Faulty extrapolations of normalized data leading to errors in static torque-position-current data, as mentioned in Section 2.2.2.1.
3- Faulty extrapolations of normalized data leading to errors in flux linkage-current-position data, as mentioned in Section 2.2.2.2.
4- Errors in core loss calculations due to not considering number of simultaneously excited pole pairs, as mentioned in Section 2.3.4.3.
5- Error in rms current calculations, as can be seen in Section 4.6.3.
6- High errors in optimization performance calculation results, which can be seen in Section 4.7.
7- Many algorithm errors within the implementation of the MATLAB code for both the performance calculation and the optimization process, which are corrected by the author but will not be explicitly shown in this thesis.

These errors and the lack of an interface program are the reasons that lead to the necessity of this research.

1.4. Normalization and performance calculations

This part will focus on the definition and calculation of the normalized data used in this research and will give a brief information on how the static torque-position-current values, flux linkage-current-position values and performances of the SRM under running conditions are calculated.

1.4.1. The normalized data

This section will give a summary of the methods for the calculations of the normalized data used in this research. The parameters used for the calculations are defined in Table 1.1 and are varied in the same range as [23].

Table 1.1. *Variable parameters of the basic geometry for normalization*

Variable	Explanation	Variation range	Number of points
λ/g	Tooth pitch to air gap length ratio	40 to 250 with a step of 15	11
t/λ	Tooth width to tooth pitch ratio	0.3 to 0.5 with a step of 0.1	3
MMF	Excitation magnetomotive force	50 to 3000 A.turns with steps of 50 A.turns	60
$x_n=2x/\lambda$	Normalized position (Figure 1.1 shows the distance x)	0 to 1 with a step of 0.05	21

The core used for calculating the normalized data is named C-core and assumed to be infinitely permeable for eliminating MMF drops on the core, and the area around is assumed to be vacuum not to allow flux leakage due to tooth saturation. Data are calculated for a tooth pitch (λ) value of 0.0172m, core length (L_c) value of 1m and a slot depth (h_s) that is 40 times the air gap length (g). The B-H curve data of the core is the same as the data supplied in [14], and is given in Figure A.1 within Appendices Section A. It is important to note that the B-H curve and core loss data of the machines used in this research are given in Appendices Section A. A model of the geometry used in [18] can be seen in the following Figure 1.1.

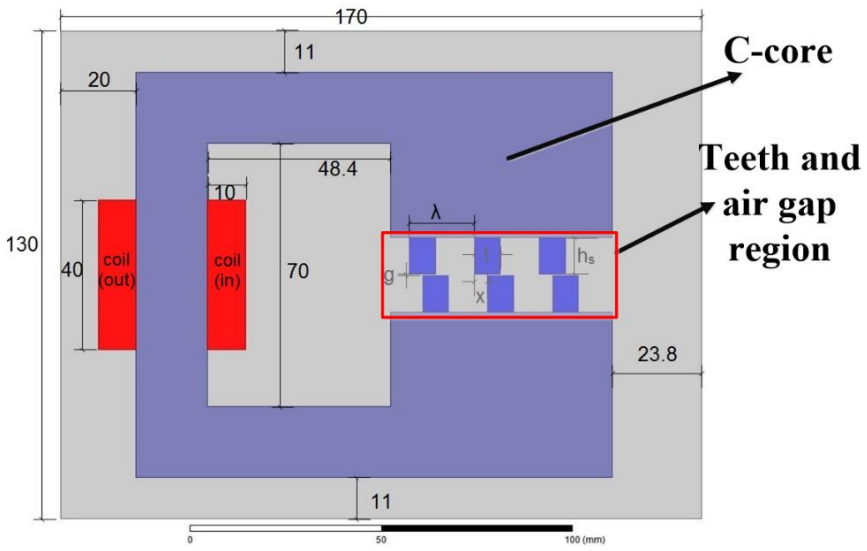

Figure 1.1. Model geometry where $x_n=0.4$, $t/\lambda=0.4$ and $\lambda/g=70$

The normalized permeance, force and average tooth flux density is calculated for the given λ/g, t/λ and x_n under different MMF values.

It is important to define how these parameters are calculated. The average flux density value (B_{av}) can be found as given in Equation 1.1, where B_{total} is the total flux passing one tooth pitch divided by the tooth pitch area. It is to be noted that these calculations are done at the middle tooth, and λ is the tooth pitch centered at the middle tooth of Figure 1.1.

$$B_{av} = \frac{1}{t}\int_0^{\lambda} B_{total}.dl \tag{1.1}$$

For the calculation of normalized permeance (P_n), a base permeance (P_{base}) is necessary. The base used is selected as given in Equation 1.2, which corresponds to the permeance of air gap region. In this formula, λL_c corresponds to the area of the air gap region and μ_0 is the permeability of free space.

$$P_{base} = \frac{\mu_0 \lambda L_c}{g} \tag{1.2}$$

The normalization is done as given in Equation 1.4 where P_x is the permeance calculated for the middle tooth in Equation 1.3.

$$P_x = \frac{\varphi}{N \times I} \tag{1.3}$$

$$P_n = \frac{P_x}{P_{base}} \tag{1.4}$$

It should be noted that φ in Equation 1.3 is the flux passing the middle tooth region. With these at hand, the normalized permeance is driven as in Equation 1.5.

$$P_n = \frac{\varphi}{\mu_0 (N \times I)(\frac{\lambda}{g})L_c} \tag{1.5}$$

One important issue to note is that in Equation 1.5, L_c has a value of 1 meter.

The normal and tangential forces are calculated using the Maxwell software [23], in which the partial derivative of the stored energy (W_e) with respect to displacement is used to calculate the force.

$$F_t = -\frac{\partial W_e}{\partial x} \tag{1.6}$$

The calculation of the force data can also be done by Maxwell stress tensor method [24] as given in Equation 1.7 for the tangential force (F_t) and Equation 1.8 for the normal force (F_n) where B_n and B_t stand for the normal and tangential flux densities, respectively.

$$F_t = \frac{1}{2\mu_0}\iint B_n B_t dA \tag{1.7}$$

$$F_n = \frac{1}{2\mu_0}\iint (B_n^2 - B_t^2) dA \tag{1.8}$$

1.4.2. Normalization method for SRMs with asymmetrically slotted poles

It is important to note that the calculations offered in Section 1.4.1 have been made using symmetrically slotted pole assumptions. However, switched reluctance motors in general have uneven structured stator and rotor poles. Thus, a method has been driven in [19] for the calculation of normalized permeance, force and MMF values of the asymmetrically slotted SRMs. This method suggests the stator and rotor poles of the switched reluctance motor to be modelled into two symmetrically slotted forms, which will be referred to as Geometry-A and Geometry-B. The stator and rotor poles of the Geometry-A are modelled to have the same width as the stator pole width of the asymmetrically slotted motor. In Geometry-B, the stator and rotor tooth widths are modelled to have the same width as the rotor pole width of the asymmetrically slotted motor. Figure 1.2 shows the mentioned modeling of the poles.

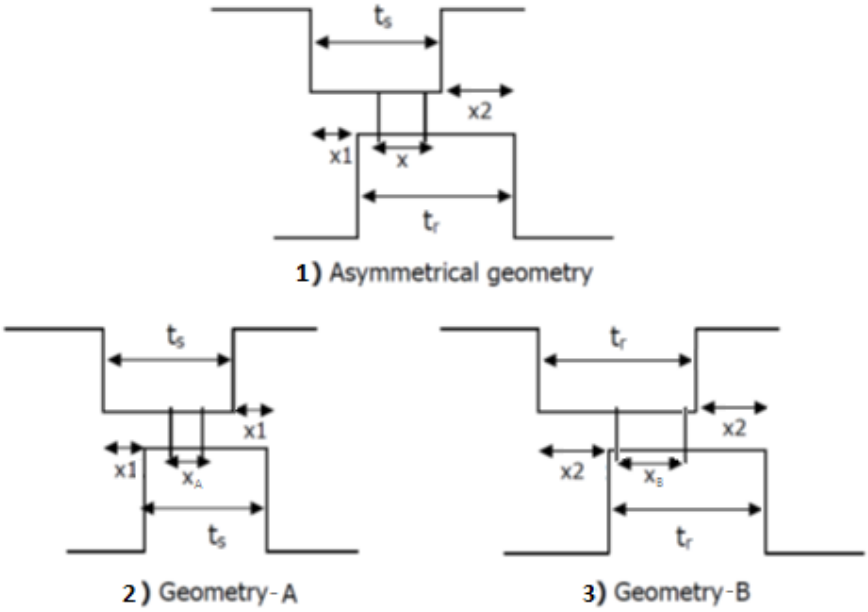

Figure 1.2. Symmetrically slotted modeling of the asymmetrical stator and rotor poles

In Figure 1.2, x, x_A and x_B are the distances between the middle points of the poles. Tooth pitches of the geometries are calculated as given in Equation 1.9 and Equation 1.10. It is important to note that the λ/g and t/λ values will be assigned a different value if the distance to the next pair of teeth is lower than 25g as suggested in [25], due to the nearing teeth starting to affect each other.

$$\lambda_A = max(\lambda_r, t_s + x_1 + 25\,g) \tag{1.9}$$

$$\lambda_B = max(\lambda_r, t_r + x_2 + 25\,g) \tag{1.10}$$

λ_A and λ_B are the tooth pitches of the symmetrically slotted geometries. λ_s and λ_r refer to the tooth pitches of the stator and rotor, respectively, g is the length of the air gap, t_s is the tooth width of stator, t_r is the tooth width of rotor, x_1 and x_2 are the distances defined in Figure 1.2.

It needs to be stated that when the poles are further away from each other, the (t_s+x_1+25g) and (t_r+x_2+25g) values will be higher than the original tooth pitch of the rotor, thus they will represent the tooth pitch values for the symmetrically slotted geometries A and B, respectively. When the poles start to near the aligned position, x_1 and x_2 have smaller values, thus λ_r value replaces them as the tooth pitch values for the symmetrically slotted geometries.

For calculating the original tooth pitches, rotor outer diameter value, air gap length and number of stator and rotor poles of the motor are used. These calculations are given in Equation 1.11 and Equation 1.12.

$$\lambda_s = \frac{\pi(D_{or} + 2g)}{N_s} \tag{1.11}$$

$$\lambda_r = \frac{\pi D_{or}}{N_r} \tag{1.12}$$

In the given calculations N_s is the number of stator poles, N_r is the number of rotor poles and D_{or} is the outer diameter of the rotor.

The correct determination of the tooth pitch data is very important, as it is used in calculations of the normalized permeance, tangential force and the MMF values, and consequently the torque-position-current and flux linkage-current-position values. The normalized permeance, tangential force and the tooth region MMF values for the asymmetrically slotted geometry can be simply calculated from the two symmetrically slotted geometries as in [19,23].

$$P_n = \frac{2P_{n_A}P_{n_B}}{P_{n_A} + P_{n_B}} \tag{1.13}$$

$$MMF = \frac{MMF_A + MMF_B}{2} \tag{1.14}$$

$$F = \frac{F_A + F_B}{2} \tag{1.15}$$

1.4.3. Determination of the operating point

Once the normalized data is determined, the operating point needs to be found. For this purpose, total MMF drop (MMF_{total}) is calculated by adding the teeth region MMF drop (MMF_{teeth}) and back iron MMF drop (MMF_{bi}).

$$MMF_{total} = MMF_{teeth} + MMF_{bi} \tag{1.16}$$

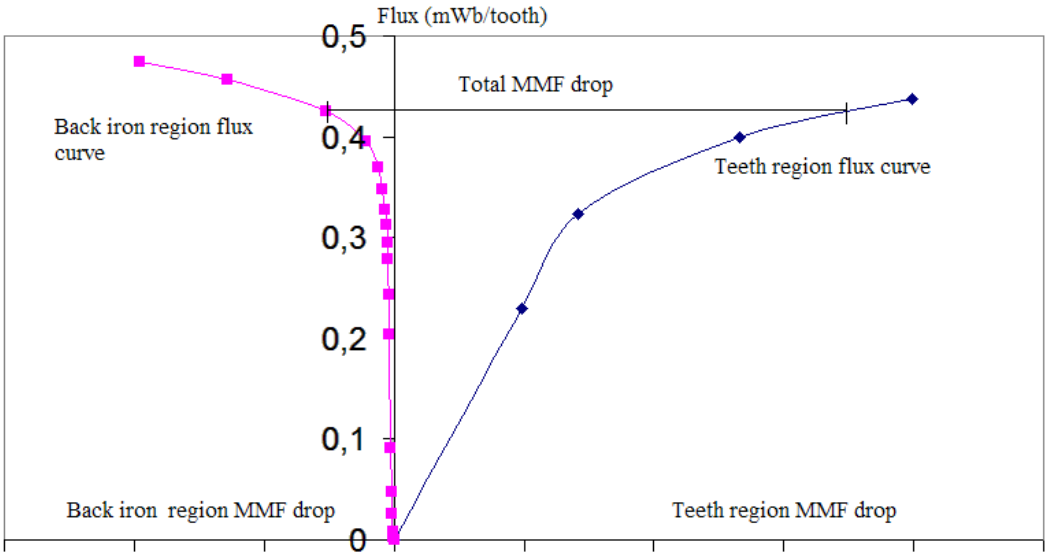

Figure 1.3. Total MMF drop of the SRM through the MMF drops in teeth region and back iron region

Calculation for the back-iron losses are given in detail in [23]. The following is a summary of these calculations.

For back-iron losses, there are four regions that need to be considered. Stator back-tooth, rotor back-tooth, stator back core and rotor back core. The stator tooth MMF drop is considered for the length that corresponds to 40 times the air gap length, starting from the tip of the tooth, and the region after that is taken to belong to the stator back-tooth. Figure 1.4 shows the described regions in the following page.

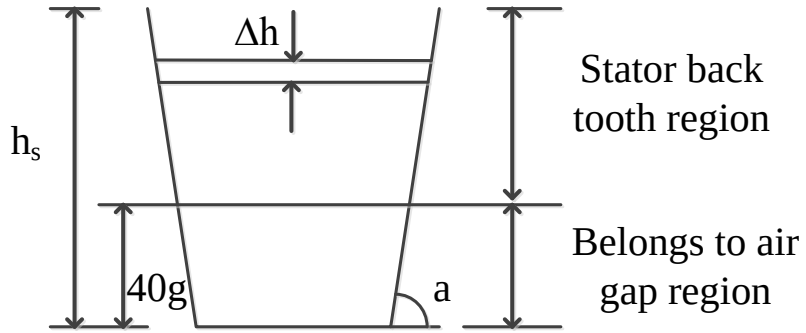

Figure 1.4. The stator back-tooth region

It should be noted that the distance Δh in Figure 1.4 is defined as given in Equation 1.17, h_s is the height of the stator pole and tapering angle is shown with 'a'.

$$\Delta h = \frac{h_s - 40g}{10} \tag{1.17}$$

With the back-tooth region described, the MMF drop on the stator back-tooth region (MMF_{sbt}) is calculated as follows.

$$MMF_{sbt} = \sum_{i=1}^{10} H_i \Delta h_i = \Delta h \sum_{i=1}^{10} H_i \tag{1.18}$$

H_i in Equation 1.18 is the flux intensity of the sections of stator back-tooth. In order to calculate H_i, firstly flux density for each section (B_i) is calculated.

$$B_i = \frac{\varphi}{Lt_i} \tag{1.19}$$

Once the flux density value is found, flux intensities are obtained from B-H characteristics of the core material.

The MMF drop in the rotor back-tooth (MMF_{rbt}) is calculated in a similar manner. It should be noted that, as there is no tapering on the rotor poles, the calculations are simply done as shown in Equation 1.20.

$$MMF_{rbt} = H_{rbt}(h_r - 40g) \tag{1.20}$$

The rotor back tooth flux intensity (H_{rbt}) given in Equation 1.20 is driven from the B-H curve of the core material once the rotor back tooth flux density (B_{rbt}) is found.

$$B_{rbt} = \frac{\varphi}{Lt_r} \tag{1.21}$$

For the stator back core MMF drop (MMF_{sbc}), firstly the flux density of the stator back-core region (B_{sbc}) needs to be determined.

$$B_{sbc} = \frac{\varphi}{2LW_{sbc}} \tag{1.22}$$

In Equation 1.22, W_{sbc} stands for the width of the stator back core and L is the core length. The flux density value is again used to find the flux intensity of the stator back-core region (H_{sbc}) using the B-H curve. Afterwards, MMF drop of the stator back-core region (MMF_{sbc}) is calculated as given in Equation 1.23.

$$MMF_{sbc} = H_{sbc}l_{sbc} = H_{sbc}\left(\frac{2q}{N_s} \times \frac{\pi(D_{os} - W_{sbc})}{2}\right) \tag{1.23}$$

In Equation 1.23, N_s is the number of stator poles, D_{os} is the outer diameter of the stator, q is the number of phases and l_{sbc} is the length of the flux path within the stator back-core region.

The MMF drop in the rotor back-core region (MMF_{rbc}) is found similarly, as given in Equation 1.24, where D_{or} is the rotor outer diameter, H_{rbc} is the flux intensity of the rotor back-core region, W_{rbc} is the width of the rotor back-core region, h_r is the rotor pole height and l_{rbc} is the length of the flux path within the rotor back-core region.

$$MMF_{rbc} = H_{rbc} l_{rbc} = H_{rbc} \left(\frac{2q}{N_s} \times \frac{\pi(D_{or} - 2h_r - W_{rbc})}{2} \right) \quad (1.24)$$

Once the stator back-tooth, stator back-core, rotor back-tooth and the rotor back-core MMF drops are determined, the total of the back iron MMF drop is calculated as follows.

$$MMF_{bi} = 2(MMF_{sbt} + MMF_{rbt}) + MMF_{sbc} + MMF_{rbc} \quad (1.25)$$

It should be noted that the back-iron MMF drop is calculated for the stator tooth flux densities from 0.01T up to 2.2T by steps of 0.01T. This covers all the possible operating regions as the maximum allowable flux density is 2T in the stator tooth [23].

1.4.4. The slot leakage flux linkage

The flux leaking to adjacent poles are also taken into consideration as in [23]. This will be referred to as slot leakage flux, and its effects are discussed in Chapter 2 of this research. This flux can be observed in Figure 1.5.

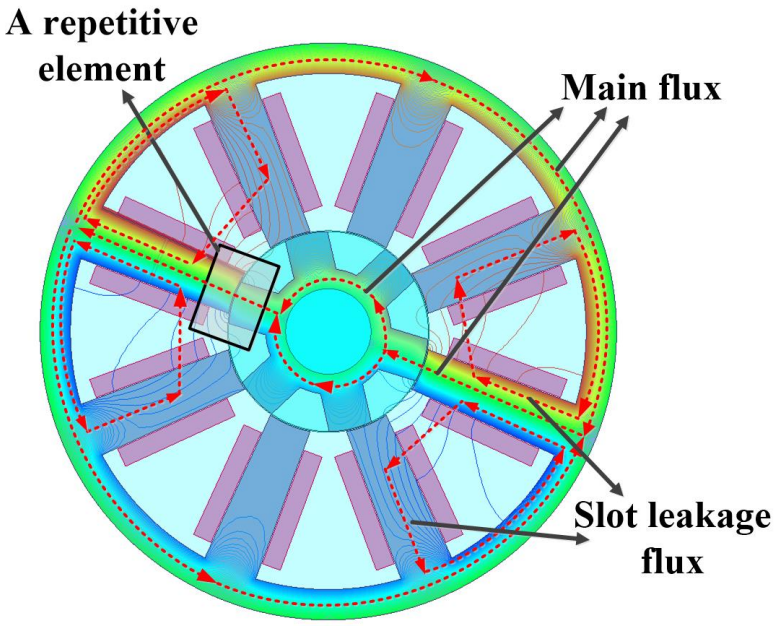

Figure 1.5. The slot leakage flux

The calculation of the slot leakage flux is explained in detail in [23], thus will not be re-calculated in this research. Once the slot leakage flux ($\varphi_{leakage}$) is calculated, slot leakage flux linkage ($FL_{leakage}$) is found as in Equation 1.26.

$$FL_{leakage} = 2 \times 2 \times N\varphi_{leakage} \tag{1.26}$$

The first multiplication by 2 is due to the 2 adjacent teeth, and the second multiplication by 2 is for calculating the leakage flux linkage value of the pole pair.

1.4.5. Static torque and flux linkage calculations

Once the total MMF drop of the SRM is calculated, the current can be found by Equation 1.27, where N is the number of turns per pole.

$$I = \frac{MMF_{total}}{2N} \tag{1.27}$$

Through this current and the dataset created from the normalized variables, tangential force for specific λ/g and t/λ values are determined. Torque is simply calculated from the tangential force data as given in Equation 1.28.

$$T = \frac{F_t D_{or} L}{2} \tag{1.28}$$

As the stator pole flux is also known, the flux linkage can be calculated as given in Equation 1.29.

$$FL = 2N\varphi \tag{1.29}$$

Slot leakage flux linkage found in Equation 1.26 is also added into flux linkage found in Equation 1.29 for calculation of flux linkage values that include slot leakage.

Finally, the static torque-position-current and flux linkage-position-current graphs are constructed through combination of these calculations done at different normalized positions and flux densities.

Figure 1.6 and Figure 1.7 show the typical static torque-position-current values and typical flux linkage-current-position values for an SRM calculated with the proposed methods [23].

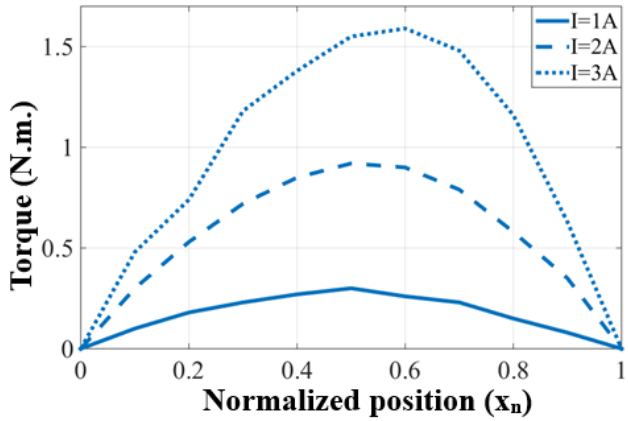

Figure 1.6. Typical torque-position-current values of a switched reluctance motor

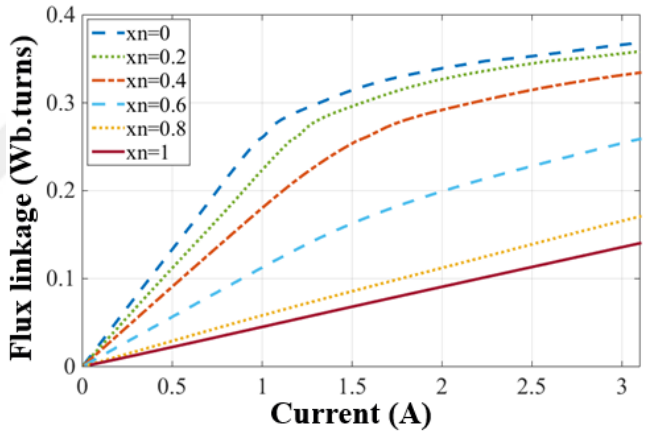

Figure 1.7. Typical flux linkage-current-position values of a switched reluctance motor

1.4.6. Determination of the performances of the SRM under running conditions

After the determination of torque-position-current and flux linkage-current-position values, the instantaneous torque and current of the SRM are to be calculated. These calculations are made under the assumption of a steady state where the SRM is running at a certain speed. Figure 1.8 shows one phase equivalent circuit of a switched reluctance motor.

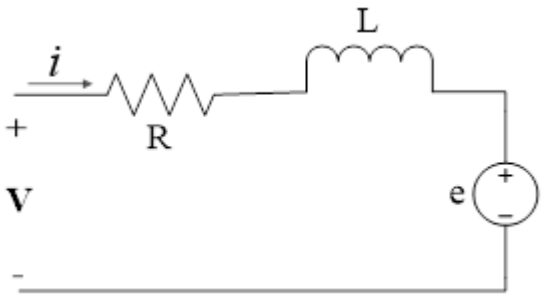

Figure 1.8. Equivalent circuit of an SRM for one phase

In Figure 1.8, V stands for the DC side voltage, '*i*' is the instantaneous current, R is the phase resistance, L is the incremental inductance and e is the back-emf. However, the back emf in this case is different in the sense that it depends on the phase current, also changes with the rotor position. Thus, it will be referred to as self-emf, which is proportional to the current *i*, angular speed ω and rate of change of inductance with rotor angle (θ) [5].

In calculations, initial current and flux linkage (FL) are assumed to have zero value. Initial rotor position is set to the desired turn on angle. Using the proposed model, voltage is calculated in Equation 1.30, which can be rewritten as Equation 1.31.

$$V = Ri(FL,\theta) + \frac{dFL(\theta,i)}{dt} \tag{1.30}$$

$$V = Ri + \frac{dFL(\theta,i)}{d\theta}\frac{d\theta}{dt} = Ri + \omega\frac{dFL(\theta,i)}{d\theta} \tag{1.31}$$

In order to solve Equation 1.31, the equation is written as the differential equation given in Equation 1.32.

$$\frac{dFL(\theta,i)}{d\theta} = \frac{1}{\omega}(V - Ri(FL,\theta)) \tag{1.32}$$

The differential equation given in Equation 1.32 is solved with a fourth order Runge Kutta method, which is explained in detail in [23].

In each iteration of the calculation, the angular position is converted into normalized position, and the flux linkage value calculated by Runge Kutta method is stored to be used in the next iteration. These normalized position and flux linkage values are used to determine the instantaneous torque and current values.

It should be noted that when the current is rising, the source voltage applied is V. When current reaches the maximum chopping value, this voltage is disconnected from the phase, meaning applied voltage is set to zero and current decreases on the freewheeling circuit until the minimum value of the chopping current is reached, after which V is again applied to the phase. When the phase is being turned off, applied voltage is taken as -V in order to fasten the fall of current, which is done in order to avoid a negative torque production.

1.4.7. Calculation of losses and efficiency

Once the phase current is known, copper loss calculation is simple. Equation 1.33 shows the copper loss for one phase of the SRM (P_{cu_1}).

$$P_{cu_1} = 2\frac{q}{N_s}\,(I_{rms})^2 R \tag{1.33}$$

In Equation 1.33, q is the number of phases, N_s is the number of stator poles, I_{rms} is the rms current of one phase and R is the series resistance of one pole pair. For calculating total value of the copper loss (P_{cu}), the per phase copper loss needs to be multiplied by the number of phases.

$$P_{cu} = qP_{cu_1} \tag{1.34}$$

For the calculation of core losses, Steinmetz's equation is used, basic form of which is given in Equation 1.35.

$$P_v = kf^a B^b \tag{1.35}$$

In the basic Steinmetz's equation, P_v is the time average of the power loss in mW per cubic centimeter, f is the frequency in kHz and B is the peak value of the magnetic flux density. The parameters k, a and b are the Steinmetz's coefficients and are found from the iron loss (W/kg) vs flux density data of the material at different frequency values. Example calculations are given below for the core materials (10JNEX900 and M36) of the two SRMs used in this research, which are defined in Section 2.3.1.

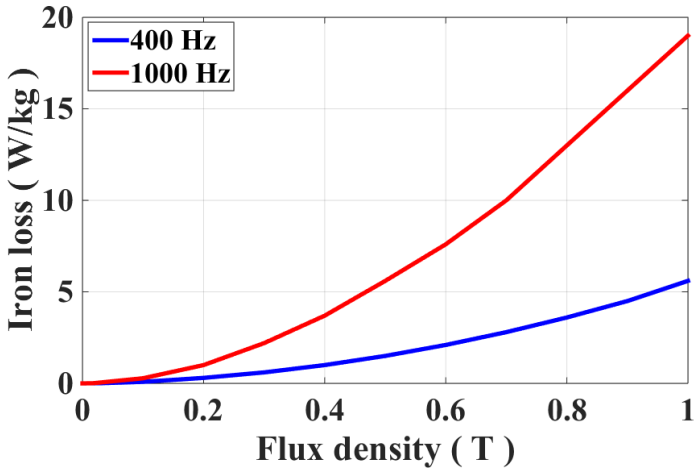

Figure 1.9. Iron loss vs flux density data of 10JNEX900 for 400Hz and 1kHz

The loss coefficients are calculated using the data provided in Figure 1.9. Iron loss values for both the frequencies at 0.4T are used to derive these coefficients and are substituted into Equation 1.36 [23].

$$P_c = k_e f^2 B^2 + k_h f B^n \tag{1.36}$$

In Equation 1.36, P_c stands for the core loss, f is the frequency, B is the peak value of the magnetic flux density, 'n' is the power coefficient, k_e is the eddy current coefficient and k_h is the hysteresis coefficient. It needs to be noted that power coefficient 'n' is taken to be equal to 2, as in [23]. Once the substitution is done, k_e is computed as 1.25×10^{-5} and k_h as 0.01063.

The core losses for M36 are calculated in a similar manner. The coefficients for this material are predicted by the research of Pillay [26-28]. Figure 1.10 shows the eddy current coefficient versus frequency.

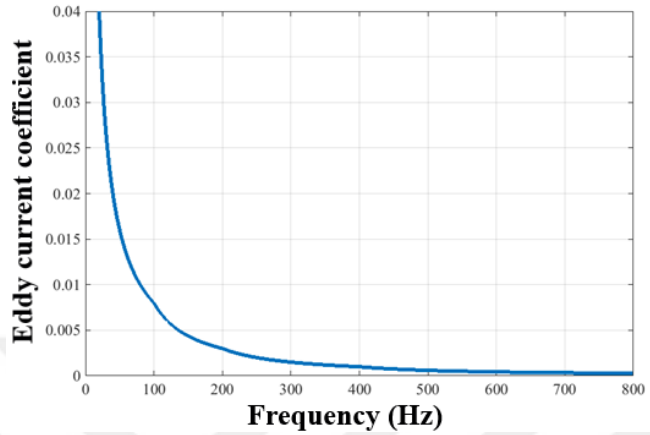

Figure 1.10. Eddy current coefficient of M36 vs frequency

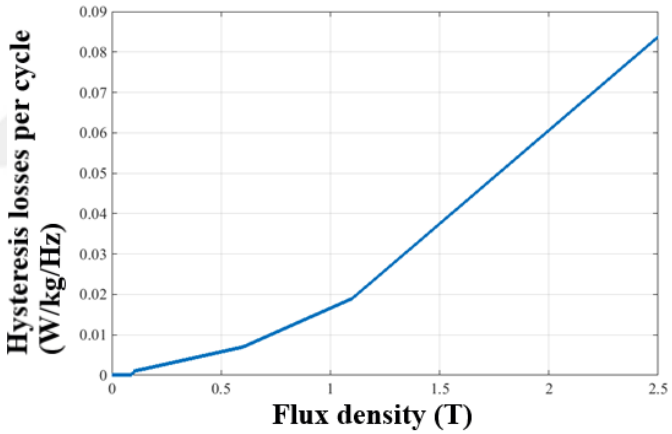

Figure 1.11. Hysteresis loss per cycle for M36 given in W/kg/Hz

Hysteresis losses are given in W/kg/Hz, so hysteresis losses per unit motor mass (W/kg) can be found by multiplying with the frequency. The calculations can be found in detail in [23].

Once the coefficients are found, losses at stator teeth, rotor teeth, stator back-core and rotor back-core are calculated by multiplication with their masses. Addition of these values gives the total value of the core losses.

After the determination of copper (P_{cu}) and core (P_c) losses, total loss (P_{loss}) is found by addition of the losses.

$$P_{loss} = P_{cu} + P_c \tag{1.37}$$

For efficiency calculations, determination of output power (P_{out}) and input power (P_{in}) is necessary. Output power is found by the multiplication of average torque (T_{avg}) and mechanical speed (ω_{mech}), as given in Equation 1.38, and input power is found from the summation of total loss with output power. Afterwards, efficiency (η) can be simply defined as in Equation 1.39.

$$P_{out} = T_{avg} \times \omega_{mech} \tag{1.38}$$

$$\eta = \frac{P_{out}}{P_{in}} = \frac{P_{out}}{P_{out} + P_{loss}} \tag{1.39}$$

1.5. Structure of this research

This thesis firstly focuses on correcting the previous errors for the performance calculation and optimization of the SR motors as mentioned in Section 1.3.

The second aim is the creation of a detailed user interface for performance calculation and optimization simulations.

The final aim is to find out how pole combinations (different selections of N_s and N_r) affects the average torque, torque per unit volume and efficiency of a given SR motor.

For the achievement of these aims, the study is constructed as follows.

In Chapter 2, the performance calculation errors encountered in [23] are corrected. Performances of two switched reluctance motors are calculated and compared with the results given in [23]. Also, polynomial fitting is used instead of neural network approach for data extrapolation, thus saving a vast amount of computational time.

Chapter 3 explains the user interface created for the performance and optimization simulations. It must be noted that this program is tailored in detail for stability, debugged for any user-based errors, and does not use any licensed packages in the base code or libraries. This means any interface, including plotting is made from scratch. The software is developed for using as little resources, both execution time and memory space, as possible. Object oriented C# language is chosen for coding and C# methods and classes are utilized for minimization of the ripple effect [29]. The source code includes comments on the used algorithms and their purposes, thus further developments can be made by other researchers if necessary. The program is a result of 2 years of research and development and consists of over 30 thousand line of codes.

Chapter 4 focuses on the optimization of the switched reluctance motor. The design procedure and the optimization method are explained in detail. Results of the optimization performance calculations are compared to the previous research [23]. The optimal pole combination of the given SRM is calculated and explained.

It needs to be noted that implementations of both the performance and optimization calculations done by Tarvirdilu [23] within the MATLAB software, which consist of over 5 thousand lines of codes, have been analyzed, controlled for errors, corrected and altered for this research. The details for each alteration will not be given in this research, but the main changes in computations and the effects of the faults on previously calculated results will be given in Chapter 2 and Chapter 4 of this research.

CHAPTER 2

PERFORMANCE ANALYSIS CORRECTIONS FOR THE SRM AND VERIFICATION OF RESULTS

2.1. The aim of the chapter

This chapter focuses on correcting the errors encountered in [23] for switched reluctance motor performance calculation purposes and comparing the corrected performance results obtained for two switched reluctance motors that have been used in [23].

For these purposes, firstly the calculation errors will be corrected, and methods used for this purpose will be explained. Afterwards, the two test SRMs will be explained and their performances will be obtained. Finally, the results will be compared to those previously achieved in [23].

2.2. Correction of performance calculation errors

The switched reluctance motor performances are calculated as briefly explained in Section 1.4 of this research. In this section, the corrections on the previous research [23] is explained.

2.2.1. Errors in the modelling of asymmetrically slotted SRMs

As explained in Section 1.4.2 of this research, the switched reluctance motors in general have uneven structured geometries for the stator and rotor poles. In order to be able to use the normalization methods proposed in Section 1.4.1, the normalized permeance, force and MMF data for the unevenly structured SRM needs to be determined, the method for which is developed by [19]. For calculation of these data, [19] offers the tooth pitches of the asymmetrically slotted SRMs to be modeled as two symmetrically slotted SRMs.

For the calculation of the normalized tooth pitches of the symmetrically slotted geometries given in Figure 1.2, Tarvirdilu has used the following Equation 2.1 and Equation 2.2 in [23].

$$\lambda_A = max(\lambda_s, t_s + x_1 + 25\,g) \tag{2.1}$$

$$\lambda_B = max(\lambda_r, t_r + x_2 + 25\,g) \tag{2.2}$$

However, the calculation of the tooth pitch of structure A is flawed. The Equation 2.1 in the correct form needs to be as given the Equation 1.9.

2.2.2. Error corrections on data extrapolations

Normalized data is calculated for the values given in Table 1.1 with the methods explained in Section 1.4. These data, however, give normalized permeance, MMF and force data for only certain points that are given in the Table 1.1. For the normalized data to cover a variety of range for calculations of different switched reluctance motors, data extrapolation needs to be done on the obtained results.

In order to find intermittent values for the normalized permeance, MMF and force data, in [23] Tarvirdilu uses feed forward neural networks. Usage of neural networks for extrapolation purposes is a very accurate procedure, if the neural network is trained correctly. However, the feed forward nature of the neural networks used in [23] leads to faulty training of neural networks. As the static torque and flux linkage characteristics are driven from these data, faulty training of the neural networks lead to fault calculations of static torque and flux linkage values. It also needs to be mentioned that training the neural networks is a highly time consuming process. In order to overcome the errors introduced by faulty extrapolations done in [23], the author of this research has used polynomial fitting method, which decreases the computation time of performance calculations from hours to minutes.

2.2.2.1. Errors in the static torque-position-current calculations

It can be clearly seen in Figure 2.1 that extrapolated data derived through neural networks used in [23] lead to faulty calculations of static torque-position-current values. The torque data of the torque-position-current graph reaches zero values before the out position. It should also be noted that these zero values are reached at different normalized position values for each current value.

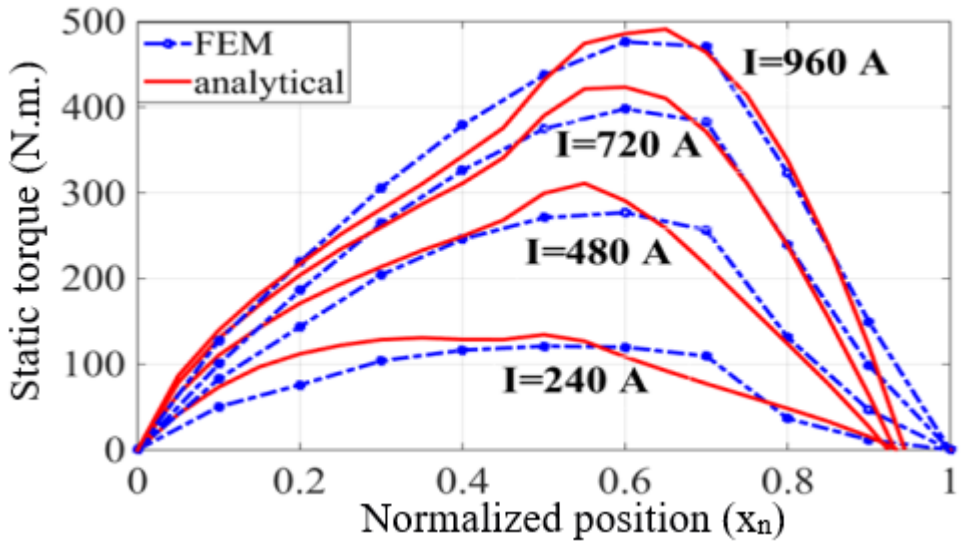

Figure 2.1. Static torque-position-current values retrieved from performance calculation results within [23]

In order to fix this problem, data extrapolations for the normalized permeance, MMF and force data are done by the polynomial fitting method instead of the usage of neural networks. For the implementation, polynomial fitting function of MATLAB software has been used. Static torque values are then found using the methods explained in Section 1.4.5. Inspection of the results show that the attained values through usage of polynomial fitting are closer to the measured values, which will be further discussed in this chapter. The polynomial fitting method also has small errors in the extrapolations in the low current values (lower than 1/3rd of the rated current of the motor), which needs to be corrected, and gives very accurate results around the rated current value. These small mistakes are also corrected in this research.

The fix for the slight inaccuracies introduced by polynomial fitting has been explained in the following steps.

1- The torque values for in and out positions have been set to zero. It needs to be mentioned that for currents around the rated value, there is no error. In very low currents, the torque values at in and out positions can be slightly above or below due to the nature of the fitting, thus is manually set.

2- The values are controlled starting from the torque-position-current graph's rated current value to lower current values, for each normalized position x_n value. If there are n different current values up until the rated current (assuming the n^{th} value being the rated current), the n-2^{nd} line data is proportioned with the n^{th} and n-1^{st} data. Then, the comparison is done similarly for n-3^{rd} data for n-2^{nd} and n-1^{st}. All proportions are saved into a new variable, which will be used if any fault is encountered. The x_n value is increased for the next check.

3- The program starts checking for where a cross over or higher/lower proportion than expected occurs. In this case, the found rate of change in proportions is used to find the expected proportion, and this proportion is multiplied by the previous correct data to find the expected torque value at the specific current and position value.

4- For safe checking, the data until peak value is compared for being of rising trend and the fall section data being of falling trend. In any false occurrences, the data is proportioned using the same method described above. However, the error flag used in the calculations has not encountered such an error.

After the implementation of the steps explained, an exemplary graph of the static torque-position-current data obtained can be seen in Figure 2.2.

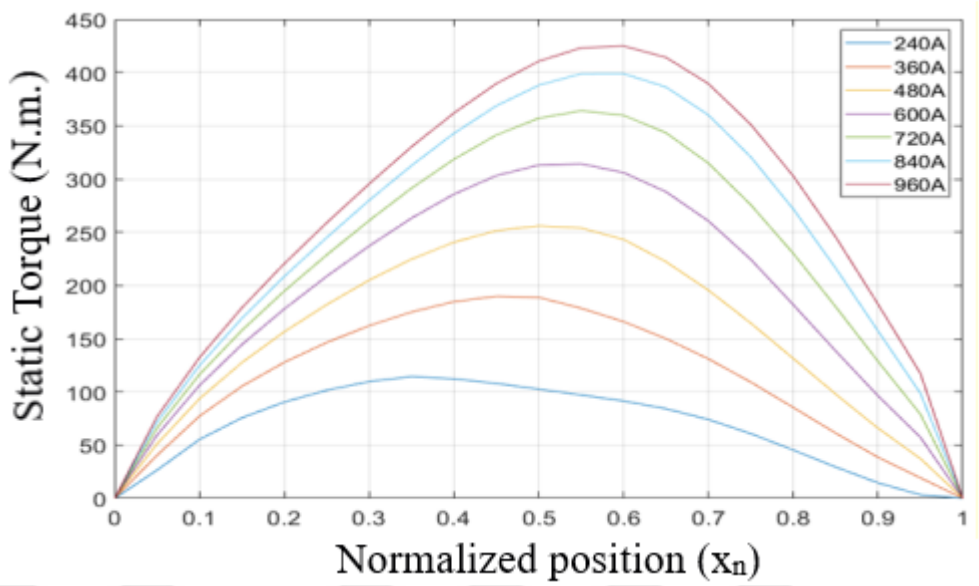

Figure 2.2. Example of static torque-position-current data obtained through polynomial fitting and the described fixes

It can be seen that the static torque calculations found in Section 2.3.3.1 are closer to the measurement values and are in considerably better agreement with the real SRM characteristics than the ones provided in [23].

2.2.2.2. Errors in the flux linkage-current-position calculations

The flux linkage-current-position values of a switched reluctance motor is especially important as it determines the operation loop of the motor. For the correct prediction of the operation, it is crucial for these data to be accurate.

It has previously been stated under Section 2.2 that the tooth pitch calculation and the neural network training done by Tarvirdilu [23] contain errors. The following figures show the faulty results obtained for the flux linkage values after errors in the normalized permeance, MMF and force extrapolations. An example duplicated for this research is given in Figure 2.3 and the results provided in [23] are given in Figure 2.4.

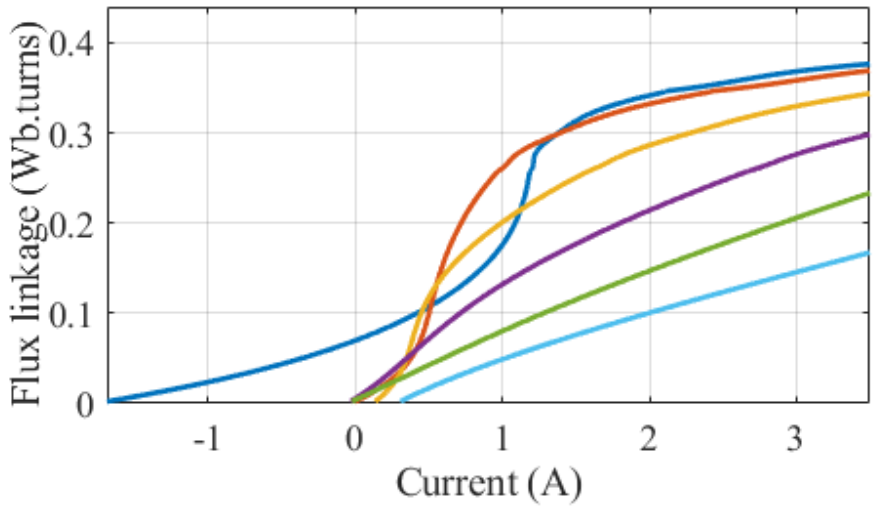

Figure 2.3. Flux linkage-current-position values calculated by neural network method as in [23]

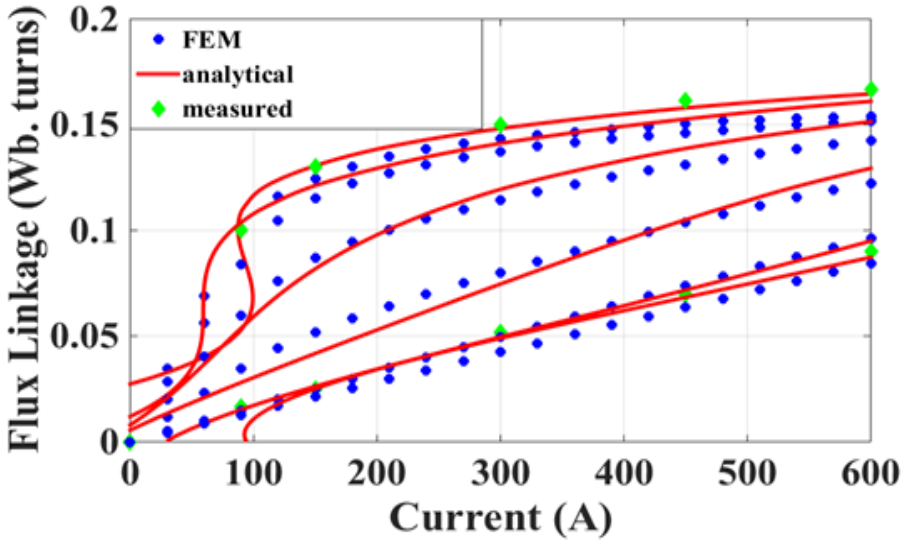

Figure 2.4. Flux linkage-current-position values given in [23]

Both analytical models show impossible material flux linkage vs current properties and need to be corrected for the performance calculations of switched reluctance motors. It can clearly be observed at Figure 2.4 that there are even more than one flux linkage values for the same value of excitation current. Also, flux linkages start from a variety of different points whereas all should have a zero value when the current is zero.

This research, as mentioned, uses polynomial fitting instead of neural networks for data extrapolations in calculation of intermittent values of normalized permeance, MMF and force. The flux linkage-current-position data are then obtained using the methods explained in Section 1.4.5. However as in the case of torque-position-current calculations, in the low current values (less than 1/3rd of rated current), the polynomial fitting introduces small fluctuations that needs to be corrected for achieving the real SRM characteristics. For the corrections, the following steps have been taken.

1- The starting current values are set to zero. It needs to be mentioned that for currents around the rated value, there is no error in the flux linkage values. In very low currents, the flux linkage values are slightly above or below zero due to the nature of the fitting, thus are manually set.

2- Comparison with the measured data shows that after saturation the flux linkage values are in good agreement with the measurements. So, this data is used as a reference to determine the actual flux linkages in the unsaturated region.

3- It is known that until saturation occurs, the inductance which corresponds to the slope of the flux linkage-current graph is constant, thus giving a linear line.

4- Considering that the flux linkage vs current data after saturation are predicted accurately, the data is determined backwards for each flux linkage-phase current-position graph. Starting from the saturation point, there is a small decreasing slope introduced for the cross-over region, i.e. where the saturation starts to occur, approximating the initial decrease with a first order line. This slope passes from the mean of the crossover region data calculated by polynomial fitting, thus to ignore the fluctuations. The current bandwidth of this region is lowest for in position and increases as it goes to the out position, as the transition takes longer due to the slower increase in inductance. The lengths of these regions are taken as the length of the transition region of the polynomial fitting.

5- The inductance is known to be linear until saturation starts to occur. Thus, from the end of the transition region, the data is linearly decreased (backwards) until it reaches zero flux linkage value at zero current value.

6- For very high current values (more than 10 times the rated current value), which is practically very unlikely but theoretically calculated in [23], a comparison algorithm is applied as the very high values also are not as accurate. These values are not practically used, but the calculations are fixed for the sake of achieving total correction. After saturation, at a certain normalized position, the rise rates of flux linkage values should always be lower or equal to the rise rate of the previous values, so the dataset is compared and proportioned when a fault occurs.

It will be seen in Section 2.3.4.2, that the predictions once these steps are done are in good agreement with the measured data and are in considerably better agreement with the real SRM flux linkage characteristics than the ones provided in [23]. An exemplary graph of the obtained flux linkage-current-position data can be seen below.

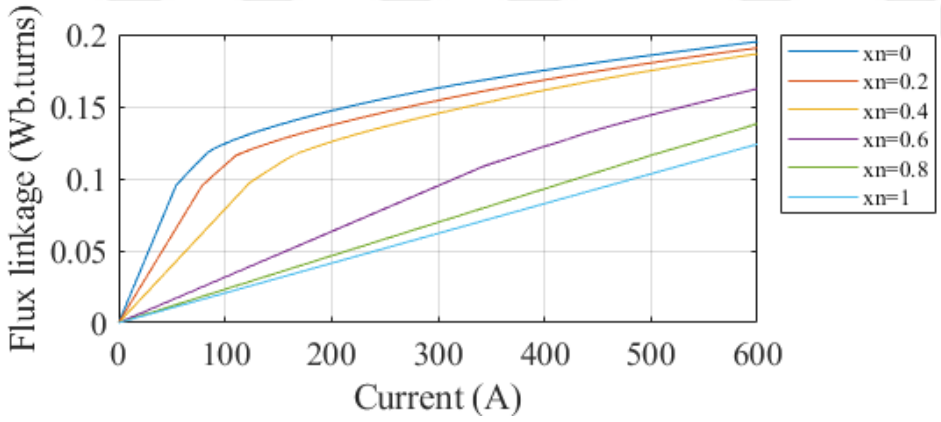

Figure 2.5. Example of flux linkage-current-position data obtained through proposed methods

The following is an example on how these corrections are made. The flux density (B) vs MMF data driven by the methods explained in Section 1.4 from Ertan's model (Figure 1.1) at excitation levels given in [21] is taken to illustrate, as they hold the base for calculations of flux-linkage-current-position data. In this example, λ/g is taken 40 and t/λ is 0.3. Datapoints are for $x_n=0$ which corresponds to the in position.

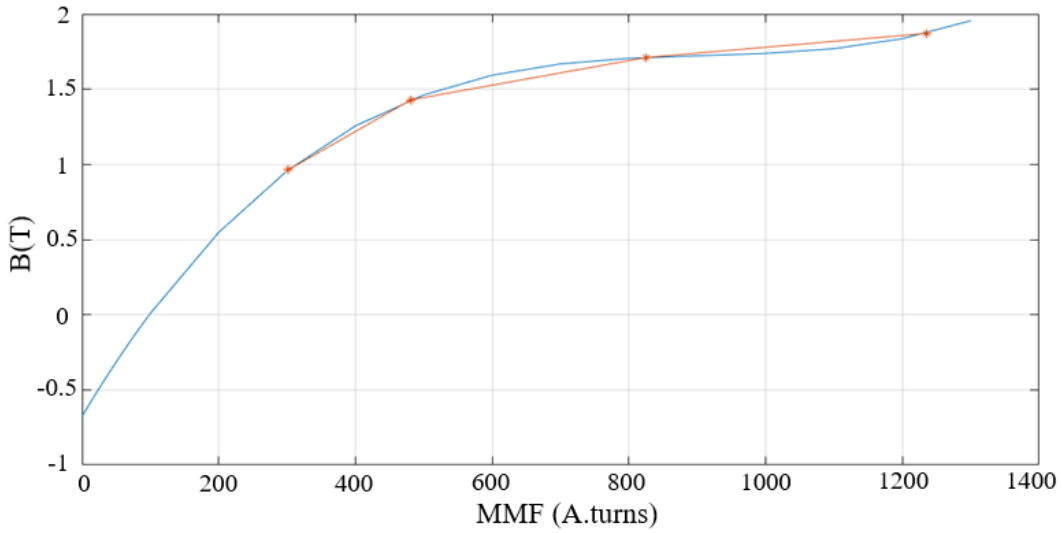

Figure 2.6. B vs MMF (*λ/g=40, t/λ=0.3*). Red dots show the results obtained from Ertan's model, blue line shows the polynomial fitting without necessary corrections

It can be observed from the figure that the fitting requires small fixes to match the real-life model. The initial part requires rearranging and the increase in slope should not happen after the saturation. Applying the steps mentioned above, the obtained final results can be seen below:

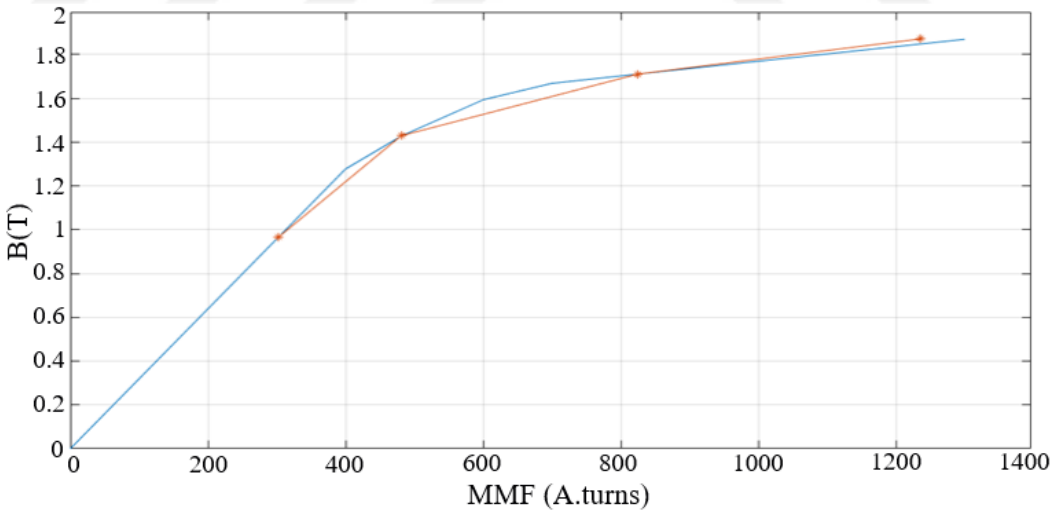

Figure 2.7. B vs MMF (*λ/g=40, t/λ=0.3*). Red dots show the results obtained from Ertan's model, blue line shows the corrected polynomial fitting

The Figure 2.7 shows that the desired linearity and saturation are being obtained without having to compromise from the original results.

2.3. Verification of results

This section will focus on verifying that the proposed methods are accurate. In order to verify that the proposed methods and calculations are accurate, performances of two test motors are to be calculated. It is to be noted that, for comparison purposes, these test motors have been selected as the test motors proposed in [23].

2.3.1. Test motors

The first motor is an 8/6 switched reluctance motor made from M36 steel material that can be found in Middle East Technical University's Electrical Machines Laboratory, which is used for washing machine purposes. This motor will be referred to as SRM1 for better understanding the comparisons with the previous research [23]. The second motor is an 18/12 50kW motor designed to be used in hybrid electrical vehicle applications [3], which will be referred to as SRM2. The core of this motor is made from 10JNEX900 material.

Table 2.1 shows the dimensional parameters of SRM1, Table 2.2 shows the drive specifications of SRM1 and Figure 2.8 shows the geometry of SRM1.

Table 2.1. *Dimensional parameters of SRM1*

Rotor outer diameter	38.6 mm
Stator outer diameter	110.4 mm
Core length	40.4 mm
Stator back-core width	5.2 mm
Shaft diameter	16.5 mm
Air gap length	0.325 mm
Rotor back-core width	3.9 mm
Stator tooth tapering angle	2.215 degrees
Stator tooth width	8.35 mm
Rotor tooth width	8.4 mm
Stator pole depth	30.4 mm
Rotor pole depth	7.2 mm
Number of turns per pole	322 turns
Wire diameter	0.7 mm

Table 2.2. *Drive specifications of SRM1*

Rated power	350W
Rated speed	12500 rpm
DC voltage	300 V
Rated current	3A
Number of phases	4

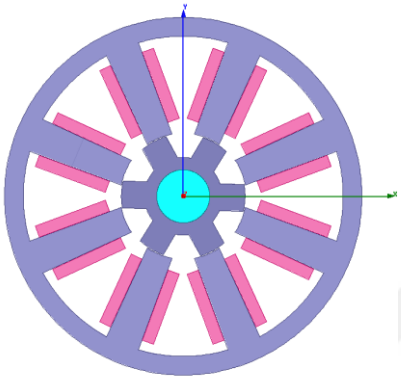

Figure 2.8. Geometry of SRM1

The dimensional parameters for the SRM2 are given in Table 2.3, Table 2.4 shows the drive specifications of SRM2 and Figure 2.9 shows the geometry of SRM2.

Table 2.3. *Dimensional parameters of SRM2*

Rotor outer diameter	179mm
Stator outer diameter	269mm
Core length	135mm
Axial length	155mm
Stator back-core width	17.25mm
Shaft diameter	105.5mm
Air gap length	0.5mm
Rotor back-core width	17.25mm
Stator tooth tapering angle	2.215 degree
Stator tooth width	16.49mm
Rotor tooth width	17.2mm
Stator pole depth	27.25mm
Rotor pole depth	19.5mm
Number of turns per pole	17turns
One strand diameter	0.6mm
Number of strands	22

Table 2.4. *Drive specifications of SRM2*

Rated output power	50 kW
Rated speed	1200-6000 rpm
DC voltage	500 V
Peak current (Per pole)	320 A
Number of phases	3

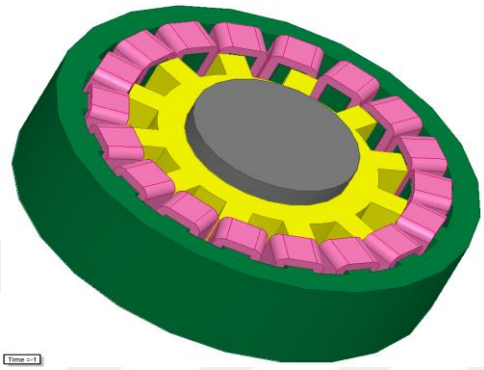

Figure 2.9. Geometry of SRM2

It should be noted that the B-H data of the core materials of SRM1 and SRM2 are given in the Appendices Section A.

2.3.2. Assumptions on the calculations

For the performance calculations, the assumptions made have to be considered. These are the following:

1- Parallel structure for each phase winding is considered.
2- Friction and windage losses have not been considered. Friction torque must be added from Göynük's calculations on pages 123 and 124 of his research [22].
3- End-winding leakage losses of the motor in general have been calculated to have low effect, so the consideration of this loss is optional.
4- Fringing is neglected.
5- Performances of SRM under running condition are considered with chopping.
6- Magnetic shaft effects on the calculations of rotor-back core flux density are not considered.

2.3.3. Verification of results for SRM1

This part focuses on the results obtained for the 8/6 M36 steel SRM1 used for washing machine applications. The obtained results will be compared to previously obtained analytical results in [23], measurement results and the results of Finite Element Method [23].

Initially, the results of the static torque-position-current calculations and flux linkage-current-position calculations of SRM1 are to be compared. Afterwards, the motor performances under steady state running conditions will be simulated and predictions will be compared with the measurements and the previous research results in [23]. These involve instantaneous current, instantaneous torque, efficiency and copper and core losses of the SRM.

2.3.3.1. Results of static torque-position-current calculations of SRM1

The static torque-position-current values of SRM1 is obtained as described in Section 1.4.5 with the data extrapolations explained in Section 2.2.2.1. Torque values at different excitation levels are calculated. These calculations are done between aligned and unaligned positions, normalized position x_n varying between 0 and 1, which correspond to fully aligned in position and fully unaligned out position, respectively. The simulated results displayed at Figure 2.10 start at 0.5A and are increased step by step from bottom to up by a step of 0.5A. The results obtained in [23] can be seen in Figure 2.11.

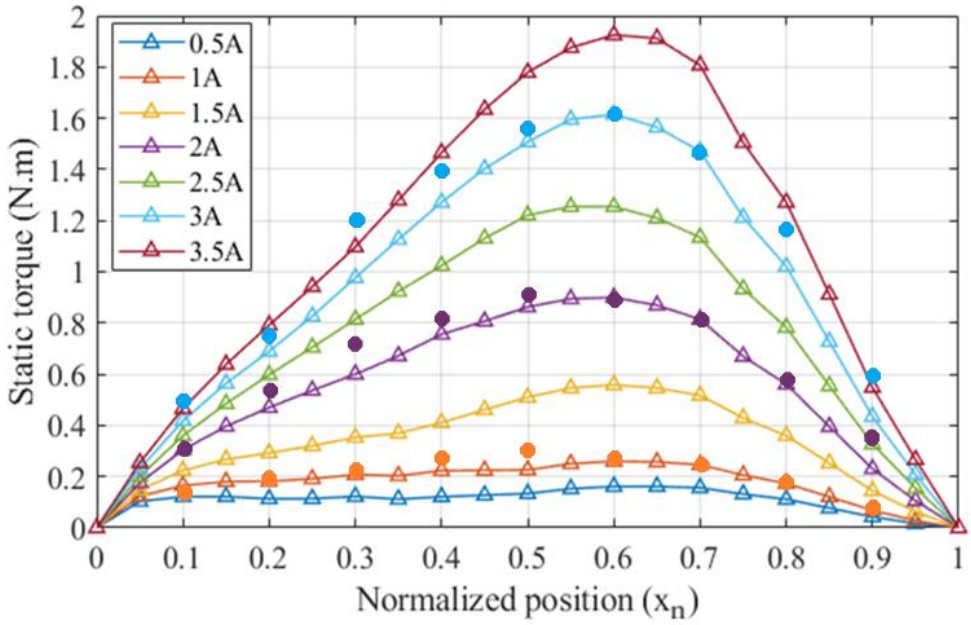

Figure 2.10. Static torque-position-current graph of SRM1 calculated in this research with dots showing measurements at 1A, 2A and 3A excitation values

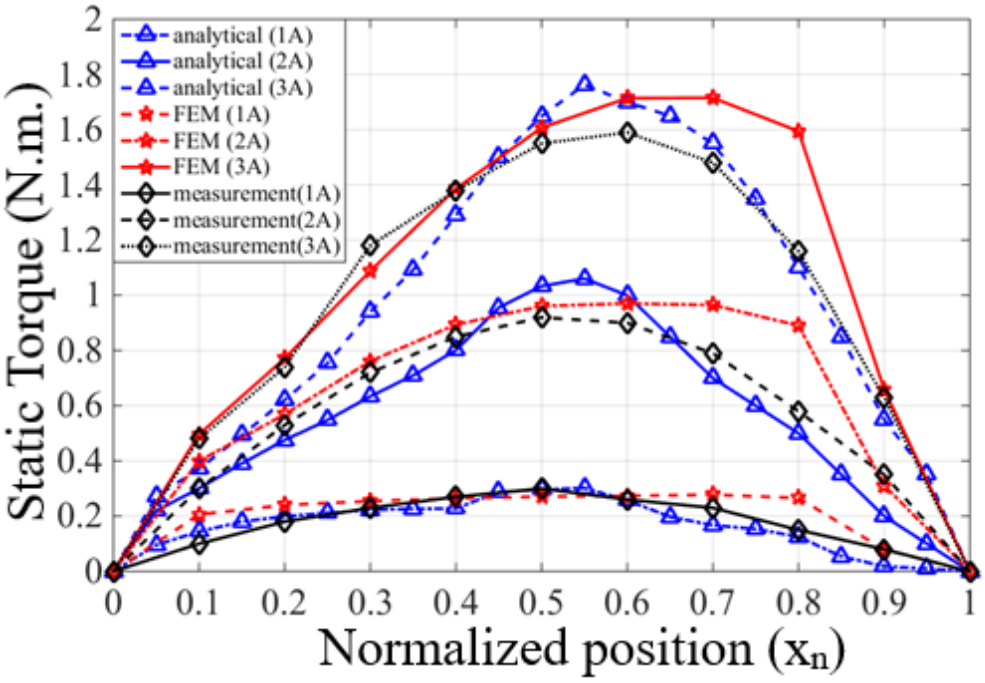

Figure 2.11. Static torque-position-current graph of SRM1 with analytical results, FEM results and measurement results [23]

The torque-position-current graph shown in Figure 2.10 is the torque production of a single phase. For the computation of total torque, overlaps between phase currents, thus torques should be considered and added on top of each other at the operated angles.

Table 2.5. *Static torque data of SRM1 with comparisons (given in N.m.)*

		x_n=0.2	x_n=0.4	x_n=0.6	x_n=0.8
1A	Analytical - [23]	0.2	0.23	0.26	0.13
	Measurement	0.18	0.27	0.26	0.15
	FEM - [23]	0.24	0.26	0.27	0.26
	Analytical - This research	0.18	0.22	0.26	0.17
2A	Analytical - [23]	0.48	0.8	1	0.5
	Measurement	0.53	0.85	0.9	0.58
	FEM - [23]	0.56	0.89	0.97	0.89
	Analytical - This research	0.47	0.76	0.9	0.56
3A	Analytical - [23]	0.62	1.29	1.7	1.1
	Measurement	0.74	1.38	1.59	1.16
	FEM - [23]	0.77	1.39	1.71	1.59
	Analytical - This research	0.69	1.27	1.62	1.02

Comparing the values given at Table 2.5, it can be seen that the obtained results are in a good agreement with the measurement results, and in many points a better approximation to the measurements than the FEM or analytical results of [23], thus concluding the methods and assumptions used in calculations being correct.

2.3.3.2. Results of flux linkage-current-position calculations of SRM1

The flux linkage data versus current at different normalized positions is very important for the determination of the operation cycle. The results obtained for SRM1 flux linkage-current-position values as described in Section 1.4.5 with the data extrapolations explained in Section 2.2.2.2 can be observed in the Figure 2.12. Results obtained at [23] are given in Figure 2.13.

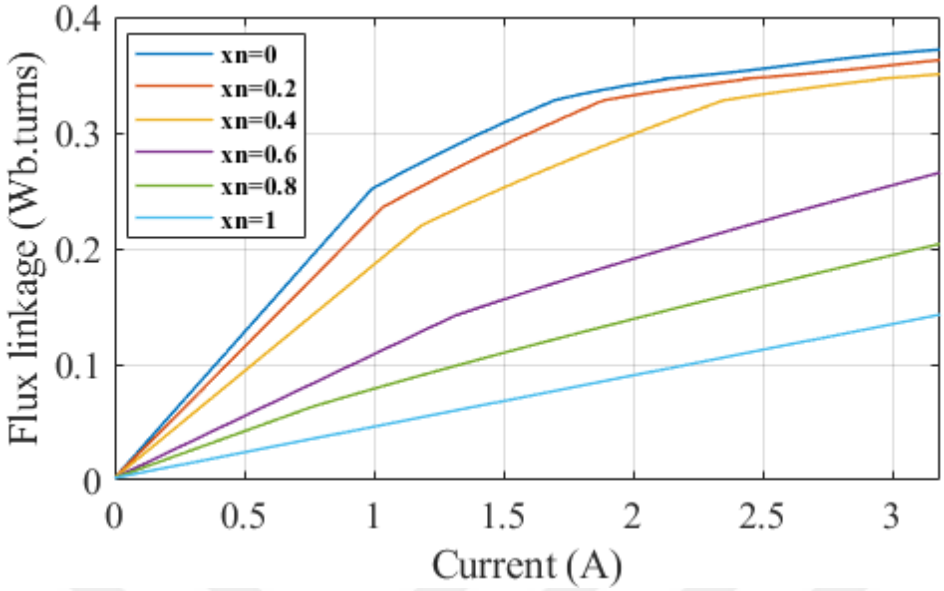

Figure 2.12. Flux linkage-current-position graph of SRM1 calculated in this research

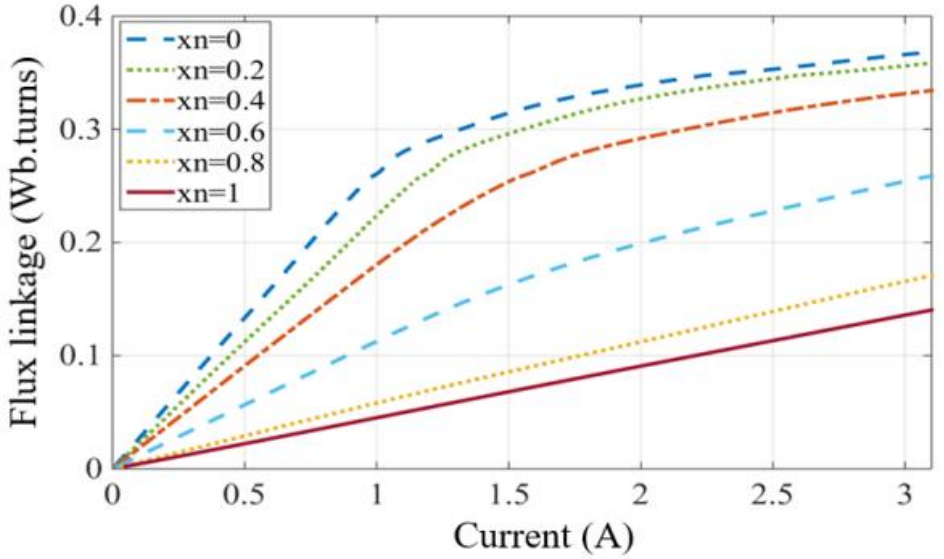

Figure 2.13. Flux linkage-current-position graph of SRM1 from [23]

It is to be noted that neural network method is more precise if applied correctly, however in the cost of hours of computation time.

Table 2.6. *Comparison of SRM1 flux linkage data (analytical, RMxprt and measurements)*

Flux linkage (Wb.turns)		x_n =0	x_n =0.2	x_n =0.4	x_n =0.6	x_n =0.8	x_n =1
1A	Analytical - [23]	0.26	0.22	0.19	0.11	0.06	0.05
	RMxprt - [23]	0.26	0.21	0.17	0.11	0.07	0.05
	Measurement	0.29	0.26	0.2	0.15	0.1	0.08
	Analytical - This research	0.26	0.23	0.19	0.11	0.08	0.05
2A	Analytical - [23]	0.34	0.33	0.29	0.18	0.11	0.09
	RMxprt - [23]	0.34	0.31	0.26	0.18	0.13	0.1
	Measurement	0.42	0.39	0.35	0.28	0.2	0.16
	Analytical - This research	0.34	0.33	0.30	0.19	0.14	0.09
3A	Analytical - [23]	0.37	0.36	0.33	0.25	0.17	0.14
	RMxprt - [23]	0.35	0.34	0.3	0.25	0.19	0.15
	Measurement	0.46	0.44	0.41	0.35	0.28	0.25
	Analytical - This research	0.37	0.36	0.35	0.26	0.20	0.14

Table 2.6. shows the value comparison of the calculated data with that of the data in [23] and the measurement data. It can be seen that the results obtained in this research are in better agreement with the measurement results, though still being in close range of the results in [23]. Slight differences are caused by a more linear approximation used after the extrapolation of data using polynomial fitting. In Section 2.3.3.3, after the addition of slot leakage which is explained in Section 1.4.4, it will be seen that the obtained flux linkage values are much closer to the measured values.

It should be noted that for SRM1, the errors in Tarvirdilu's calculations did not have a big impact on the static torque and flux linkage calculations, and the feed-forward neural networks used in [23] are trained correctly in this case. This has been confirmed after similar results being achieved with the new method used in this research. However, it will be seen in Section 2.3.4 that, especially for the calculations of SRM2, this is not the case and the high errors introduced by feed-forward neural network training will be shown.

2.3.3.3. Results of flux linkage-current-position calculations of SRM1 including slot leakage

In this part, flux linkage introduced by the slot leakage of SRM1 is also considered in determination of flux linkage, as explained in Section 1.4.4. Figure 2.14 shows the resultant flux linkage for SRM1 after the addition of the slot leakage.

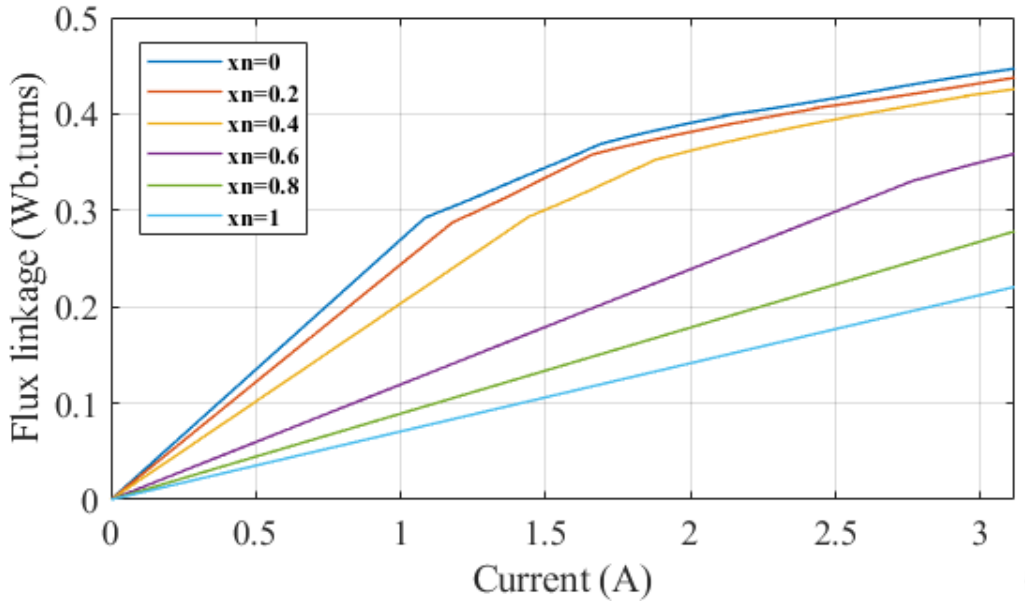

Figure 2.14. Flux linkage-current-position graph of SRM1 calculated in this research including slot leakage

Tarvirdilu [23] has not provided a graphical result for these calculations, thus it cannot be used for the purpose of a visual comparison. However, in [23], the flux linkage including slot leakage data is supplied for different normalized position values under different excitation levels, that can be observed in the Table 2.7. In this table, the analytical method and FEM simulation data obtained in [23] and the measurement results are compared with the results obtained in this research.

Table 2.7. *Comparison of SRM1 flux linkage data including slot leakage calculations*

Flux linkage (Wb.turns)		x_n =0	x_n =0.2	x_n =0.4	x_n =0.6	x_n =0.8	x_n =1
1A	Analytical - [23]	0.29	0.27	0.23	0.14	0.09	0.07
	Measurement	0.29	0.26	0.2	0.15	0.1	0.08
	FEM - [23]	0.28	0.25	0.2	0.15	0.1	0.08
	Analytical - This research	0.28	0.25	0.2	0.13	0.09	0.07
2A	Analytical - [23]	0.4	0.38	0.35	0.25	0.18	0.15
	Measurement	0.42	0.39	0.35	0.28	0.2	0.16
	FEM - [23]	0.4	0.38	0.36	0.29	0.21	0.15
	Analytical - This research	0.4	0.38	0.36	0.24	0.18	0.14
3A	Analytical - [23]	0.44	0.43	0.4	0.33	0.25	0.22
	Measurement	0.46	0.44	0.41	0.35	0.28	0.25
	FEM - [23]	0.44	0.42	0.39	0.33	0.27	0.23
	Analytical - This research	0.44	0.43	0.42	0.35	0.27	0.22

The results of this research can be seen to be in a much better agreement with the measured flux linkage values, compared to the results obtained in Table 2.6. It must be noted that, although the flux linkage results obtained by adding the slot leakage are more accurate, in this specific case, the performances calculated for the running conditions in Section 2.3.3.4 with the exclusion of the slot leakage are found to be more accurate. This is likely due to the relatively small size of the motor, where the leakage becomes insignificant and is compensated in value by the approximations done in calculations.

2.3.3.4. Comparison of the SRM1 performance calculations under running conditions

The performances of the switched reluctance motor under steady state running conditions hold and important place in understanding the operating characteristics. The calculations of these performances are highly dependent on the control methods and drive characteristics.

The 8/6 SRM1 performances under running conditions will be calculated at 500 rpm and 1000 rpm. The control characteristics for these speeds are given at Table 2.8 and Table 2.9.

Table 2.8. *Control characteristics of SRM1 at 500rpm*

Maximum chopping current (I_{max})	3.1 A
Minimum chopping current (I_{min})	2.9 A
Excitation period	0.5 p.u.
Phase turn on angle (θ_{on})	-45 degrees electrical
Speed	500 rpm

Table 2.9. *Control characteristics of SRM1 at 1000rpm*

Maximum chopping current (I_{max})	3.2 A
Minimum chopping current (I_{min})	2.8 A
Excitation period	0.5 p.u.
Phase turn on angle (θ_{on})	-45 degrees electrical
Speed	1000 rpm

Referred to as advance angle, turn on angle or firing angle (θ_{on}), which is the electrical angle at which phase is excited, is selected in order to allow current enough time to rise. This angle can be seen in Figure 2.15. The excitation (conduction) period is the duration in electrical degrees for which the phase stays excited after being fired.

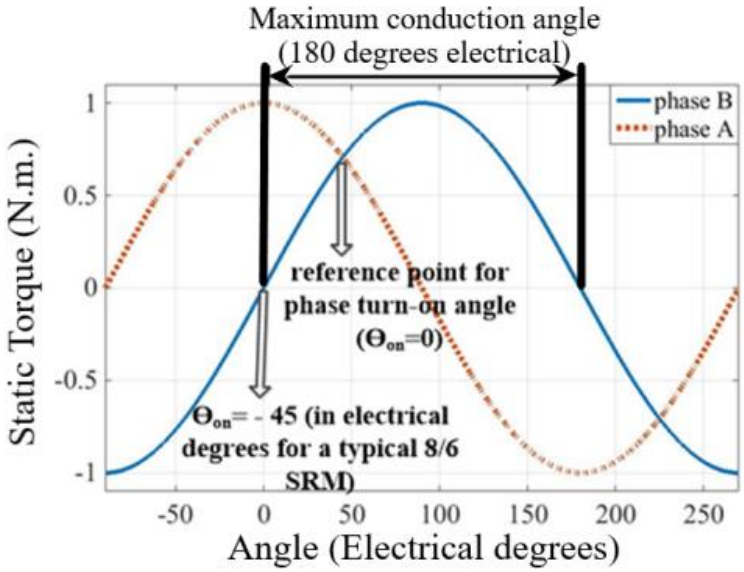

Figure 2.15. Ideal consecutive torque graph and turn on angle of an 8/6 SRM

The instantaneous phase current values are calculated as described in Section 1.4.6. The obtained calculation results of SRM1 are compared with the previous calculations and measurement results for understanding the accuracy. Correct prediction of phase currents will mean that the resultant instantaneous torque calculations are also accurate.

Figure 2.16 shows the result obtained in this research, Figure 2.17 is the result obtained in [23], and Figure 2.15 is the measurement result. It should be noted that all three result are acquired with a -45 degrees electrical turn on angle and electrical conduction angle corresponding to 0.5 per unit at 1000 rpm.

The rise time of the current is taken as the time for the current to reach from 0.1 of the maximum value to 0.9 of the maximum value. The rise time of the calculations shown in Figure 2.16 corresponds to 0.54 milliseconds. The chopping frequency of the controller circuit is 2.19kHz.

Through comparison of the calculated and measurement results, it can be seen that the calculations in Figure 2.16 are in a good agreement with the measurement results seen in Figure 2.18, whereas the results obtained in [23] which can be seen in Figure 2.17 show an initial drop on the chopping current through a high inductance which is not observed in the real case. This holds to be another proof showing that the corrections made give out results that are parallel to the measurements.

Next, the instantaneous current results obtained at 500 RPM with -45 degrees electrical phase turn on angle and 0.5 per unit conduction angle for SRM1 are shown. Figure 2.19 shows the result obtained in this research and Figure 2.20 and Figure 2.21 correspond to the analytical calculations and FEM calculations in [23], respectively. It is important to note that speed, turn on angle and conduction period are the same in these figures.

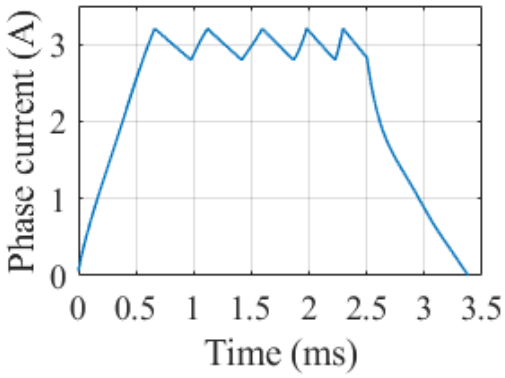

Figure 2.16. Phase current vs time of SRM1 calculated in this research at 1000 rpm with a conduction angle 0.5 p.u. fired at -45 degrees electrical

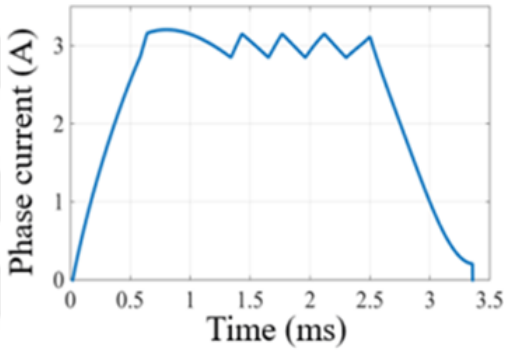

Figure 2.17. Phase current vs time of SRM1 at 1000 rpm with a conduction angle 0.5 p.u. fired at -45 degrees electrical calculated in [23]

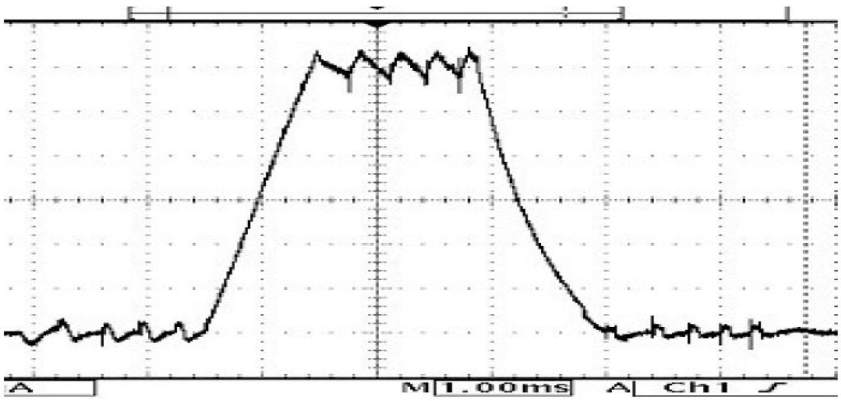

Figure 2.18. Measured current of SRM1 at 1000 rpm with a conduction angle 0.5 p.u. fired at -45 degrees electrical

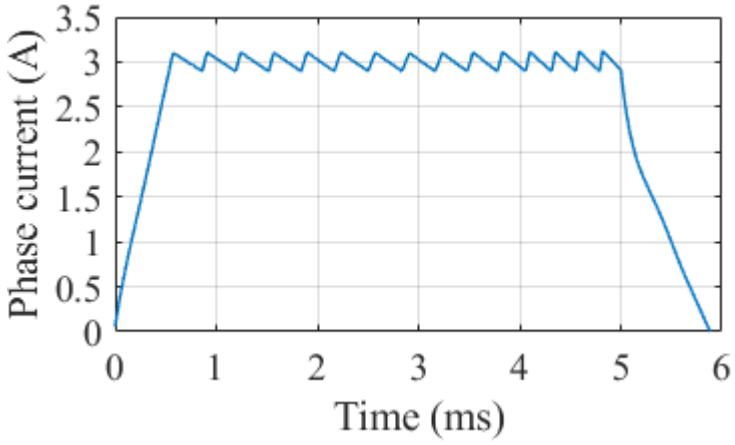

Figure 2.19. Phase current vs time of SRM1 calculated in this research at 500 rpm with a conduction angle 0.5 p.u. fired at -45 degrees electrical

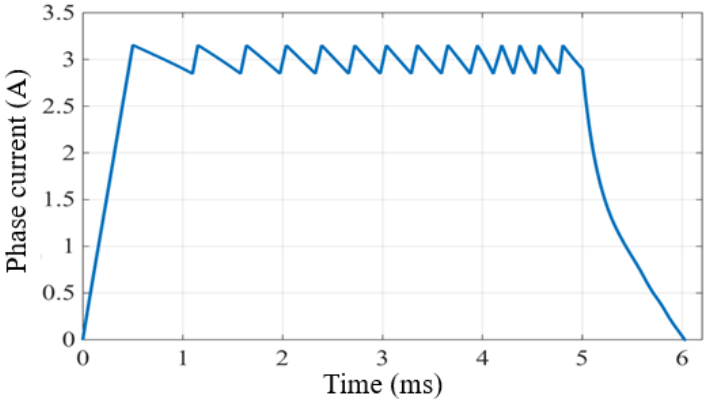

Figure 2.20. Phase current vs time of SRM1 at 500 rpm with a conduction angle 0.5 p.u. fired at -45 degrees electrical calculated in [23]

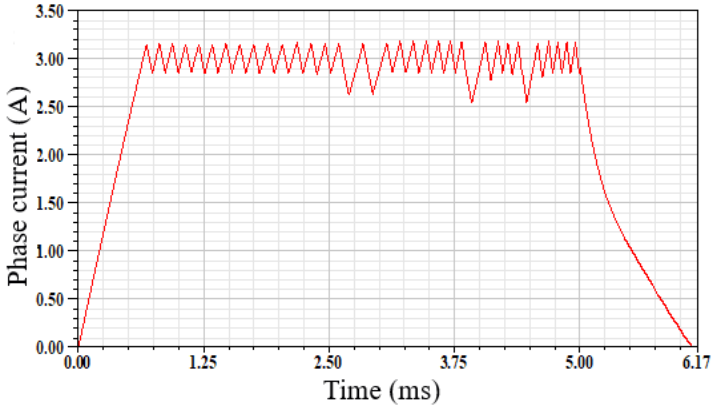

Figure 2.21. Phase current vs time of SRM1 at 500 rpm with a conduction angle 0.5 p.u. fired at -45 degrees electrical obtained by finite element method in [23]

The rise time of the current in Figure 2.19 is taken as the time for the current to reach from 0.1 of the maximum value to 0.9 of the maximum value. This time corresponds to 0.474 milliseconds. The chopping frequency of the controller circuit is 3.45 kHz.

The comparison of the obtained results with the analytical results obtained in [23] show that the found instantaneous current results are in good agreement. Unfortunately, there is no measurement data to be compared with. To understand the accuracy, calculated and measured values of rms currents are compared in Table 2.10.

Figure 2.22 shows the result of the calculated instantaneous torque for SRM1 as explained in Section 1.4.6. Figure 2.23 shows the results obtained in [23].

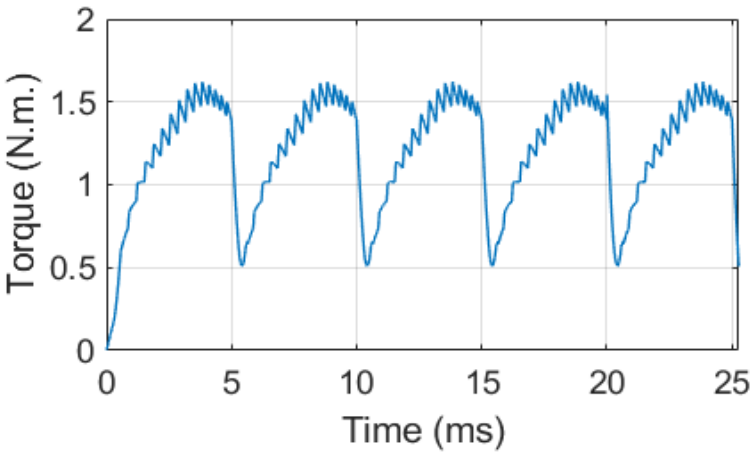

Figure 2.22. Total torque vs time prediction of SRM1 at 500 rpm obtained in this research

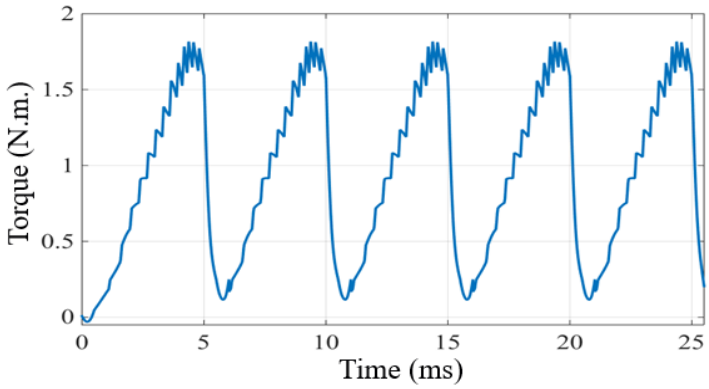

Figure 2.23. Total torque vs time of SRM1 at 500 rpm [23]

It is very difficult to measure the instantaneous variation of torque as this is the electromagnetic torque. The load inertia affects the torque value, only after which the torque value can be measured. The goodness of the curves given in Figure 2.22 and Figure 2.23 are to be compared on the basis of average value of the measured torque and predicted value of the torque as given in Table 2.10.

Table 2.10 presents average torque calculations at 500 rpm as well as comparisons of rms current, input power, output power and losses of the motor.

Table 2.10. *SRM1 performance calculation results at 500 rpm (θ_{on}=-45 degrees electrical and conduction angle=0.5 p.u.)*

	Speed (rpm)	Average torque (N.m.)	RMS current (A)	Output power (W)	Copper loss (W)	Core loss (W)	Total loss (W)	Input power (W)	Torque ripple (%)	Efficiency (%)
Analytical - [23]	500	1.19	1.45	62.4	43.69	29	72.69	135.1	93.4	46.1
FEM simulations - [23]	500	1.23	1.49	64.37	46.5	31	77.5	141.8	88	45.4
Measurements	500	1.25	-	65.45	-	-	-	-	-	-
Analytical - This research	500	1.23	1.48	64.4	45.29	33.75	79.04	143.44	68.5	44.8

From the results in Table 2.10, it can be seen that the calculated average torque is closer to the measurements than the previous analytical results in [23]. A higher torque indicates higher rms current and thus higher losses, resulting with a slightly lower efficiency. That is the result observed in the results of this research, thus concluding that the methodology used is a good way of predicting the operation of the SRM.

For further testing the accuracy, the results obtained at 1000 rpm with a conduction period of 0.5 per unit and turn on angle of -66 degrees electrical are calculated and compared. These results can be seen at Table 2.11.

Table 2.11. *SRM1 Performance calculation results at 1000 rpm (θ_{on}= -66 degrees electrical and conduction angle=0.5 p.u.)*

	Speed (rpm)	Average torque (N.m.)	RMS current (A)	Output power (W)	Copper loss (W)	Core loss (W)	Total loss (W)	Input power (W)	Efficiency (%)
Analytical – [23]	1000	0.93	1.45	97.4	43.7	34.5	78.2	175.6	55.47
Measurements	1000	0.84	1.36	88	38.5	-	-	-	-
Analytical – This research	1000	0.915	1.46	95.9	44.3	37.1	81.4	177.3	54.1

The average torque at 1000 rpm is found to be closer to the measured results, and the calculations are in close boundaries of the calculations obtained in [23]. It again should be noted that the errors in [23] have very small effects on the performance calculations in case of SRM1, as the motor size is considerably small. This is not the case in SRM2 performance calculations.

The calculations done at two different speeds of 500 rpm and 1000 rpm show that the methods used in this research give accurate results, thus concluding that the calculations are trustable.

2.3.4. Verification of results of SRM2

This section focuses on the three phase 18/12 50kW motor referred to as SRM2, which is used in hybrid electrical vehicle applications [3]. The obtained results will be compared to the previous calculation and FEM simulation results of [23] as well as the measurement results.

Firstly, the results of the calculations of static torque-position-current values and flux linkage-current-position values will be given and compared for the SRM2. Afterwards, the results for instantaneous phase current values, instantaneous torque predictions, efficiencies and losses are to be compared.

2.3.4.1. Results of static torque-position-current calculations of SRM2

For the static torque-position-current calculations of SRM2, excitations at different current levels are calculated and corresponding torque values are found, as mentioned in Section 1.4.5 with the data extrapolations explained in Section 2.2.2.1. These calculations are done between aligned and unaligned positions, normalized position x_n varying between 0 and 1, which correspond to fully aligned in position and fully unaligned out position. The simulated results at Figure 2.21 start at 240A and are increased step by step from bottom to up by a step of 120A. These results will be compared with the results obtained in [23].

Following figures show the results obtained. Figure 2.24 shows the static torque-position-current graph for this research and Figure 2.25 shows the FEM simulations and analytical results obtained in [23].

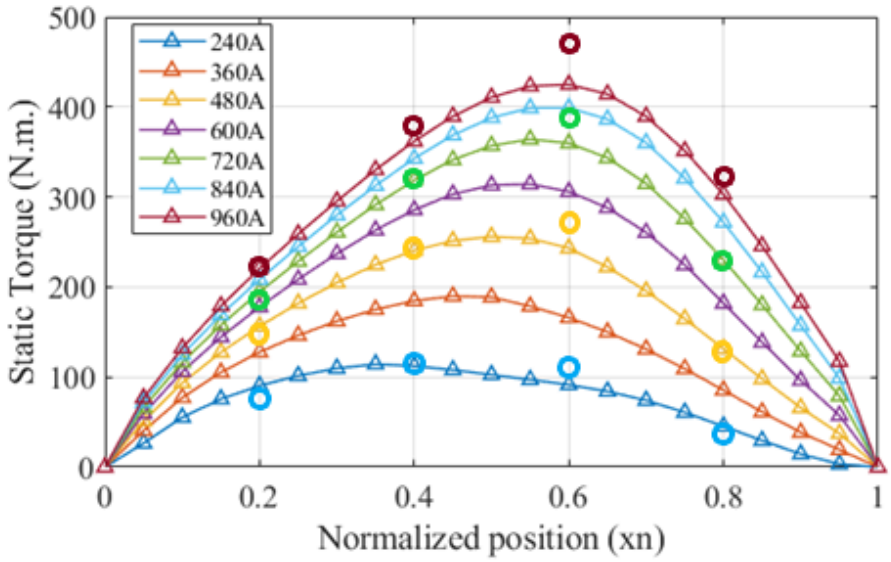

Figure 2.24. Static torque-position-current graph of SRM2 obtained in this research where the circles show comparisons with the FEM calculations

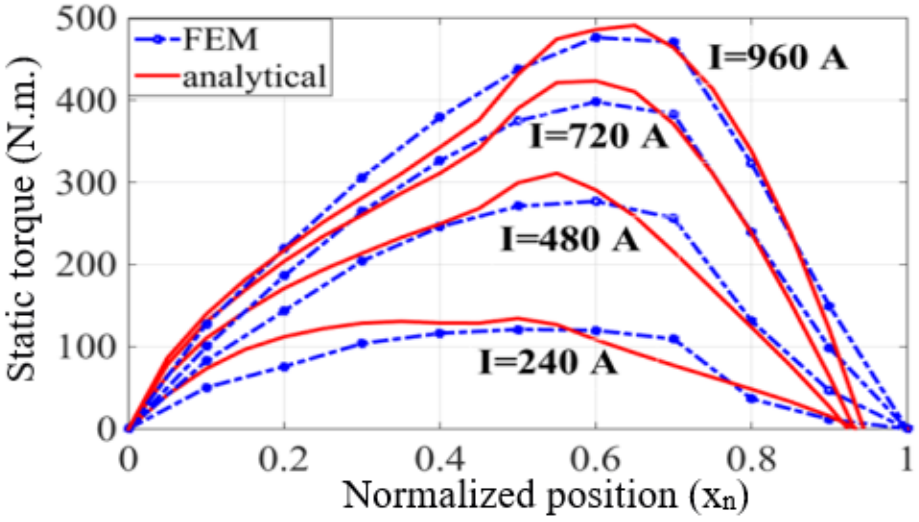

Figure 2.25. Static torque-position-current graph of SRM2 obtained in [23]

Comparing the results, it can clearly be seen that the analytical results proposed in [23] are faulty and reach zero torque value before the unaligned position is reached. The results found in Figure 2.24 are closer to the results found by finite element method, which in results given in Table 2.13 have been seen to be more accurate.

Thus, concluding that the results are trustable. It should be noted that there is no dataset provided in [23] for comparison of static torque-position-current values.

2.3.4.2. Results of flux linkage-current-position calculations of SRM2

The results of flux linkage-current-position calculations of SRM2 as described in Section 1.4.5 with the data extrapolations explained in Section 2.2.2.2 can be seen in Figure 2.26. In addition, Figure 2.27 shows FEM and analytical calculations in [23] as well as measurement results.

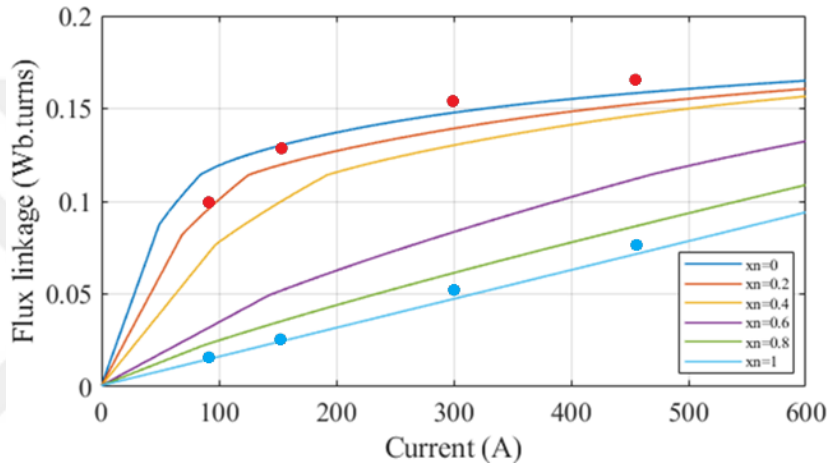

Figure 2.26. Flux linkage-current-position of SRM2 calculated in this research without the addition of slot leakage, dots show measurements for x_n=0.2 and x_n=1

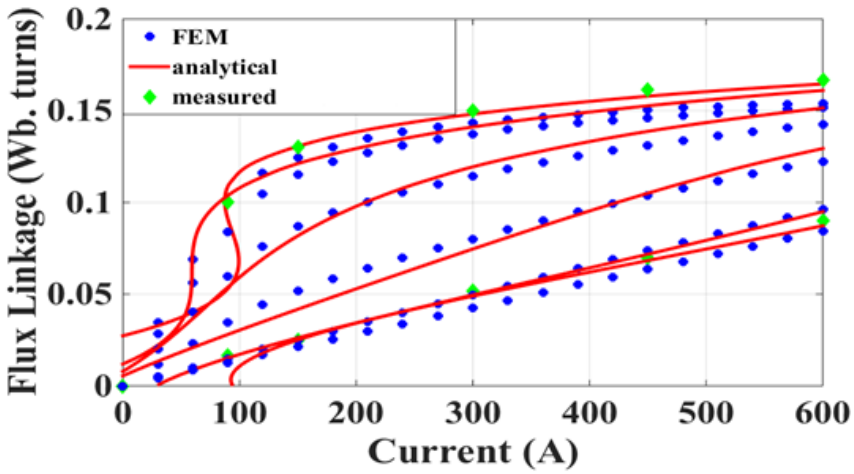

Figure 2.27. Flux linkage-current-position of SRM2 supplied in [23], green dots show measurements for x_n=0.2 and x_n=1

It needs to be noted that the SRM has a linear unsaturated flux linkage-current value, corresponding to a fixed linear inductance for each normalized position before saturation. Analytical calculations for the flux linkage-current-position values of SRM2 that are done in [23] and given in Figure 2.27 are highly faulty for unsaturated region and it is impossible to figure the inductance using the slope of flux linkages of [23]. These problems are not encountered in the results of this research.

It can be observed that the flux linkage results without the slot leakage obtained in Figure 2.23 are behind the measured values, especially observed in x_n=0.2 position through the help of measurement results.

The flux linkage-current-position values obtained when the slot leakage mentioned in Section 1.4.4 is also included are given in Figure 2.28. These results are not supplied in [23], so the comparison cannot be done. However, these are the flux linkage values used for the calculations of SRM2 and can be seen to be in a much better agreement with the measured results. It will be seen in Table 2.13 that the resultant performance calculated from these data is much closer to the measurements, leading to the conclusion that the polynomial fitting and described corrections have led to the correctly estimated flux linkage values.

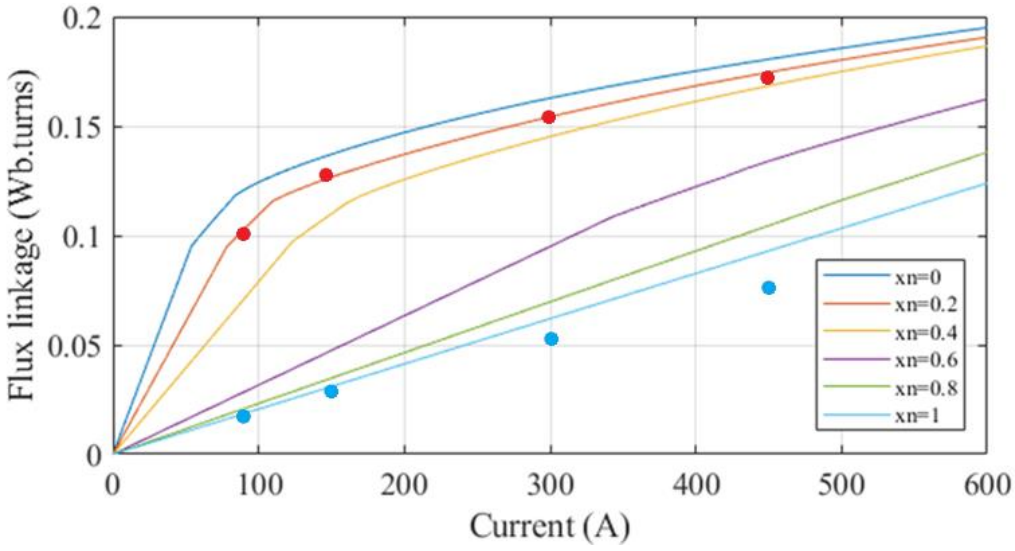

Figure 2.28. Flux linkage-current-position of SRM2 calculated in this research with the addition of slot leakage, dots show measurements for xn=0.2 and xn=1

2.3.4.3. Comparison of the SRM2 performance calculations under running conditions

This part focuses on the instantaneous current and instantaneous torque results obtained for SRM2 as explained in Section 1.4.6. For this purpose, the control characteristics are given at which the results are obtained and compared. Below are the control characteristics of SRM2 given at Table 2.12.

Table 2.12. *Control characteristics for SRM2*

Maximum chopping current (I_{max})	320 A
Minimum chopping current (I_{min})	300 A
Excitation period	0.83 p.u. (150 degrees electrical)
Phase turn on angle (θ_{on})	- 4 degrees electrical
Speed	1200 rpm

Following Figure 2.29 shows the current vs time calculation results for the SRM2 under the control characteristics given in Table 2.12.

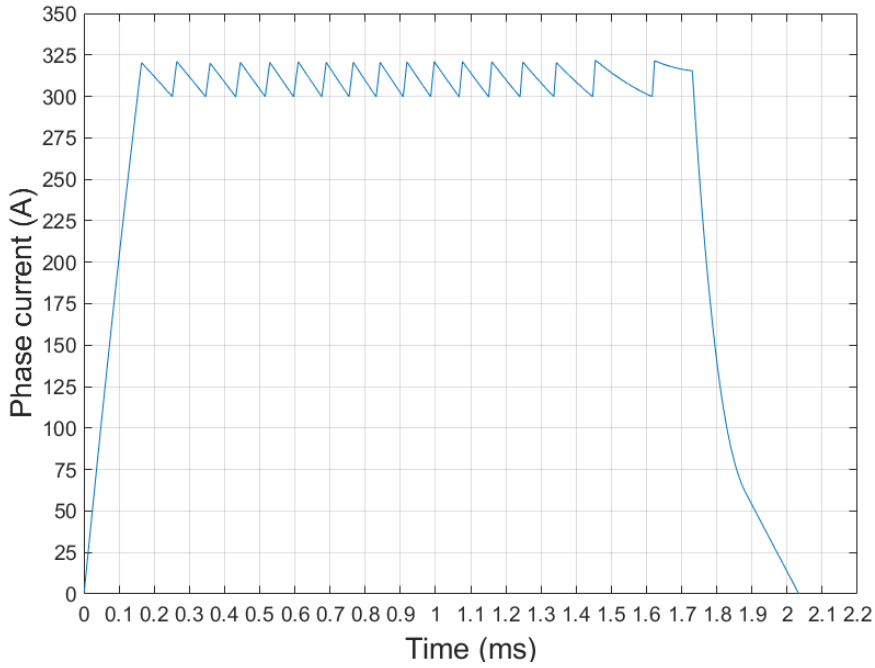

Figure 2.29. Current vs time of SRM2 calculated in this research at 1200 rpm, 0.83 p.u. conduction angle and -4 degrees electrical turn on angle

The rise time of the current given in Figure 2.29 is 0.131 milliseconds and the initial chopping frequency of the controller circuit is 11.63 kHz. It needs to be noted that the chopping frequency decreases as the phase inductance increases with increasing overlap. The data supplied by Tarvirdilu [23] does not include the instantaneous current of SRM2 for comparison, but the rms values of the currents are compared at Table 2.13. It can be seen that the calculated rms current is much closer to the measured value when compared with the calculations done in [23].

Figures 2.30 and 2.31 show the predicted instantaneous torques for this research and previous calculations in [23], respectively. It should be noted that in a three phase 18/12 switched reluctance motor there are 3 pole pairs excited at the same time. Torque calculated in Figure 2.27 shows the total torque production of three pole pairs. Torque ripples observed are due to the overlaps of rising and falling currents.

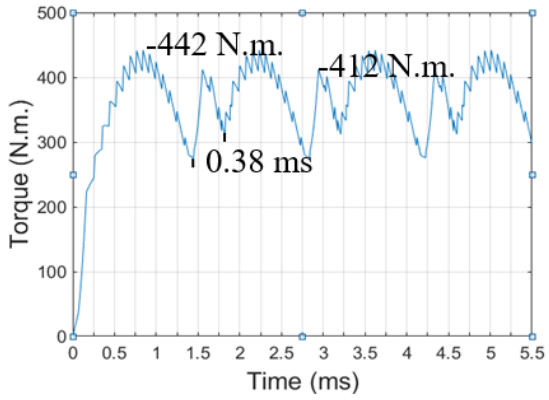

Figure 2.30. Total torque vs time of SRM2 predicted in this research at 1200 rpm

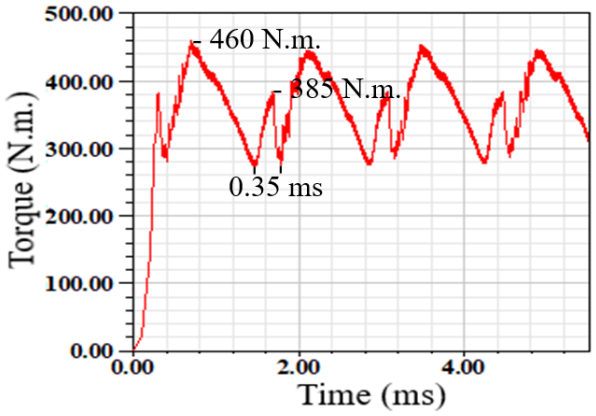

Figure 2.31. Total torque vs time of SRM2 predicted with FEM simulations at 1200 rpm in [23]

It again needs to be stated that as the change of electromagnetic torque against time cannot be measured, thus the prediction given in Figure 2.30 will be validated by comparisons over the average torque values. Looking at the performance results obtained which is given in Table 2.13, it can be clearly seen that the calculated average torque is considerably closer to the measured data, unlike the analytical calculation results of [23], thus can be seen that the calculations are in good agreement with reality.

The calculated performance values of SRM2 with the measurement data and previous calculations of [23] are given at Table 2.13.

Table 2.13. *SRM2 Performance calculation results*

	Speed (rpm)	Average torque (N.m.)	Output power (kW)	RMS current (A)	Copper loss (kW)	Core loss (kW)	Total loss (kW)	Input power (kW)	Efficiency (%)
Analytical - [23]	1200	406.6	51.1	190	12.23	1.044	13.274	64.37	79.4
FEM simulations - [23]	1200	364	45.74	191.3	12.42	1.255	13.675	59.42	77
Measurement results	1200	366	45.99	206	-	-	-	-	-
Analytical - This research	1200	371.3	46.65	196.8	13.49	1.38	14.87	61.52	75.83

It needs to be stated that Tarvirdilu in his calculations [23] has forgotten to multiply the core losses by 3, as there are 3 pole pairs simultaneously excited at a given time, and his calculations of core losses have been only for one pole pair. In Table 2.14, these mistakes have been corrected for his research [23], in order to better understand the comparisons between the two research.

The results of this research given in Table 2.13 indicate much more comparable results with the measurements compared to previously carried out analytical values of [23]. Average torque is considerably closer to the measurements. The rms current is closer to the real rms current observed on the motor, thus again concluding that the losses would be higher and the efficiency lower than previously calculated values. With the comparisons at hand, it can be concluded that the results are trustable.

CHAPTER 3

SWITCHED RELUCTANCE MOTOR ANALYSIS PROGRAM

3.1. The aim of the chapter

This chapter focuses on improvement of the capabilities of a switched reluctance motor analysis and optimization program and how it has been established. There have been many work in METU Electrical and Electronics Engineering Department on the performance of switched reluctance motors [6, 13, 14, 18-23, 25]. However, up to this date, the software algorithms created under the light of these research have usually been lost or not easy to use because of unavailable user manual or other reasons. One of the main reasons being the sustainability and the life span of the programs used, and the other main reason being the unclarity of the codes used for calculations done via MATLAB or other programs. The software developed here is mainly the user interface and calculations are carried out by calling MATLAB based calculation algorithm. The MATLAB code has been previously developed by Tarvirdilu [23], and is edited in this research with the changes described in Chapter 2, along with many corrections to the implementation of the calculation algorithms.

3.2. Previous applications and the necessity of this program

Under METU Electrical and Electronics Engineering Department, for SRM performance calculations, there has only been one interface developed by Göynük in 2008 [22], and the other software in general remained as a compilable MATLAB code. Göynük created a program for the performance calculations of a switched reluctance motor using a development software called Borland Delphi and coded the interface and calculations in Pascal language. Though working, the calculations and the interface has many shortcomings and flaws.

The initial idea in this study has been to edit the existing user interface program created by [22], by first analyzing Göynük's research, re-evaluating his calculations through the research conducted by [23] and improving the interface. However, after a thorough research of Göynük's thesis and inspection of the program he created, this has proven to not be useful. Given next are the reasons why this is decided.

1- Göynük's calculations in [22] have been observed to be not as precise as desired as the normalized data is created for lesser amount of normalized positions and MMF values than desired.
2- Running condition performances of the SRM are not calculated.
3- There is no research or code implementation for optimization purposes.
4- The interface program that has been used, Borland Delphi, has been sold to another company named Embarcadero, which means the previous versions of Borland being unsupported. The new version of the program has been tried with the code used in [22]. However, the Pascal language has also evolved and many of the libraries necessary for the compilation of Göynük's code are no longer supported and cause errors in compilation.
5- Existing software can plot only the flux linkage-current-position graph and torque-position-current graph.
6- Only two specific core materials are available for selection.
7- The graphs lack the zoom property and the data is only shown as a graph, i.e. the data values cannot be examined at desired points.
8- The data entered or loaded are not checked for errors, which means slight mistake would cause the program to crash directly.
9- The interface is not user-friendly.

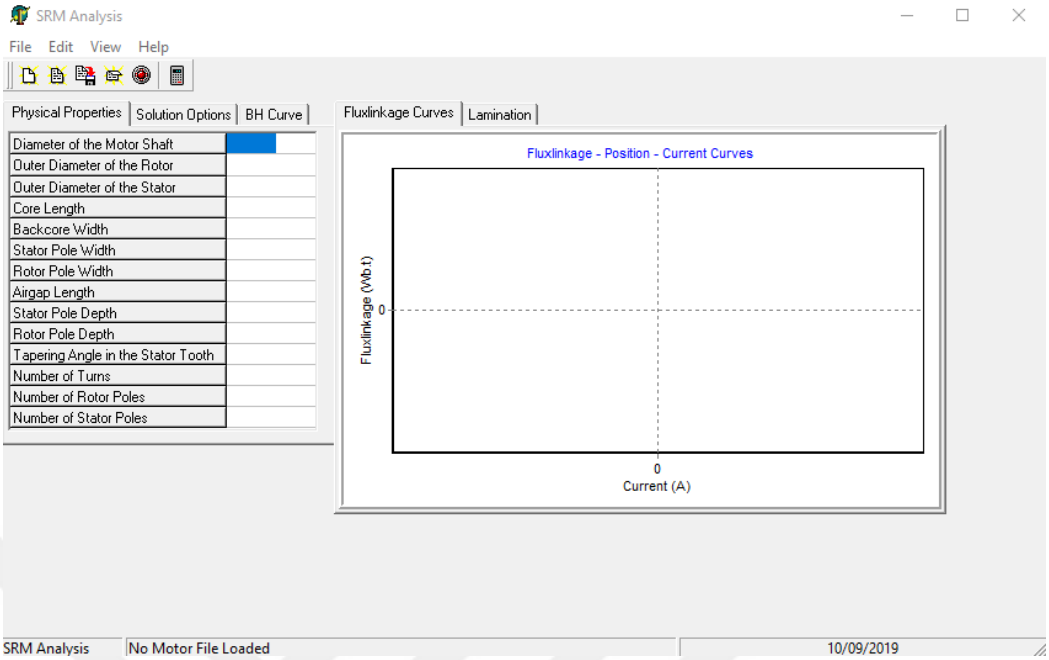

Figure 3.1. Göynük's analysis interface for the SRM [22]

The unsustainability and the errors of [22] has led to a research for finding the optimal development software and language. Microsoft's Visual Studio has been chosen as the new interface program, as Microsoft itself creates all its operating system through this software, thus ensuring the life span of the program for further support and compatibility. The development language has been chosen as C#, as it has many readily built packages and the language being a new and highly used, highly supported language in interface creations.

The next idea has been on the creation of a stand-alone executable done on MS Visual Studio. Initially, the performance and optimization calculations of the SRM have been transferred into MS Visual Studio with conversions into C# language. However, this has proven to be very time consuming and very hard for the next person to continue the research to make alterations on. Also, this would require additional packages to be included in the program for calculational purposes, as Visual Studio does not include the calculation libraries. Including these packages would also make the program unavailable for licensing under the department. Furthermore, the precisions of calculations are not as high as in other specialized programs.

Final choice has been made on using Microsoft Visual Studio to create the interface and conduct the calculations in a MATLAB. A MATLAB ‘m’ file is constructed for the calculations, which can be considered as a text document read by MATLAB. It is very easy for the user to make additions or alterations on, and the necessary input and output parts can be made to be clearly seen when fitted into a function. The use of Visual Studio as interface also allows for changes to be easily made on the interface. Both of the development software are very commonly used by the engineering society and have a long life span, which are additional reasons contributing to the selection of these programs.

With these information taken into account, the new program has been created, and will be explained in the following sections.

3.3. The new interface and the calculation program

This part focuses on understanding the new interface. It has been created under the supervision of H. Bülent Ertan and is specifically made to answer the specifications set.

Initially, there is a short splash screen that shows while the background codes compile and the program becomes ready.

Afterwards, the user comes across a screen to choose which machine to operate on. In this thesis, only switched reluctance motors are given as an option. The next positions are reserved for further research and can be easily utilized for other machines to be analyzed under the same program. Figure 3.2. given on the following page shows this interface.

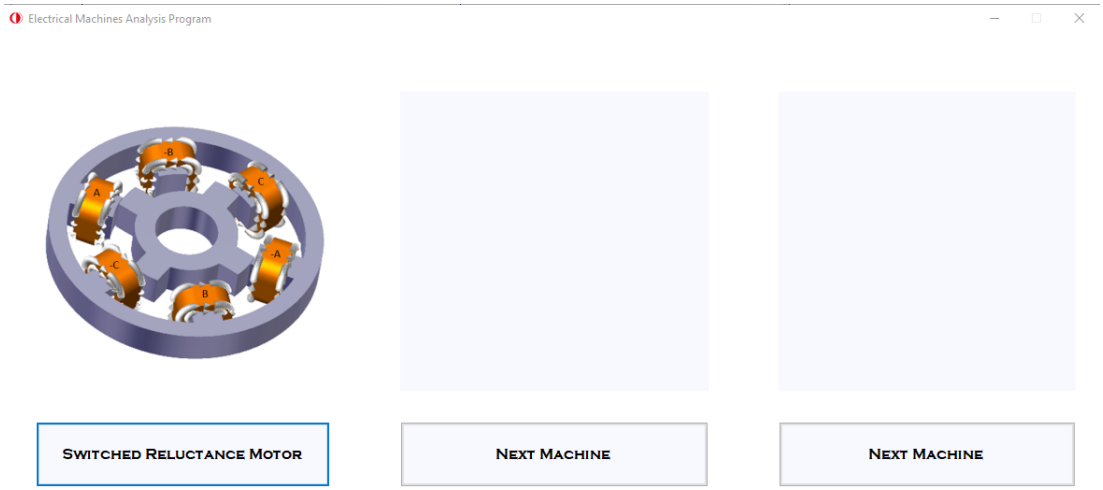

Figure 3.2. Initial interface of the developed program for choosing which machine to operate on

The interface for switched reluctance motor performance calculation and optimization has been created to have a simple but efficient and user-friendly interface. The interface can be observed at Figure 3.3.

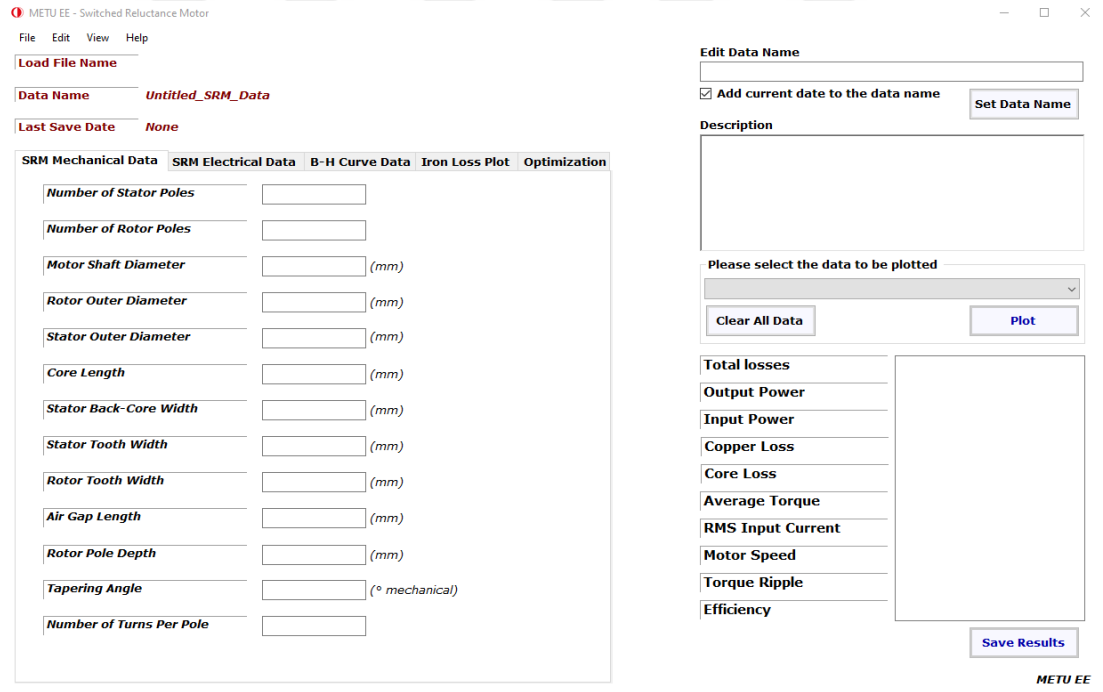

Figure 3.3. SRM interface created for performance calculations and optimization

3.3.1. Data input interface for performance calculation

There are five different tabs that serve different purposes, which are located on the lower left part of the main interface that can be seen in Figure 3.3. The first tab, which is open by default when the program is opened, is for the user to enter the mechanical parameters of the motor. All the data entries in the program are checked to be of correct format. An example would be number of poles being checked to be positive integers, or the dimensions being checked to be non-negative double values. Zero value is also checked as tapering angle can be zero, but shaft diameter cannot attain zero value. If an input error is confronted, user is given a warning on the specific type of error and asked to re-enter the value in specified format. The value can be entered with a comma or a dot for decimal values, the interface automatically corrects the format into the required dot for the calculations.

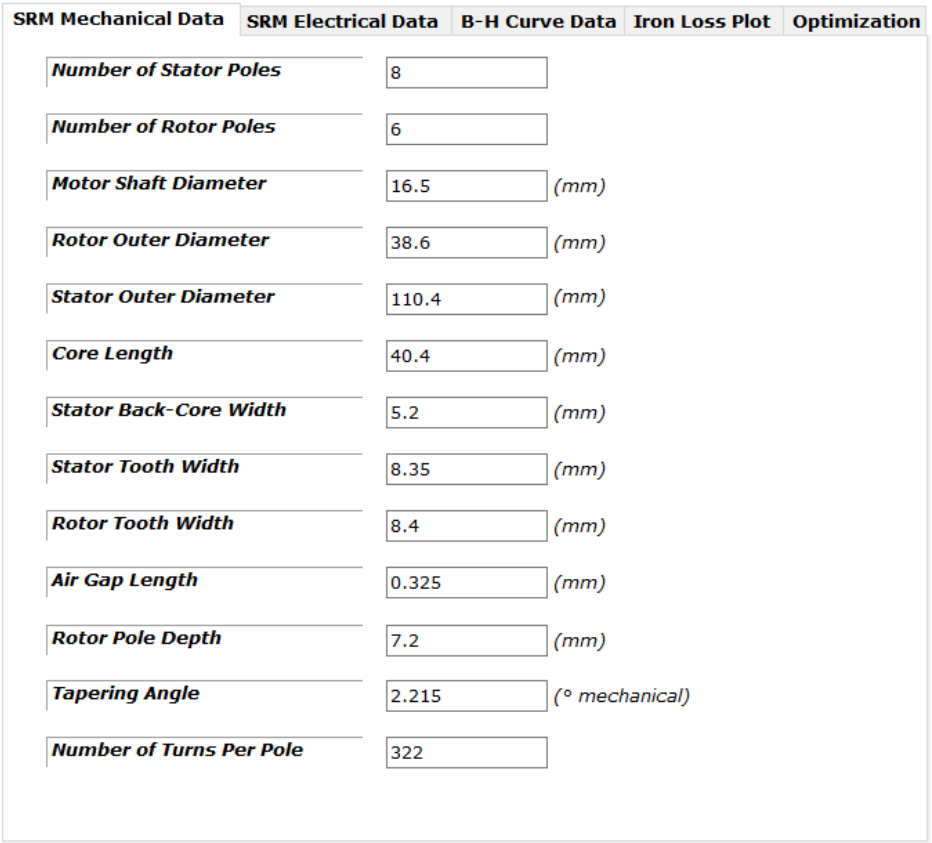

Figure 3.4. Tab 1 - Data entry interface for the mechanical parameters

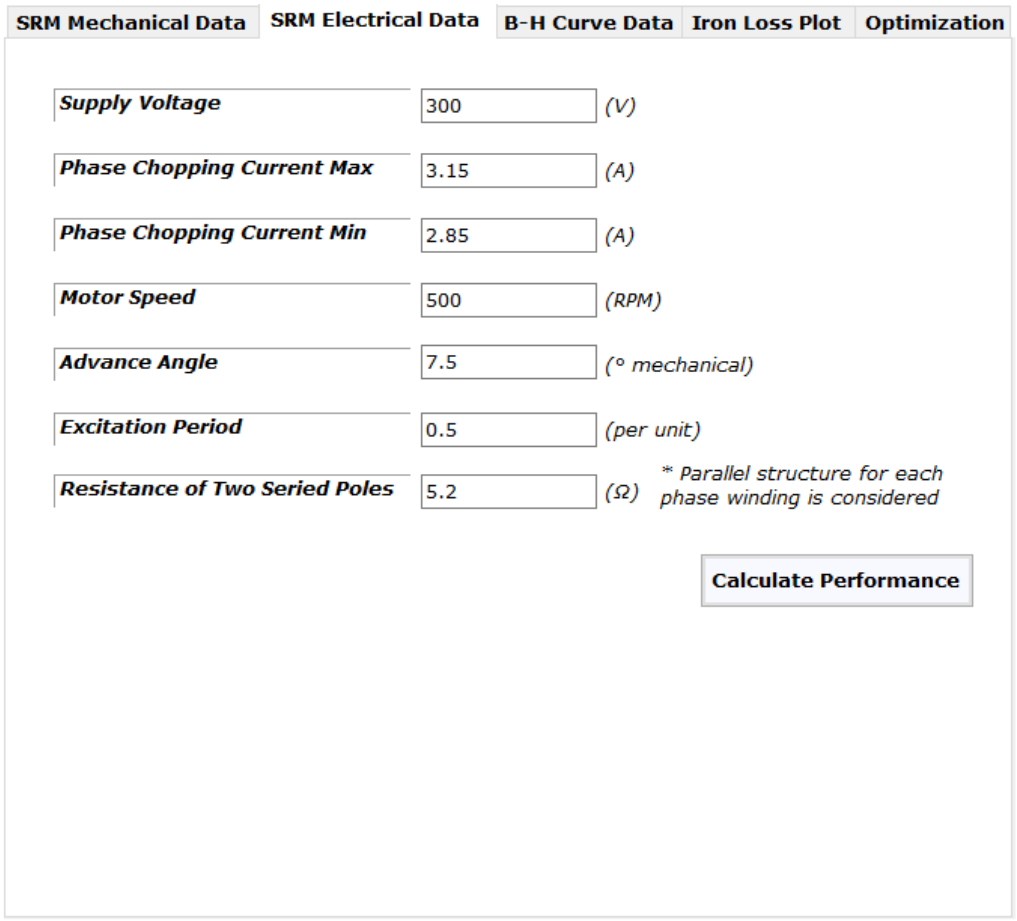

Figure 3.5. Tab 2 - Data entry interface for the drive and other electrical parameters

The second tab which is shown in Figure 3.5 allows the user to input the electrical data and drive characteristics of the switched reluctance motor. After entering the mechanical dimensions, electrical data and B-H curve data, the user is able to calculate performance of the SRM through this tab by clicking the performance calculation button. If any data is missing when performance calculation button is clicked, program focuses the user on the necessary missing data and asks it to be filled. This ensures that the program works correctly and does not encounter a crash.

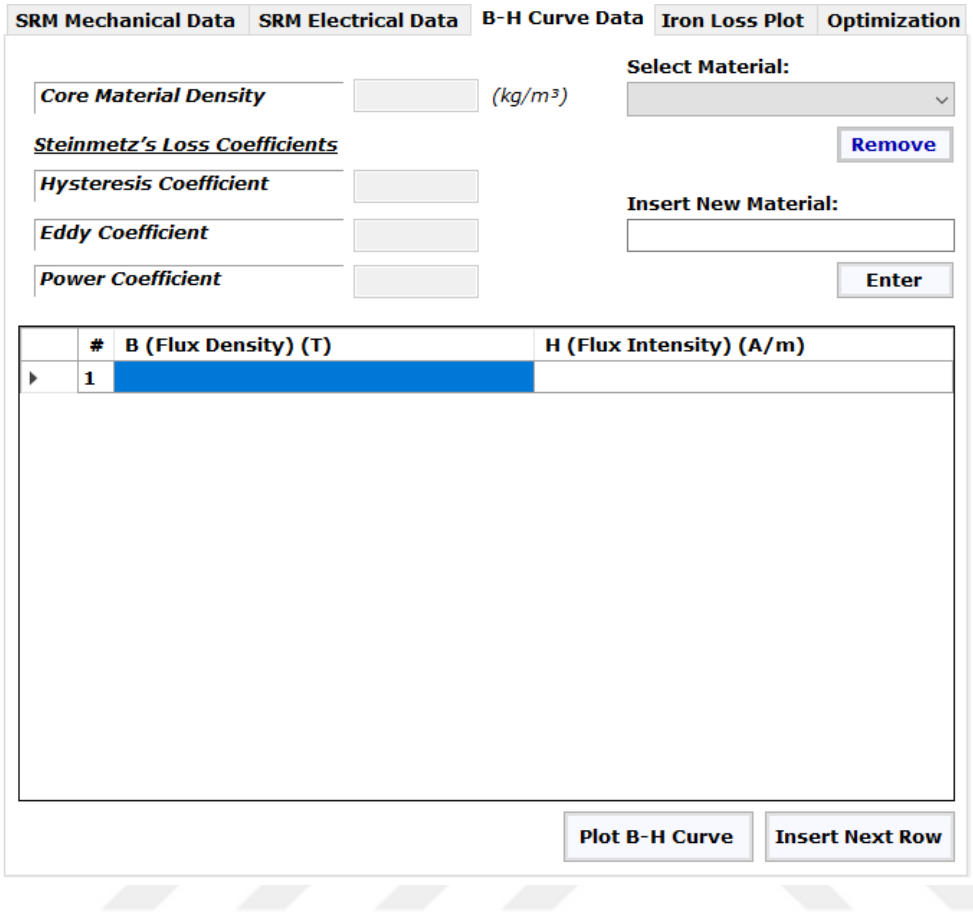

Figure 3.6. Tab 3 - Data entry interface for the B-H curve, material density and loss coefficients

The third tab shown in Figure 3.6 focuses on the data entry for material related properties of the SRM. First, the material name and information need to be entered. Afterwards, the core material density part, loss coefficients and the B-H data grid view are available for editing. The loss coefficients are found and put into place as described in Section 1.4.7. It must be noted that this tab is the common part necessary for both performance calculations and the optimization process. The program also checks for unmatching B-H curve data and if there are any, warns before saving or before calculating. If a duplicate data is entered, the user is also warned, and the duplication is corrected. The user can insert extra rows in between the B-H curve data if necessary. This part also allows the user to graphically view the B-H curve. The plotting interface of the program is made from scratch in order not to be dependent on any package with licensing issues and made to fit the specifications necessary for examining properly.

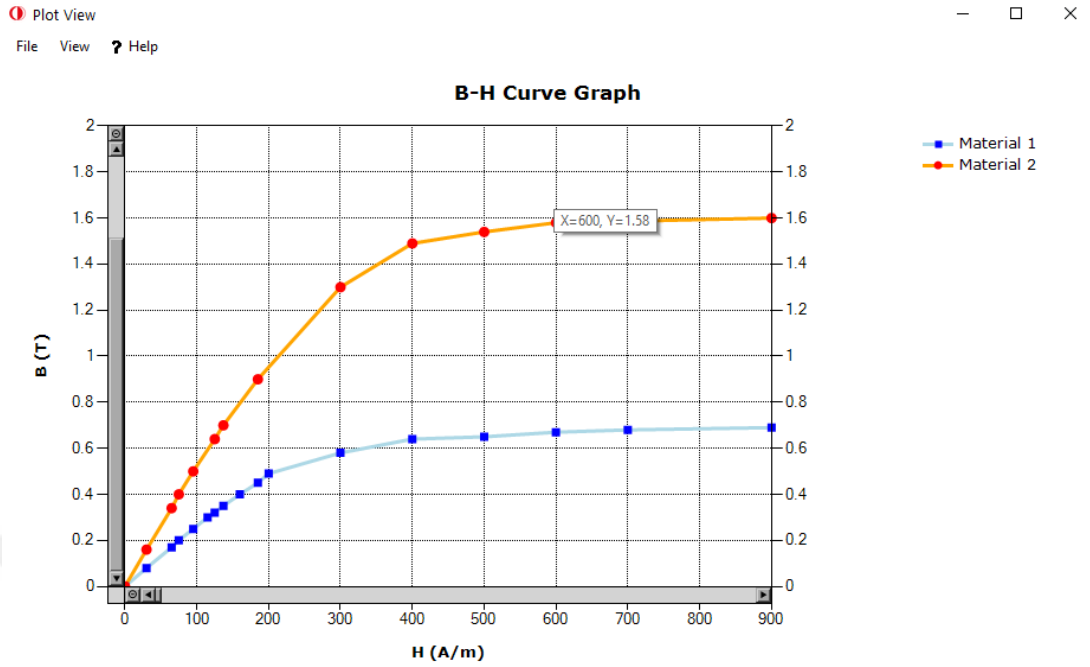

Figure 3.7. The B-H data plotting interface of the SRM performance analysis program

The plotting interface can be seen in Figure 3.7. Viewing B-H curve of more than one material is possible as shown. Hovering the mouse on the data gives the exact values of the entered datapoint. Zooming is possible through mouse wheel or by selecting the zoom area by a rectangle. The boundaries are automatically updated and the increasing steps on X and Y axis are automatically calculated.

The view tab offers many different plotting options. The user can decide to plot a single B-H curve as shown in Figure 3.8 or plot multiple curves as shown in Figure 3.7. Plot may display just entered points or may connect them in various ways. The user can also save the graph as a PNG or JPEG image file. Help option also informs the user on how the plotting and other options work. The user can auto-scale the graph using three options, auto-scaling X axis, Y axis or by auto-scaling both X and Y axis.

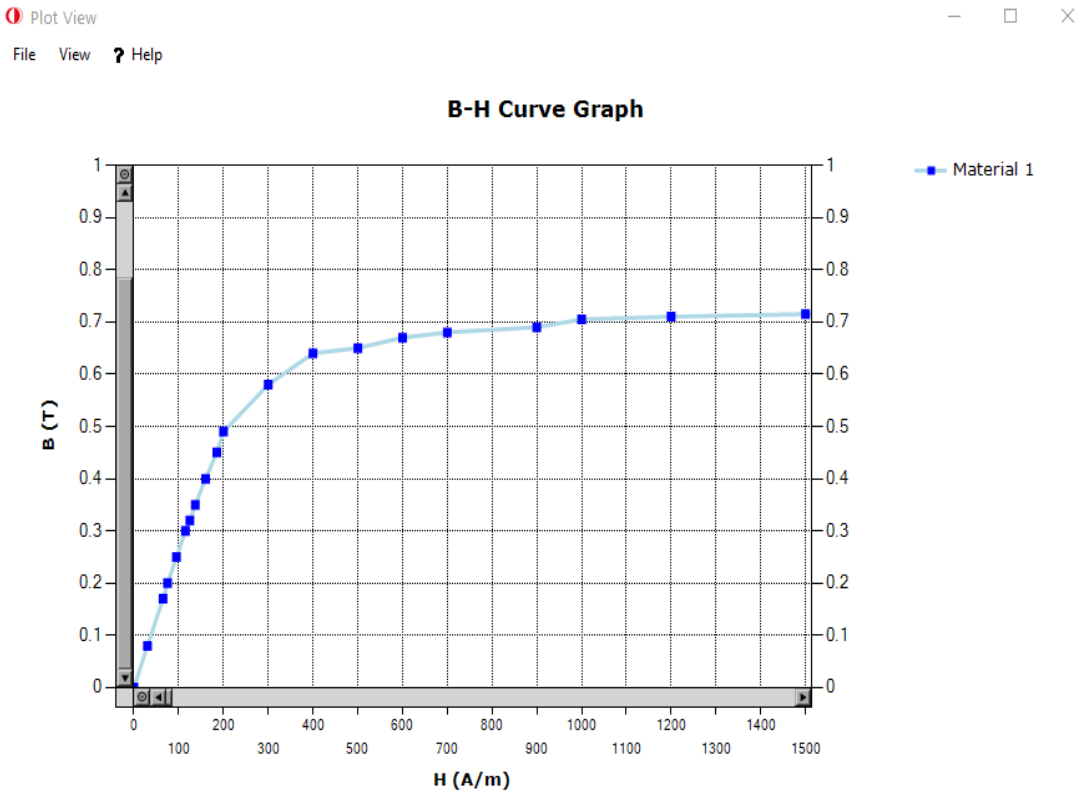

Figure 3.8. The B-H data plotting interface with plot option selected for a single material

The fourth tab shown in Figure 3.9 allows the user to enter iron loss data for each frequency and plot it to obtain a visual guide on how the loss varies. The current version of the program uses the entered information in the third tab for the calculations of the core losses. The MATLAB 'm' file used for analytical calculations and the user interface can be modified to use the data entered into the fourth tab, if available, instead of the core loss calculations through the usage of Steinmetz's equation.

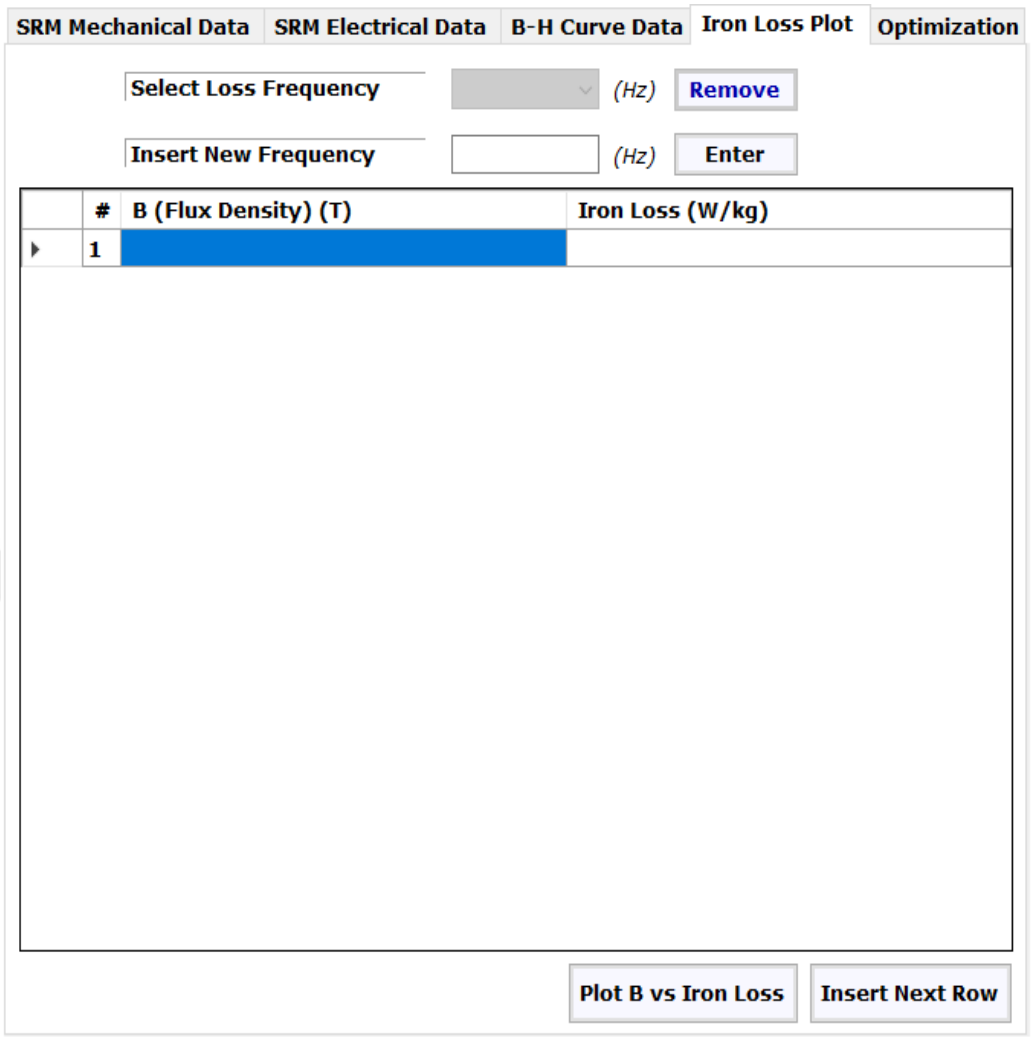

Figure 3.9. Tab 4 - Iron loss plotting interface of the SRM performance analysis program

3.3.2. Data input interface for simulating the results of the optimization process

As well as the analysis capability, the developed software has the capability to optimize a switched reluctance motor to meet given specifications.

The fifth tab, which is given in Figure 3.10, displays the user interface screen where the user can enter the necessary data for optimization process to simulate and obtain the results once the genetic algorithm results have been found. The optimization algorithm used in this part of the software is explained in Chapter 4.

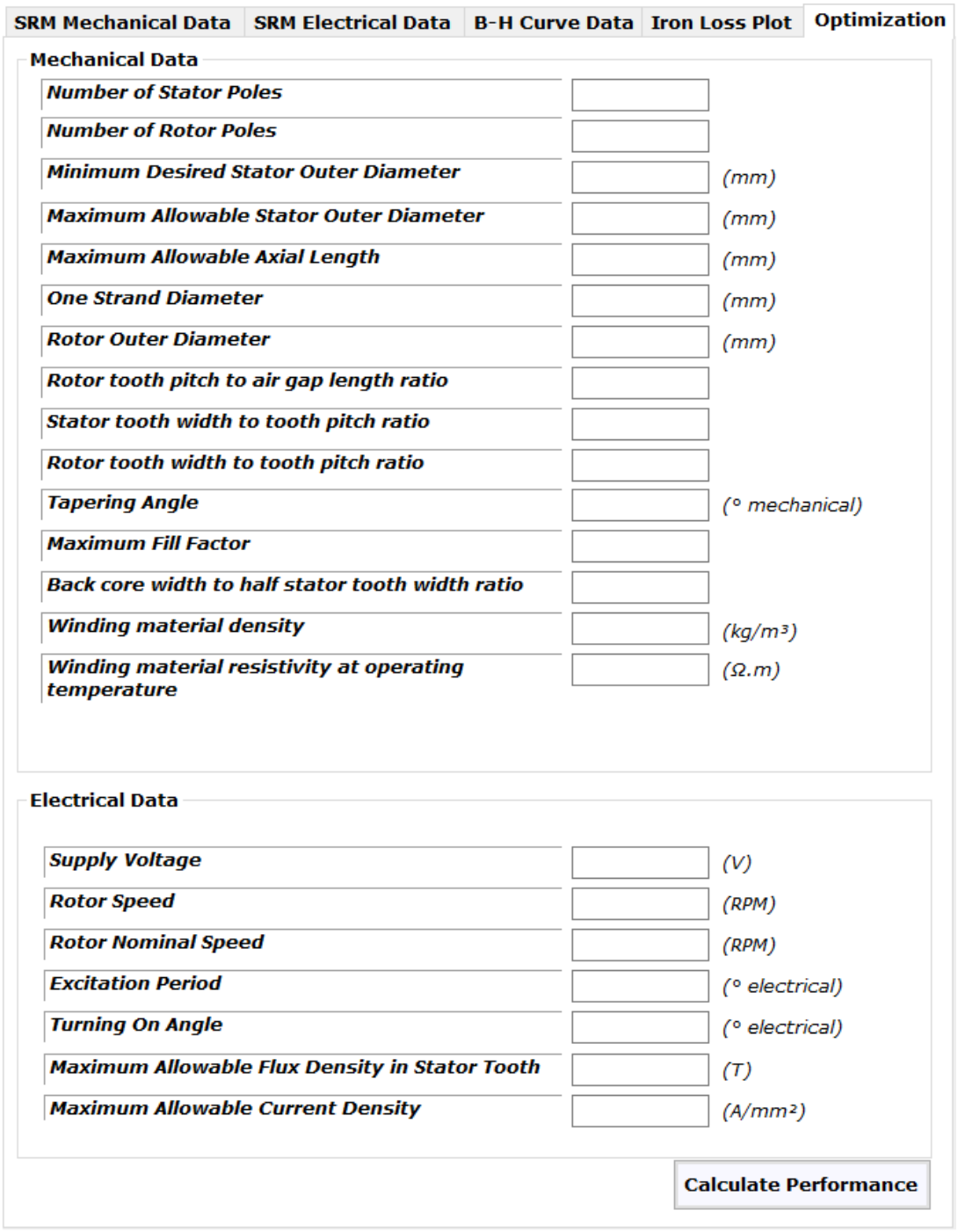

Figure 3.10. Tab 5 - Performance calculation interface of the SRM performance analysis program for optimization purposes

It should be noted that the genetic algorithm is not called from the designed interface as currently MATLAB focuses on updating and changing its optimization program. Thus, it is more feasible to open the ‘m’ file directly via MATLAB (with slight alterations to the code to fit the format required for the genetic algorithm optimization method through optimization toolbox) and use the optimization toolbox it has until the update in optimization software is brought by MathWorks [30]. Then, it can be implemented in this program.

MATLAB optimization toolbox interface [30] which is used for determination of the independent variables of the optimization are given in Figure 3.11 and Figure 3.12. The user should select genetic algorithm as the solver, enter the reference to the ‘m’ file, declare the number of independent variables of the optimization and set the upper and lower limits for the independent variables, as seen in Figure 3.11.

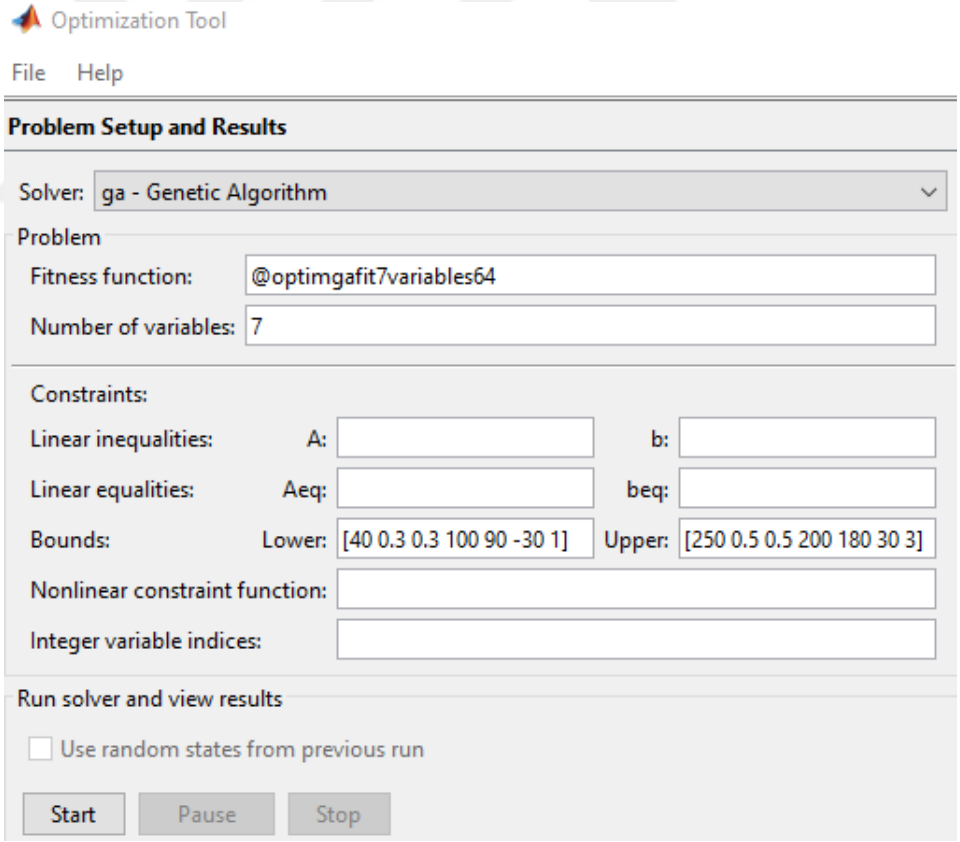

Figure 3.11. Entry of bounds, independent variables and function reference into the MATLAB optimization toolbox

The user should then specify how the genetic algorithm is to be implemented. Setting the number of generations, number of stall generations and function tolerance is an example to this, as can be seen in Figure 3.12, which is the case used in the optimizations covered in Chapter 4 of this research.

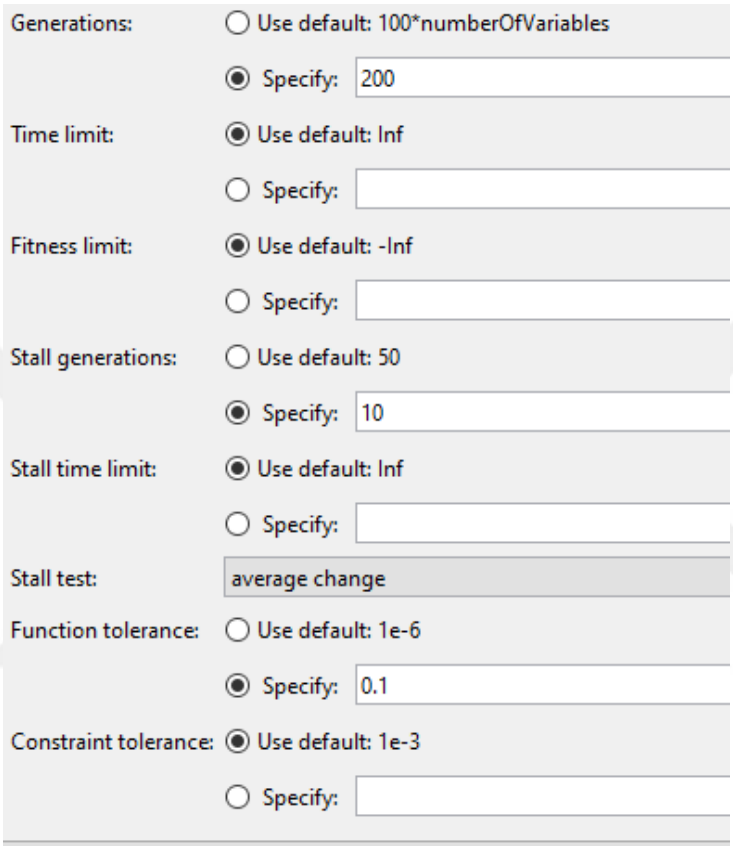

Figure 3.12. Determination of the operation of the genetic algorithm within MATLAB optimization toolbox

Once the ‘m’ file is changed to meet the specifications, and the necessary inputs are entered to the MATLAB optimization toolbox [30] as in Figure 3.11 and Figure 3.12 for the desired pole combination, optimization can be started. After computation, optimized values for the independent variables and the resultant value of the objective function are displayed in this interface. The user can then enter these independent variables into the fifth tab shown in Figure 3.10, as well as the other necessary inputs in the tab, in order to calculate the performance of the optimized SRM.

It should be noted that the third tab given in Figure 3.6 and the fifth tab given in Figure 3.10 should both be filled for the performance calculation of the optimization to take place. When the necessary data is filled, the user can press the performance calculation button for the calculations to take place. After the button is pressed, if there are any missing or problematic parts on the data input side, the user is directed to the point of error for corrections, after which calculation can be made.

3.3.3. Results, definitions, save and load procedures

This part is for describing the user interface functions on saving and loading processes, entering definitions and plotting and illustrations of the results.

The upper part of the interface shown in Figure 3.13 allows the user to set the data name, and optionally add the date when the data is to be saved. Adding the date automatically helps keep track of the data and information altering process. The user can optionally enter a description for the ongoing analysis for better understanding the project that is being worked on at that time. This is recommended and gives a great ease of use as there can be many projects that are simultaneously being worked on, thus helping the user know exactly what was aimed to be achieved with the data used.

Plotting and saving results part is only available after performance calculation of a specific SRM or performance calculation for optimization purposes have been done. Once the calculations are completed, the user can choose which dataset to be plotted, such as torque-position-current, flux linkage-current-position, phase current vs time or angle, instantaneous torque vs time graphs. Final results for the performance calculation are displayed on the bottom right part of the interface shown in Figure 3.13 and the user can easily see the results of the analysis. Performance calculation for optimization, after being calculated, also opens up a new window to show the design parameters necessary for the design of the SRM. These parameters are described in Chapter 4 of this research.

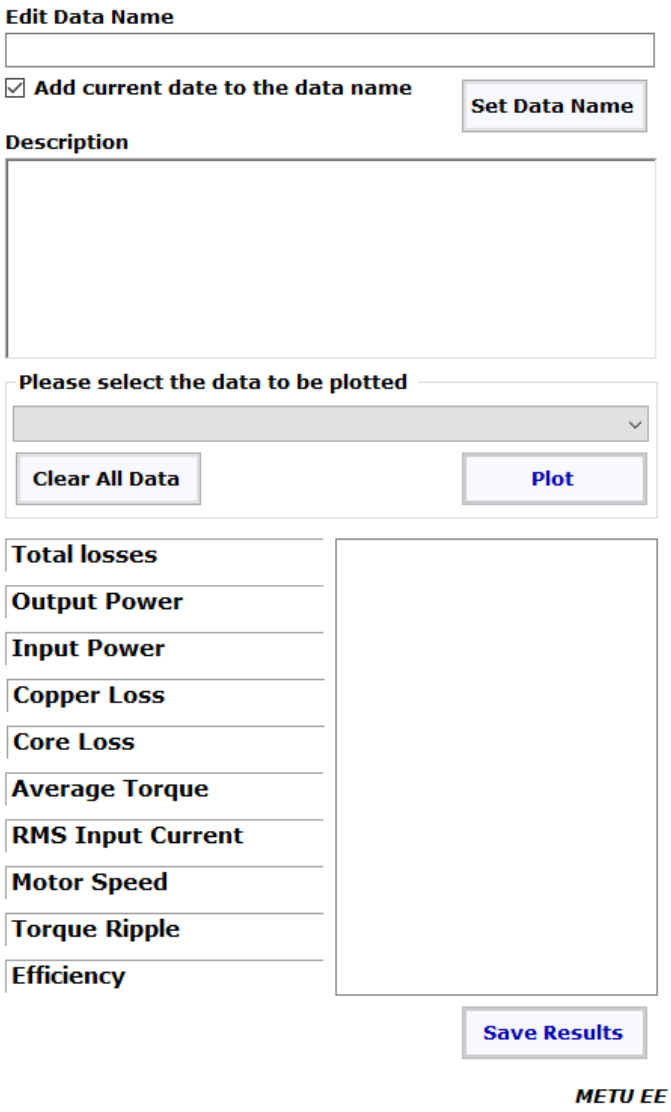

Figure 3.13. The result and info part of the SRM performance analysis program

The user can also choose to save the data at any time or load a previously saved data for analysis purpose. When saving, the entered data is checked for any missing inputs or errors and warns the user about detected errors. The data is saved as a text file, and although not recommended, the user can also alter it and add new data through the text file interface as well. Thus, for the loading process, there is a very strict control of the data in order not to load anything that has been altered into an incorrect format. Each step is checked for alterations and if any, necessary warnings are displayed to the user and only the correctly entered data is accepted.

Figure 3.11 shows an example of the warnings that can be encountered while saving. Figure 3.12 shows an exemplary text file created for the save process and how the save data is stored. Figure 3.13 shows some of the errors that can be encountered while loading a saved data.

These processes and precautions ensure that the calculations are done correctly. If the user desires, they can also clear all the data (which keeps the description and data name untouched while clearing the data entered into the described five tabs), clear everything or just open a new project.

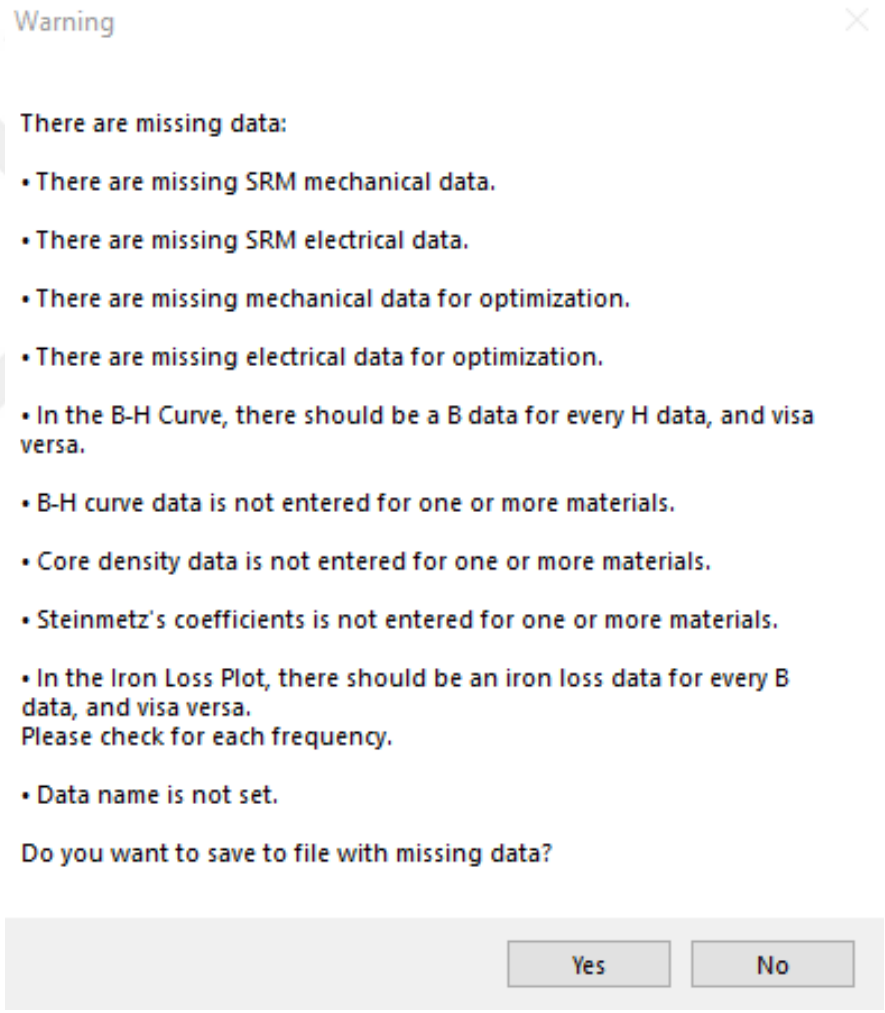

Figure 3.14. Save warnings of the SRM analysis program for the user

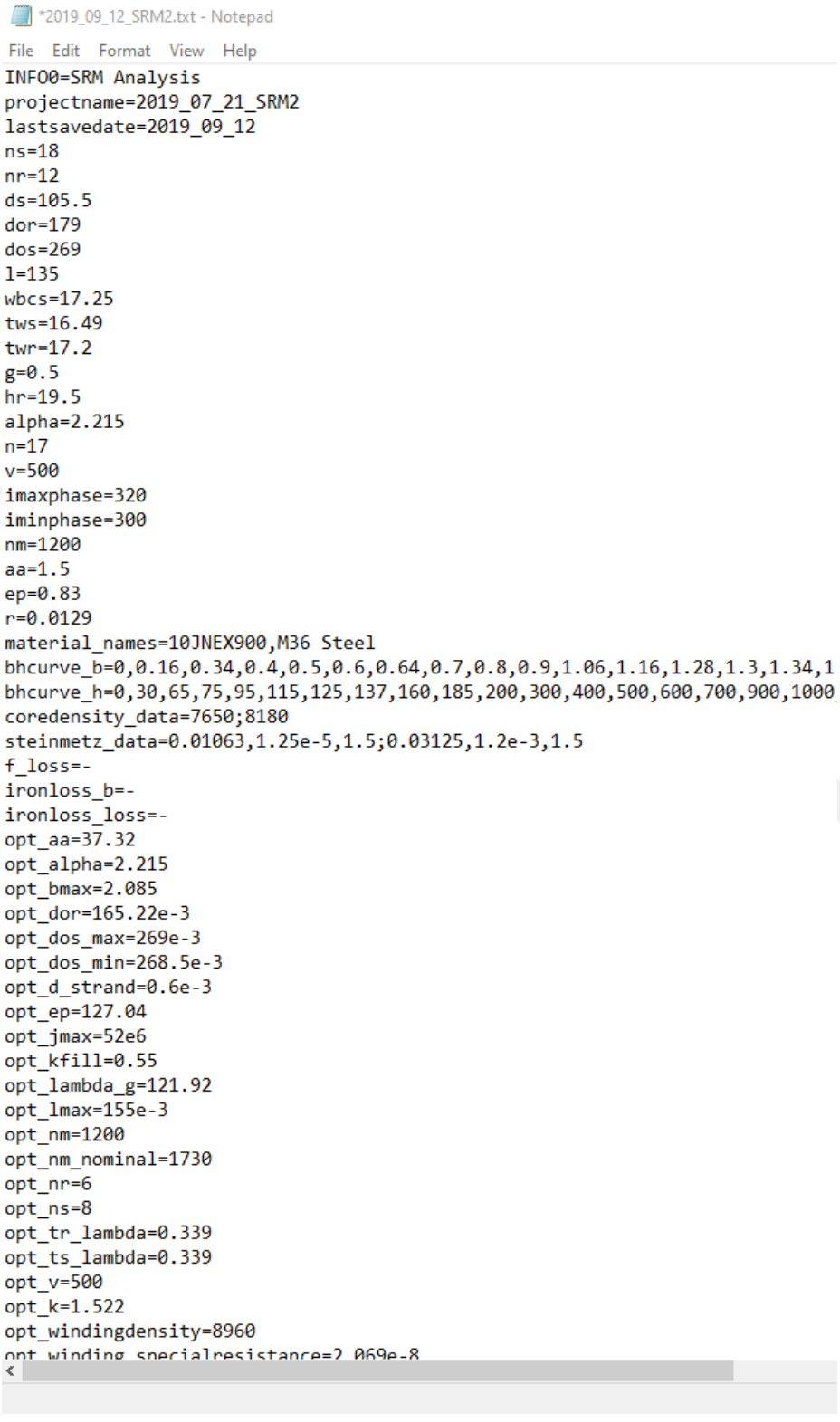

Figure 3.15. The text save file containing all the information stored in the SRM analysis project

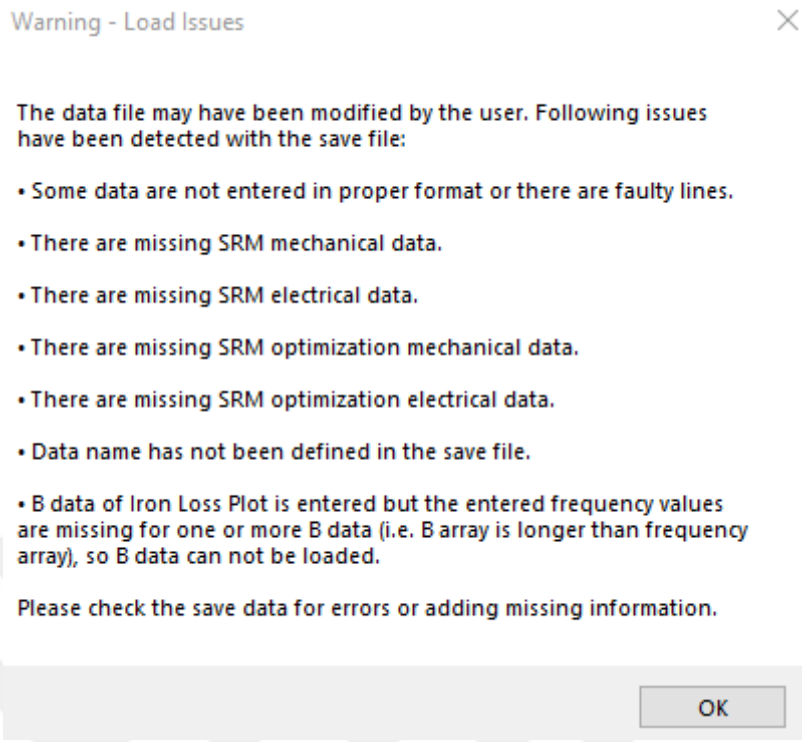

Figure 3.16. Example of warnings that may be encountered when a corrupted save file is being loaded

The user is also able to resize the data entry screen at will. This is an important but highly skipped part of developed programs. Especially the programs that have been previously created in METU Electrical and Electronics Engineering Department have been seen to lack this property. A false sizing causes the program to appear broken or not allow the user to enter the required data into the program. Enabling and properly setting the resizing property allows the user to work on different screens or multitasking with other programs.

CHAPTER 4

OPTIMIZATION PROCESS AND DETERMINATION OF OPTIMAL POLE COMBINATION FOR THE SRM

4.1. Aim of the chapter

This part focuses on attaining the optimal torque from a switched reluctance motor by testing different pole combinations and control values. Thus, the optimal pole combination for the offered switched reluctance motor specified can be found. The idea is to increase the torque while keeping the core length and outer diameter of the motor within specified constraints. Later on, the corrected results will be compared to the results given in [23].

4.2. Optimization procedure

For the optimization purpose, the objective function to be maximized is taken as the average torque of the motor at 1200 rpm. This average torque (T_{avg_1}) is calculated through integration of the steady state torque variation vs time (T(t)) of the SRM and dividing it with the conduction period for one phase (T_1).

$$T_{avg_1} = \frac{1}{T_1}\int_0^{T_1} T(t)dt \tag{4.1}$$

It should be noted that there are two penalty factors imposed on this average torque value calculations for the optimization, f_{p1} and f_{p2}, defined in Equation 4.21 and Equation 4.30. So, the augmented objective function of the optimization process becomes as defined Equation 4.2.

$$T_{avg} = \left(\frac{1}{T_1}\int_0^{T_1} T(t)dt\right) - f_{p1} - f_{p2} \tag{4.2}$$

There are eight independent variables of this optimization process. These are:

1- N_s/N_r, number of stator poles vs number of rotor poles
2- λ_r/g, rotor tooth pitch per air gap length ratio
3- t_s/λ_r, normalized stator tooth width
4- t_r/λ_r, normalized rotor tooth width
5- D_{or}, the outer diameter of the rotor
6- K, back core width to half of stator tooth width ratio
7- Conduction period (ep)
8- Phase turn on angle (θ_{on})

These values will be changed within a boundary in order to find the best combination for maximizing the average torque. Optimization is done similar to the method proposed in [23], with the changes made to the analysis algorithm as described in Chapter 2.

There are two constant parameters that will be taken the same for all the optimization procedure of this research. These are:

1- Motor speed, taken as 1200 rpm
2- DC supply voltage, taken as 500V

It is important to note that the motor to be optimized is aimed to give the same or better performance results as compared to SRM2. Thus, the desired output power is set to 50kW at 1200 rpm. After the optimization calculations for different pole pairs, the results will be observed to see if the case is met.

4.2.1. The genetic algorithm

The procedure to be applied is for the determination of the optimal pole combination and sizing of the switched reluctance motor to maximize the torque output. In order to do so, the most optimal operation point for each pole combination needs to be determined by changing the independent variables, and afterwards these results need to be compared.

The standard derivative approach is not a good procedure to be applied in this case as many local maximum and minimum values exists. Thus, genetic algorithm offered through MATLAB's optimization toolbox [30] has been selected to be used in the optimization process.

Genetic algorithm, as the name suggests, is an algorithm that derives its logical roots from nature's evolution theory. At every step, the algorithm uses randomly selected individual solutions to predict the next generation of values. The randomly selected values can be viewed as parents and the generation that follows as children. It should be noted that the children are created from the parts of the population where the fitness function (which is the augmented objective function defined in Equation 4.2 for this case) has higher values. This means that the independent variable values that lead to higher torque output calculations are selected and different combinations of these values produce the next population.

With each step the population evolves towards an optimal solution. These steps continue until a specified criterion is met. The criteria can be met by a maximum desired number of generations being achieved or through tolerance of the function, which means that the rate of change of the fitness function over stall generations (the generations where the rate of change in the fitness function starts decreasing) is below a certain specified range, i.e. lower than the tolerance of the function.

In this research the population is set to have 200 members in each generation. This means that the fitness function is calculated 200 times for each generation, which corresponds to 200 different combinations of the independent variables. These 200 will parent the next 200 switched reluctance motors until the necessities for stopping are met. These criteria are having 10 stall generations (which can be considered as the minimum number of generations that are created) and 0.1 for the function tolerance. The implementation is done via MATLAB's optimization toolbox [30] as can be seen in Figure 3.11 and Figure 3.12 and is explained in Section 3.3.2.

4.2.2. Steps of the optimization process

There are seven independent variables apart from the N_s/N_r value, described in Section 4.2.3. The boundaries for these are set as described in Section 4.2.3 and entered into the optimization toolbox as limits. Genetic algorithm uses these independent variables to generate the initial points of the optimization. This procedure is done for every N_s/N_r value separately. For each, a separate excitation pattern and an optimized geometry that gives the highest torque output will be determined. It is important to note that the genetic algorithm is actually a minimization algorithm. Thus, simply multiplying the resultant torque by -1 and minimizing that value results in the calculation of the maximum torque output value. The following steps are described below in order:

1- Through the boundaries set for the independent variables of the optimization, as can be seen in Figure 3.11, genetic algorithm creates the initial population.
2- The initial values generated by the genetic algorithm are used to calculate air gap length, stator and rotor tooth width, as described in Section 4.3.1.
3- Rotor and stator back-core widths are calculated, as in Section 4.3.3.
4- Motor shaft diameter and rotor pole height are calculated, as in Section 4.3.4.
5- Stator pole height, number of turns per pole, winding wire diameter, rated current, minimum and maximum value of chopping current and wire resistance are calculated, as explained in Section 4.4.5.
6- Torque-position-current and flux linkage-current-position data are calculated, as described in Section 1.4.5.
7- Torque vs time and current vs time are calculated, as in Section 1.4.6.
8- Active mass of the motor is calculated for torque per unit mass calculations.
9- Average torque is calculated as in Equation 4.2.
10- The next generation of data are created using these values. If the stopping criteria are met, the optimized results are used for design and performance calculations. The optimization is repeated for different N_s/N_r values.

It must be noted that in performance calculations, phases which produce positive torque are considered in calculation of instantaneous torque, and at appropriate times 2 phases of the SRM contribute to the torque output simultaneously.

4.2.3. Independent variables of the optimization

This part focuses on the independent variables of the optimization process. These parameters determine the change in the maximum torque of the switched reluctance motor. They introduce a change in motor size and operation, which will be examined. These independent parameters are given in the following subsections.

4.2.3.1. N_s/N_r value

The pole combinations of a switched reluctance motor have certain specific values that needs to be followed in design process. The driver control systems are made for some specific standardized values, which makes it advisable to follow the standards for ease of control. This value also specifies the number of phases of the switched reluctance motor and has a significant effect on the average torque. Number of phases can be found using the formula given below:

$$q = \frac{N_s}{GCD(N_s, N_r)} \tag{4.3}$$

In Equation 4.3, GCD is the greatest common denominator, q is the number of phases and N_s and N_r stand for the number of stator and rotor poles, respectively. Standardized values for the pole combinations are given in the Table 4.1.

Table 4.1. *Switched reluctance motor common number of poles and corresponding number of phases*

N_s / N_r	6/4	8/6	12/8	18/12	24/18	32/24
q (number of phases)	3	4	3	3	4	4

The given number of poles in Table 4.1 will each be tested out for finding the optimal pole combination of the switched reluctance motor. It should be noted that the 32/24 switched reluctance motor has not been tested out in [23] but will be tested in this research.

4.2.3.2. λ/g value

This value is for identifying the air gap length of the switched reluctance motor depending on the tooth pitch of the rotor. The tooth pitch is found using the following Equation 4.4.

$$\lambda_r = \frac{\pi D_{or}}{N_r} \tag{4.4}$$

In Equation 4.4, D_{or} represents the outer diameter of the rotor, λ_r is the tooth pitch of the rotor and N_r is the number of poles of the rotor. In this research a generic switched reluctance motor with normalized (dimensionless) variables is considered. Thus, all parameters need to be independent from dimensions, including bore diameter and motor length. This is a main reason why the normalized value of λ_r/g is chosen as an independent variable for the optimization process. The tooth pitch of the rotor and the air gap can be found for the specific SRM once the D_{or} is known.

Previous researches done on the subject have shown that the value of λ/g changes between 40 and 250. This is the procedure to be followed in this research as well.

4.2.3.3. t_s/λ value

The value of t_s/λ is used to show the normalized value of stator tooth width of a switched reluctance motor. This value is, as previously mentioned in description of the second independent variable, is to remove the effect of dimensions in the calculation process and easily determine the corresponding normalized dimensions. Later on, the tooth width of the switched reluctance motor is found by using the rotor tooth pitch and bore diameter of the motor.

In [23] this value is changed between 0.3 and 0.5, thus is to be done in this research as well.

4.2.3.4. t_r/λ value

The value stands for the normalized tooth width of the switched reluctance motor's rotor. Again, a normalization is necessarily used for the ease of dimensionless calculation. The rotor tooth width value can be calculated through the knowledge of bore length, air gap length and knowing the number of phases. The calculations are given in Section 4.3.

In this research, for optimization purposes, the value is changed between 0.3 and 0.5 as has been done in [23].

4.2.3.5. D_{or} value

As the outer diameter of the stator has a determined maximum length for this research, which corresponds to 269mm, the rotor outer diameter value is varied between 100mm and 200mm for being able to work on the sustainable and feasible values of D_{or} value. If this value is selected to be too small, the average output torque will be low and slot area will be affected, introducing a decrease in the fill factor. Also, the shaft diameter needs to be able to bear the load, so rotor outer diameter should not be too small. If it is selected larger than a certain amount, this would result in small winding area and consequently lower of a value for the electrical loading.

4.2.3.6. K value

This value represents the back-core width to half of stator tooth width ratio. This value plays an essential role in the torque production of SRM and saturation. A small value would be resulting in an early saturation region being achieved. A high value would indicate that, as this would increase greatly the motor weight, a loss in torque density would be encountered. For this research, stator and rotor back-core widths are taken to be equal. Equation 4.5 shows calculation of K value as described.

$$K = \frac{W_{bcs}}{t_s/2} = \frac{W_{bcr}}{t_s/2} \quad (1 < K < 3) \tag{4.5}$$

The following Figure 4.1 shows the back- core widths for stator and rotor for in order to supply a better understanding of the variables in a visual manner.

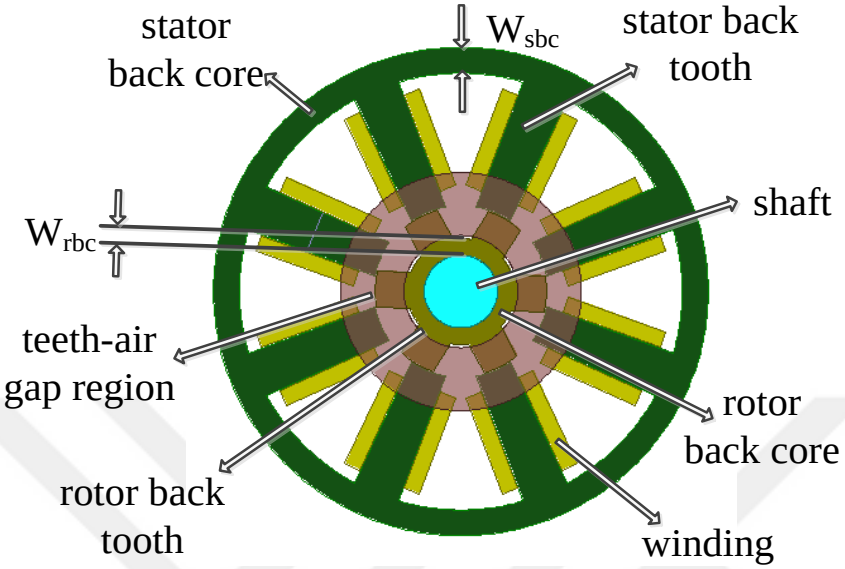

Figure 4.1. Dimensional parameters of an 8/6 SRM

4.2.3.7. Conduction period

The conduction period, which is defined in Section 2.3.3.4, has a very important role on the resultant operation of the motor. This value is altered from 90 degrees electrical to 180 degrees electrical. This affects the excitation duration of the pole pairs and thus the phase current. If the conduction duration is lower than 90 degrees, this would result in the input current not being continuous. Thus, there would be a non-excited duration until the next phase is turned on, decreasing the average output torque and causing pulsations on the rotor. If the value is selected too high however, which is larger than 180 electrical degrees, this would introduce a negative torque on the system, also having a negative effect on the rotation, causing the rotor to vibrate.

So, adjusting the appropriate conduction period plays a significant role in both the control and optimization of the motor.

4.2.3.8. Phase turn on angle

Phase turn on angle, defined in Section 2.3.3.4, also plays an important role in the control and outcome behavior of the switched reluctance motor. This property, along with the duration of conduction determines the excitation behavior of an SRM. As an example, a four phase 24/18 motor has a firing range between -45 to 45 degrees electrical. Choosing this value correctly is very important in order not to produce negative torque and let the current have enough time to rise. The excitation pattern should coincide with the rising inductance region for a motoring operation. The firing can also be done to coincide the excitation with the falling inductance region, but this would result in the machine working as a generator. Covering the firing region and changing the conduction period is thus very crucial in finding the optimal values for the optimization of the SRM.

4.2.4. Constraints for the optimization process

This part will be focusing on the constraints that bind the optimization process. Specifying these parameters correctly is necessary to attain a feasible result for the switched reluctance motor design. There are 7 constraints for this design procedure.

4.2.4.1. D_{os} value

D_{os} is the stator outer diameter value. In order to make understandable comparisons with previous research [23], the value set previously on the outer diameter of the stator will be taken, which corresponds to 269mm. This sets the maximum value of the stator outer diameter for the optimization, and the result will be less or equal to this value.

4.2.4.2. B_t value

This is the tooth flux density value. Previous finite element simulations in [23] show a maximum value of 2T reached for the proposed model, so the limit will be set to be equal or less than 2T. From the usage of tooth geometry as well, this will help determine the flux and flux linkage values.

4.2.4.3. Current density value

The maximum value of the current that passes through the windings of the stator is determined by the current density, which is also dependent on the cooling method. In this study, the previously observed limit on 18/12 SRM will be used [23], which is identified to be 33A/mm^2. It is important to note that this value is only reached at the presence of a liquid cooling system. The calculation is given in the following Equation 4.6, in which J_{rms} stands for the rms current density, I_{rms} stands for the rms current and A is the area through which current passes. It is important to note that stranded winding structure is used and diameter of one strand is chosen as 0.6mm.

$$J_{rms} = \frac{I_{rms}}{A} \leq 33A/mm^2 \tag{4.6}$$

4.2.4.4. Excitation pattern

Excitation pattern includes the turn on angle and conduction period. The focus will be on 3 and 4 phase SRMs, as they are the ones covered in this research. A four phase SRM has a minimum of -45 electrical degrees firing angle (θ_{on}) before producing a negative torque, unless being operated under very high speeds, in which firing can be set to occur even before to allow the current enough time to rise. This value is -30 electrical degrees for three-phase SRMs. Including the fact that the conduction period (ep) can be a maximum 180 electrical degrees before causing a negative torque production, which in other words brings the requirement of turning off the phase before reaching the fully aligned position, there is a constraint that is brought upon the sum of firing angle and conduction period. The limitations can be observed in the Equation 4.7 and Equation 4.8, being less or equal than 135 degrees electrical for a 4 phase SRM and 150 degrees electrical for a three phase SRM.

$$\theta_{on} \geq -45° \ (q = 4) \ \& \ \theta_{on} \geq -30° \ (q = 3) \tag{4.7}$$

$$\theta_{on} + ep \leq 135° \ (q = 4) \ \& \ \theta_{on} + ep \leq 150° \ (q = 3) \tag{4.8}$$

Figure 2.15 can be referred for a visual understanding on the limits. This figure shows the firing angle and torque production of an 8/6 4 phase SRM. It can be clearly seen that firing before -45 degrees electrical will lead to a negative torque production. If fired at -45 degrees electrical, positive torque can be produced for maximum 180 degrees electrical, and any further excitation will lead to introduction of negative torque values. Thus, the reasoning behind Equation 4.8 can clearly be seen.

4.2.4.5. Slot fill factor

Slot fill factor (k_f) is the quantity that defines the volume taken up by windings in the slot area. The definition is given in Equation 4.9, where A stands for area.

$$k_f = \frac{A_{winding}}{A_{slot}} \tag{4.9}$$

The winding and slot area of an 18/12 SRM can be observed in the Figure 4.2.

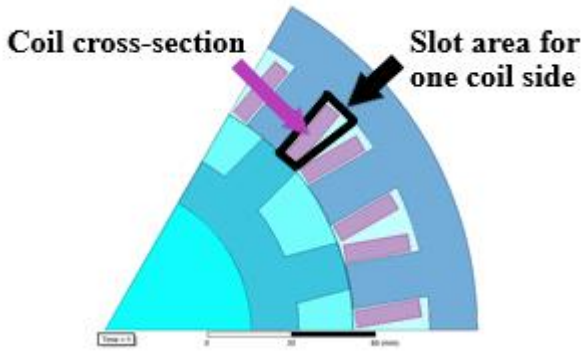

Figure 4.2. Winding and slot area of an 18/12 SRM

In the 18/12 SRM2 used for the calculations in this research, the fill factor value is 0.57. In the simulations, thus, upper boundary is to be set to 0.55. Winding area and the insulation method used for the slot are two important factors on this value.

Figure 4.3. Stranded conductor structure

In this research, in order to make better use of the windings, stranded windings are used, as can be seen in Figure 4.3. This affects the fill factor and the slot area, introducing a stranding factor. Thus, for fill factor calculations, a factor of 1.3 has to be considered. A single winding with a certain conduction area holds less space than a stranded winding with the same total conduction area. This is due to the cylindrical shape of the stranded windings, when stacked on top of each other introducing gaps in between. Area slice of a single strand occupies the area of a square, while filling area of a circle. Stranding factor of 1.3 is the proportion of areas of a square to a circle, in which one side of the square holds the same length as the diameter of the circle.

$$k_f \leq \frac{0.55}{1.3} = 0.42 \tag{4.10}$$

4.2.4.6. Shaft diameter value

The shaft diameter (D_s) should be large enough to support the stress brought upon by the load and torque. In SRM2, this value is 105.5mm. Thus, the value will be taken equal or higher than 105.5mm in order to overcome load related problems.

$$D_s \geq 105.5\ mm \tag{4.11}$$

4.2.4.7. Operating temperature

The heat and cooling method of the motor highly affects the copper loss values. It is an important point to be taken into account. This research, in addition to [23], allows calculation of resistance using resistivity of the winding material at desired temperature. The calculations are made in Equation 4.28, considering copper resistivity at 80°C, which is $2.069 \times 10^{-8}\ \Omega.m$.

It should be noted that this research does not include a thermal analysis of the SRM, which is an important factor as both the core and copper losses generate heat. The thermal analysis should be focused on for future research in this area.

In the following, summary of the given constraints can be seen.

1- $D_{os} \leq 269mm$
2- $Bt \leq 2T$
3- $J_{rms} \leq 33A/mm^2$
4- $\theta_{on} \geq -45°$ electrical for 4 phase SRMs and $\theta_{on} \geq -30°$ electrical for 3 phase SRMs.
5- $\theta_{on} + ep \leq 135°$ electrical for 4 phase SRMs and $\theta_{on} + ep \leq 150°$ electrical for 3 phase SRMs.
6- $k_f \leq 0.42$
7- $D_s \geq 105.5$ mm
8- Resistances calculated at 80°C, with a copper resistivity of $2.069x10^{-8}\ \Omega.m$.

4.3. The design procedure used in optimization

Determination of the motor dimensional parameters are necessary to find the performance of the switched reluctance motor. There are two dimensions initially specified for this case, which are the motor length including end windings which is 155mm, and the stator outer diameter which is 269mm. The calculation of the design parameters is to be discussed under this title. In this design the following parameters will be taken the same for all designed motors.

Table 4.2. *Constant parameters of the design process*

Stator outer diameter	269mm
Axial length	155mm
Stator tooth tapering angle	2.215 degree
One strand diameter	0.6mm
Simulation temperature	80°C

In the calculations of the genetic algorithm, pole combination stays constant while the other 7 independent values defined in Section 4.2.3 are changed. It must be noted that the optimization is done separately for each pole combination given in Table 4.1. In each generation, 200 SRM performances are to be calculated. In each performance calculation, independent variables have a different value. Thus, in order to calculate the performances, the calculation of SRM dimensions from these independent values is necessary. In the following, calculations of these parameters are given.

4.3.1. Tooth width values and the length of the air gap

These variables which correspond to rotor tooth pitch over air gap length, stator tooth width over rotor tooth pitch, rotor tooth width over rotor tooth pitch and the rotor outer diameter value are the dimensional independent variables of the optimization process. First, the rotor tooth pitch is calculated using the following formula.

$$\lambda_r = \frac{\pi D_{or}}{N_r} \tag{4.12}$$

In which N_r stands for the number of rotor poles, D_{or} for the rotor outer diameter and λ_r for the rotor tooth pitch. Once the rotor tooth pitch is determined, the tooth widths of stator (t_s) rotor (t_r) and the length of the air gap (g) can be found. Below the calculations for these parameters are shown.

$$t_s = \lambda_r \times (t_s/\lambda_r) \tag{4.13}$$

$$t_r = \lambda_r \times (t_r/\lambda_r) \tag{4.14}$$

$$g = \frac{\lambda_r}{(\lambda_r/g)} \tag{4.15}$$

4.3.2. The motor stack length

For calculations of the motor stack length (L), the thickness introduced by the end windings need to be considered. The width introduced by them are taken to be half of the stator sloth width (W_{slot}) in this research. The calculation is done using the following formula:

$$L = L_{total} - 2 \times \left(\frac{W_{slot}}{2}\right) - 0.002 \tag{4.16}$$

The 0.002 value corresponds to the one-millimeter safety margin from both sides of the motor.

4.3.3. Stator and rotor back core widths

These are two important variables for the magnetic characteristics and sturdiness of the motor. The stator back core width needs to be sufficiently dimensioned to avoid going into saturation. On the other hand, there is a maximum outer diameter constraint of the motor and this value of 269mm must not be exceeded. The stator back core width is selected to be greater than half of the stator pole width, as the flux that pass through the stator pole is two times that of the flux in the stator back core.

$$W_{bcs} = K \times \frac{t_s}{2} \qquad (1 < K < 3) \tag{4.17}$$

In this equation, K is an independent variable and is selected through a manner in which it will maximize the average output torque.

The rotor back core width should also be selected similarly to avoid saturation and the physical sturdiness needs to be enough to support the load. As the passing flux value in the rotor is the same as the flux passing the stator, the width is selected to be equal to the stator back-core width.

$$W_{bcr} = K \times \frac{t_s}{2} \qquad (1 < K < 3) \tag{4.18}$$

4.3.4. The pole height of the rotor and the shaft diameter

The rotor pole height contributes to few different effects. If it is selected large, the developed torque increases as the torque increases with the bore diameter for the same MMF value, and the inductance ratio between aligned and unaligned positions becomes high. However, there is a constraint on the maximum motor outer diameter. In the other perspective, a smaller rotor pole height allows a larger space for the stator windings. For the selection of the optimum rotor pole height value, an independent coefficient (k_{hr}) can be selected and changed between desired values, multiplied with air gap length and assigned to the rotor pole height (h_r).

$$h_r = k_{hr}.g \tag{4.19}$$

One important thing to note is that for calculation of the normalized parameters, the pole heights of the stator and rotor have been takes as forty times the length of the air gap. Thus, for the integrity of calculations, in this optimization process the multiplier in calculations is taken as forty.

The motor shaft diameter is also calculated after the determination of the rotor pole height as:

$$D_s = D_{or} - 2(h_r + W_{bcr}) \tag{4.20}$$

There is a penalty factor imposed upon the calculations for satisfying the constraint on the minimum shaft diameter. If air gap length is large and the shaft diameter becomes less than one fifth of the rotor outer diameter, this penalty factor is subtracted from the objective function which is the average torque, as be seen in Equation 4.2. For optimization, the torque is to be maximized and this penalty on the torque removes the undesired combinations from being selected. The penalty factor (f_{p1}) is defined as below:

$$f_{p1} = 100(e^{1-\frac{0.2D_{or}}{D_s}} - 1) \tag{4.21}$$

It should be noted that f_{p1} value changes between 0 and 100, and is subtracted from the objective function, which is the average torque value. The penalty factor is defined through experimental results of [23].

4.3.5. The stator windings, stator pole height and chopping current

The selection of the height of the pole is important for suppling the proper winding area. If the height is not sufficient enough, the loading will have to be set to a lower value than desired, leading to loss in average torque. It is also an important factor on the slot fill factor. For calculation of the pole heights, first we need to calculate the number of turns per pole. For this purpose, initially the maximum flux linkage of a phase winding (FL_{max}) is calculated. This is done by Equation 4.22 [25].

$$FL_{max} = \frac{V_{dc}\Delta\theta}{\omega_{rated}} \tag{4.22}$$

In Equation 4.20, $\Delta\theta$ stands for the mechanical angle between consecutive phases, V_{dc} being the input supply voltage and ω_{rated} being the rated angular speed. $\Delta\theta$ in the Equation 4.20 is defined as in Equation 4.23 [25].

$$\Delta\theta = \frac{2\pi}{qN_r} \tag{4.23}$$

In Equation 4.21, q stands for the number of phases and N_r being number of rotor poles. In the calculation of maximum flux linkage in Equation 4.22, the induction law has been used. A second way to express this is:

$$FL_{max} = 2\left(\frac{N_s}{2q}N_{pole}\right)\varphi_{max} = \frac{N_s}{q}N_{pole}B_{st_{max}}Lt_s \tag{4.24}$$

In Equation 4.24, N_{pole} is the number of turns per pole, L is the stack length, t_s is the stator tooth width, $B_{st_{max}}$ stands for the peak of the maximum allowable flux density in the stator tooth, and $N_s/2q$ stands for the number of pole pairs that are in conduction at the same time for one phase. This value is 1 for 6/4 and 8/6 SRMs, 2 for 12/8 SRM, 3 for 18/12 and 24/18 SRMs and 4 for 32/24 SRM.

Using the two formulas provided for the calculation of maximum flux linkage, which are given in Equation 4.23 and Equation 4.24, the number of turns per pole can be driven as:

$$N_{pole} = \frac{V_{dc}\Delta\theta}{2\frac{N_s}{2q}B_{st_{max}}Lt_s\omega_{rated}} \tag{4.25}$$

This optimization process changes the stator pole height between 40g and 250g values. In every step, slot area, stator outer diameter and pole height is calculated. The required slot area is also calculated taking into account the rms value of the maximum allowable stator current (I_{max}), which is calculated as:

$$I_{max} = \frac{MMF_{max}}{2N_{pole}} \tag{4.26}$$

In Equation 4.26, MMF_{max} is the maximum value of the MMF drop calculated at aligned position with the methods described in Section 1.4.3, and N_{pole} is the number of turns per pole. It is important to note that the value of the maximum allowable stator current is 33A/mm^2. This sets the limit for calculating area for one winding once the maximum current is known. The necessary slot area can also be found using the number of turns per phase once the area for one winding is known.

When the algorithm changes the stator pole height between calculations for 40g and 250g, in every step the pole length is increased by one air gap length. If the required value becomes smaller than the slot area at one point, the algorithm stops. On the other hand, if the required area is not met after 250g, the maximum allowable current is decreased by one percent and the steps repeated.

As the maximum allowable current is set, the chopping currents can be calculated. The maximum value of the chopping current is set to the maximum allowable current, and the minimum value of the chopping current is set to 0.92 times of that of the maximum allowable current.

It should be noted that the maximum value of the flux density and current density are not exceeded in this design method, thus a penalty factor is not introduced for them.

The method used for stator pole height calculations can be seen in the flowchart given in Figure 4.4.

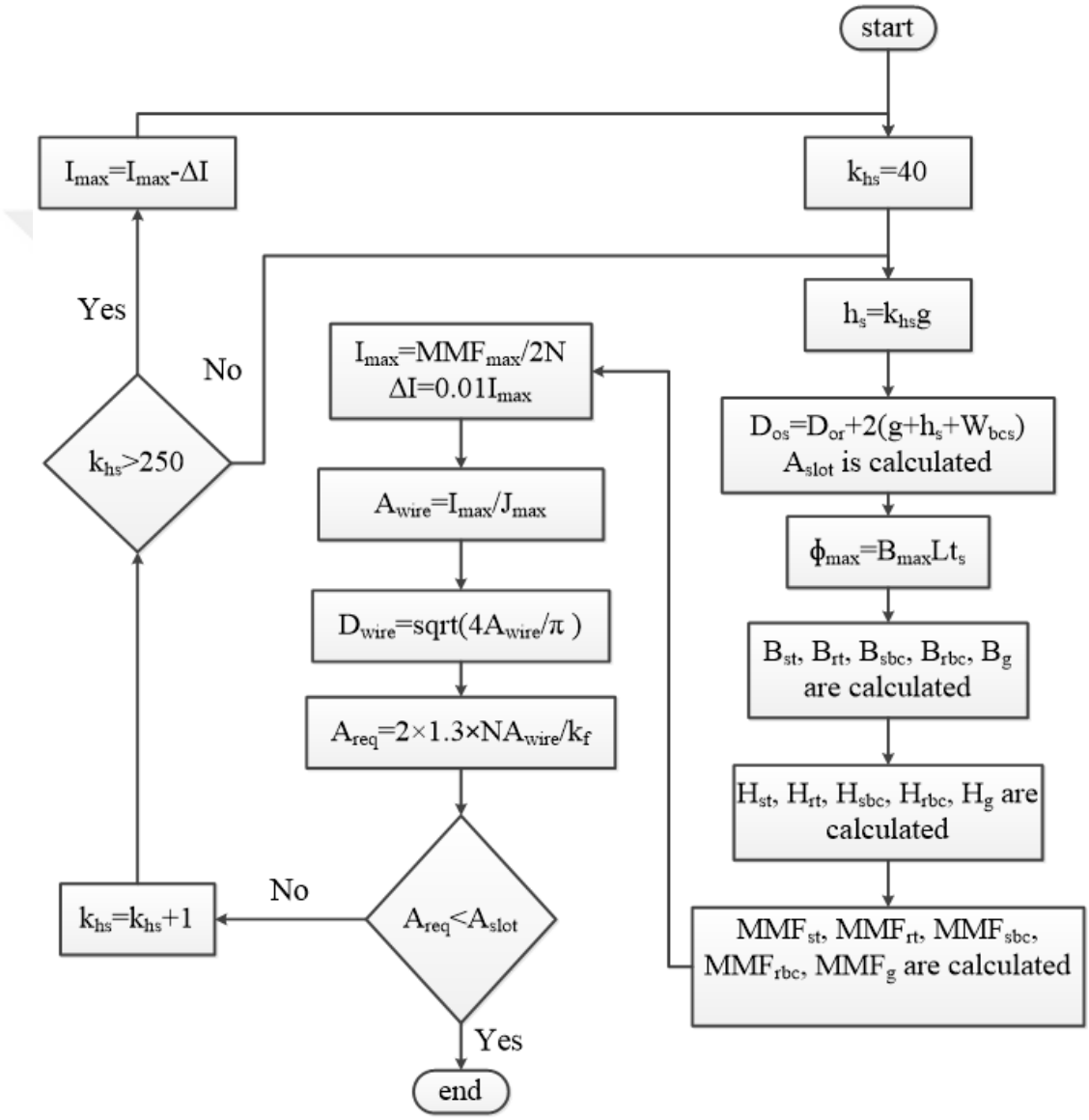

Figure 4.4. Flowchart for stator pole height calculations

4.3.6. Winding resistance

This calculation is necessary in order to compute the copper losses. For this purpose, the length of the copper windings (l_w) is calculated. For one pole pair, this corresponds to:

$$l_w = 2 \times (L + t_{s_{mean}} + 2 \times (\frac{W_{slot}}{2})) \times 2N_{pole} \quad (4.27)$$

In Equation 4.27, $t_{s_{mean}}$ stands for the mean length of the stator's tooth, N_{pole} for number of turns per pole and W_{slot} for slot width of stator. It is important to note that in this calculation, the width introduced by the end windings is considered, which corresponds to half of the stator's tooth width. The dimensions can be seen in Figure 4.5.

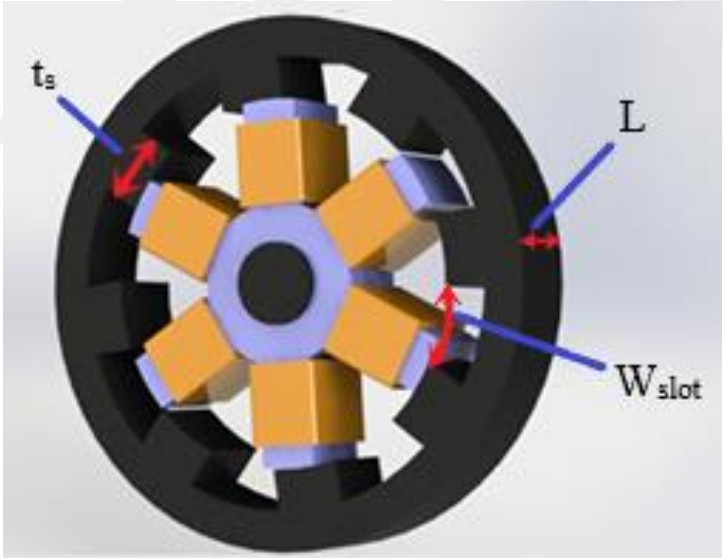

Figure 4.5. Slot width and winding of an 8/6 SRM

Once the length of the copper wire is known, the resistance (R) is simply calculated as:

$$R = \rho \frac{l_w}{A_{wire}} \tag{4.28}$$

In Equation 4.28, ρ represents the resistivity of the wire.

4.3.7. Stator outer diameter

The stator outer diameter has a constraint of 269mm, and the calculation for this dimension is done by the following formula given in Equation 4.29.

$$D_{os} = D_{or} + 2(g + h_s + W_{bcs}) \tag{4.29}$$

In Equation 4.29, D_{os} is the stator outer diameter value, D_{or} is the rotor outer diameter value, h_s is the stator pole height, W_{bcs} is the width of the stator back-core region and g is the air gap length. For a visual of these dimensions, Figure 4.1 can be referred.

If the outer diameter is to exceed the maximum desired value ($D_{os_{\max}}$), a penalty factor (f_{p2}) is introduced and taken into accounts as given in Equation 4.2. This subtraction leads to a lower torque value and thus optimization process disregards the values that are out of selection range. This penalty is defined as below:

$$f_{p2} = 2500(1 - e^{1-\frac{D_{os}}{D_{osmax}}}) \tag{4.30}$$

It should be noted that f_{p2} value changes between 0 and 2500, as given in Equation 4.30. The penalty factor is defined through experimental results of [23].

4.4. Checking the validity of the proposed design procedure

This part is for validating that the proposed design procedure works correctly. In order to do so, the design parameters for the SRM2 are calculated by the proposed method and compared with the dimensions and design of the actual SRM2 data. The obtained results vs the data at hand for SRM2 are given at the table below.

Table 4.3. *Comparison of actual and calculated dimensions of SRM2*

Variables	Actual	Calculated	Error (%)
Rotor outer diameter	179mm	179mm	0
Stator outer diameter	269mm	269mm	0
Core length	135mm	138mm	2.2
Axial length	155mm	155mm	0
Stator back core width	17.25mm	17.2mm	0.29
Shaft diameter	105.5mm	104.5mm	0.95
Air gap length	0.5mm	0.5mm	0
Rotor back core width	17.25mm	17.2mm	0.29
Stator tooth width	16.49mm	16.5mm	0.06
Rotor tooth width	17.2mm	17.2mm	0
Stator pole depth	27.25mm	27mm	0.92
Rotor pole depth	19.5mm	20mm	2.56
Number of turns per pole	17	17	0

As can be seen from Table 4.3, the calculated results are in very good agreement with actual values. This ensures that the design procedure is done correctly.

4.5. Performance results for one step of the optimization process

The objective here is to simulate a step of optimization and compare it with the results already at hand. Matching data will mean that the optimization process has been implemented correctly.

In order to compare, known values for SRM2 will be entered into the optimization code and simulated for one step, and obtained results discussed in Chapter 2 will be compared to the simulated results.

Table 4.4. *The independent variables of 18/12 SRM used for the comparison, taken as SRM2 values*

Variables	**Value**
N_s/N_r	18/12
λ/g	93.724
t_s/λ	0.352
t_r/λ	0.367
D_{or}	179mm
K	2.09
Excitation period	150 degrees electrical
Firing angle	-4 degrees electrical

Using the data shown at the Table 4.4, the results for this optimization step and comparison to the previous data are given below.

Table 4.5. *Comparison of SRM2 performance results with different calculation methods*

	Speed (rpm)	Average torque (N.m.)	Output power (kW)	RMS current (A)	Copper loss (kW)	Core loss (kW)	Total loss (kW)	Input power (kW)	Efficiency (%)
Analytical calculations - Tarvirdilu [23]	1200	406.6	51.1	190	12.23	1.044	13.274	64.37	79.4
FEM simulations - [23]	1200	364	45.74	191.3	12.42	1.255	13.675	59.42	77
Measurement results	1200	366	45.99	206	-	-	-	-	-
Analytical calculations - This research	1200	371.3	46.65	196.8	13.49	1.38	14.87	61.52	75.83
Optimization calculations - This research	1200	377	47.4	196.7	13.47	1.41	14.88	62.28	76.1
Optimization error vs measurement results (%)	-	3	3.07	4.5	-	-	-	-	-

As can be seen from Table 4.5, the results of the calculations of the optimization step are in good agreement with the previous simulations and closer to

the measurement as compared to the calculations done previously by [23]. This shows that the optimization process calculations are correct, and the optimization is trustable.

For a better inspection of the results, more correlations will be given. Below are the flux linkage-current-position graph, torque-position-current graph, phase current vs time graph and torque vs time graph for this optimization step.

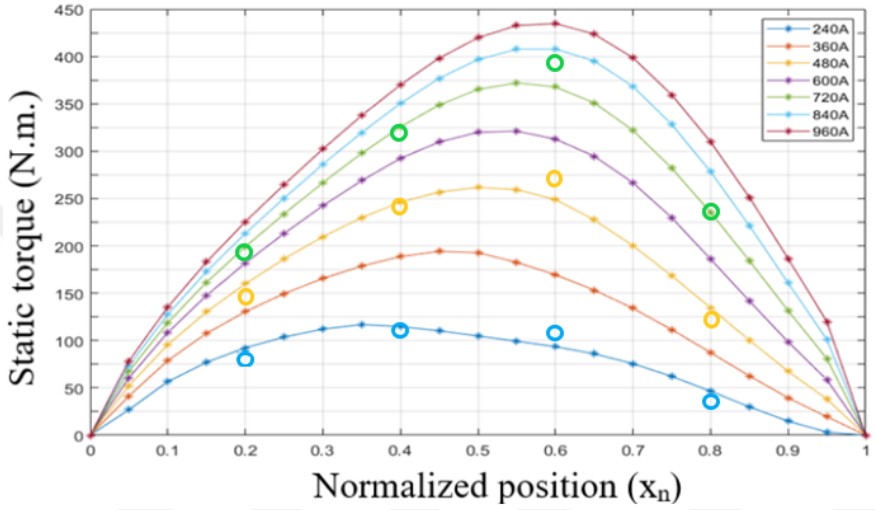

Figure 4.6. Static torque-position-current of SRM2 by optimization algorithm of this research, compared with the FEM calculations shown with circles

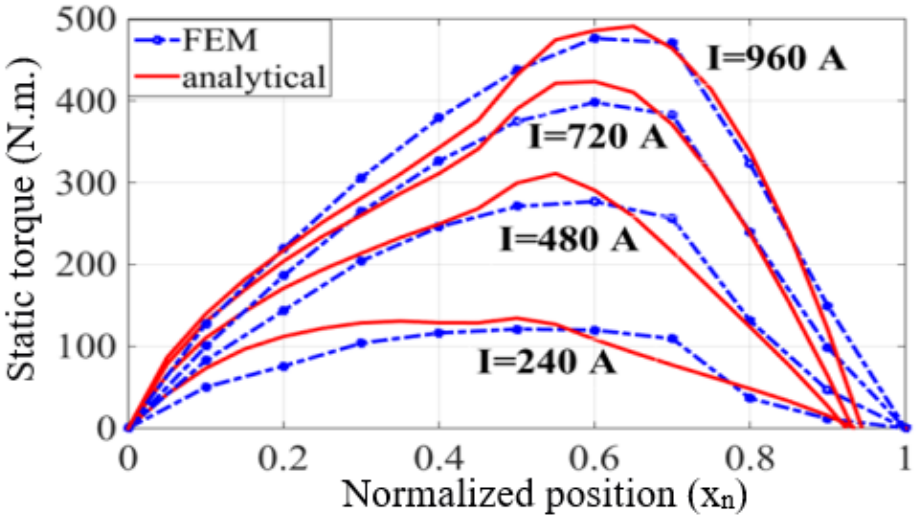

Figure 4.7. Static torque-position-current of SRM2 calculated in [23]

Comparison of Figure 4.6 and the FEM results from Figure 4.7 shows that the optimization static torque-position-current graph is calculated accurately.

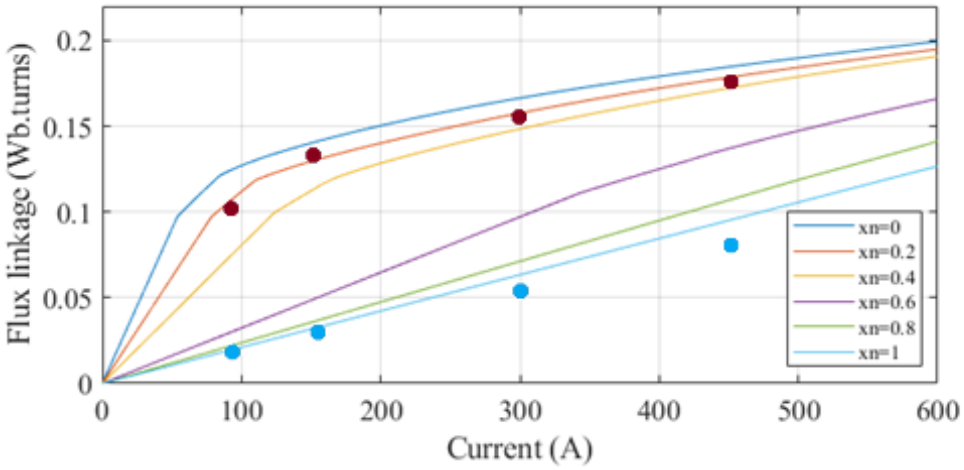

Figure 4.8. Flux linkage-current-position of SRM2 by optimization algorithm of this research with the dots corresponding to measured results for xn=0.2 and xn=1

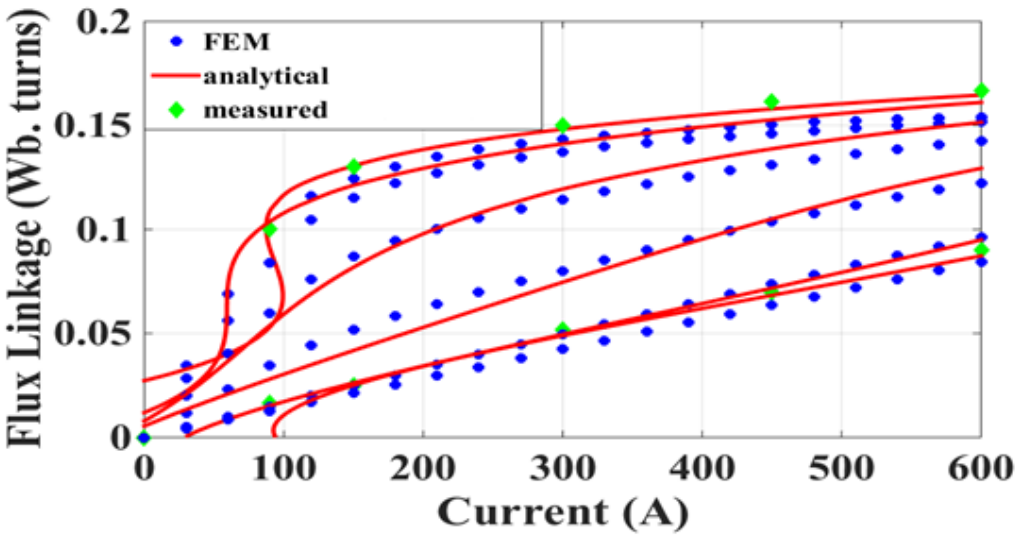

Figure 4.9. Flux linkage-current-position of SRM2 provided in [23], the green dots corresponding to measured results for xn=0.2 and xn=1

Comparison of results obtained in Figure 4.8 with the measurements and FEM results given in Figure 4.9 shows that the optimization flux linkage-current-position graph is calculated accurately.

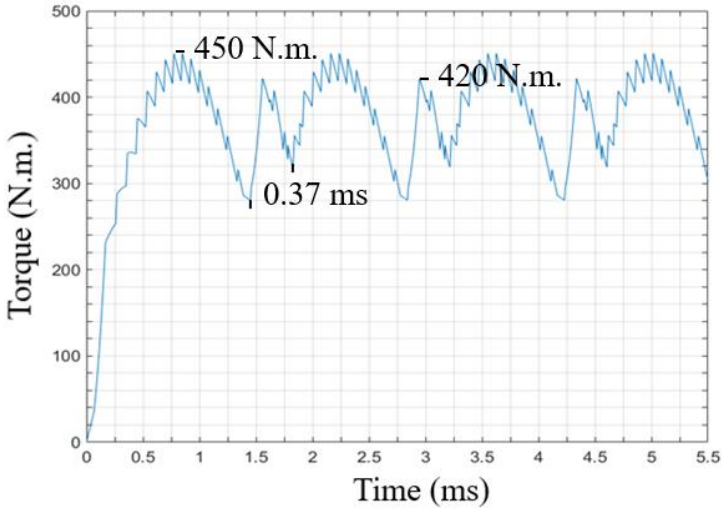

Figure 4.10. Instantaneous torque of SRM2 by optimization algorithm of this research

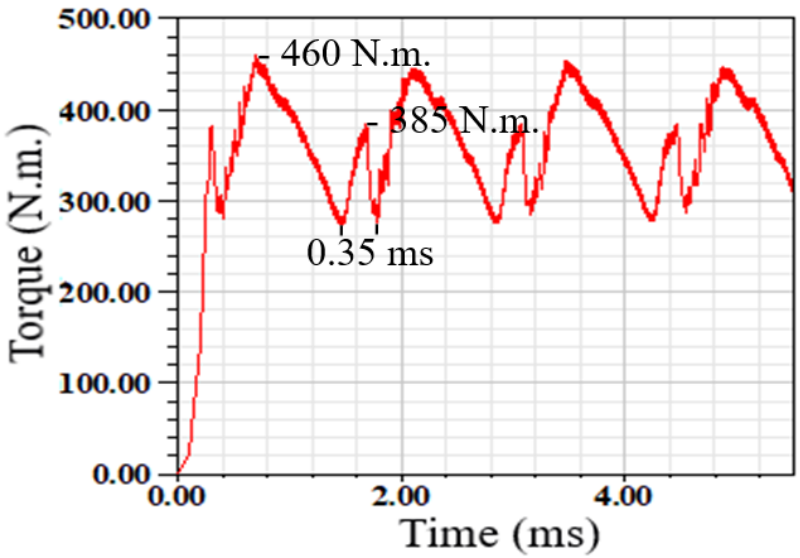

Figure 4.11. Instantaneous torque of SRM2 calculated in [23] by FEM

It should be noted that Figure 4.10 and FEM results given in Figure 4.11 show a graphical representation of the calculated instantaneous torque values. However, as it is not feasible to measure the instantaneous torque output of a SR motor, average torque values in Table 4.5 are used to confirm the accuracy.

In conclusion, the optimization process has been controlled for one step and has found to be accurate, thus concluding the optimization results to be reliable.

4.6. Optimization results for different pole combinations

This part of the research focuses on the results obtained using the optimization software for maximizing the average torque output of the specified motor subject to the defined constraints. As stated earlier, the purpose is to seek the best pole combination for the SRM which maximizes the average torque and torque density. The optimization algorithm is run for the following pole combinations.

1- 6/4
2- 8/6
3- 12/8
4- 18/12
5- 24/18
6- 32/24

The results for these combinations are given in the following pages. The previous calculation results obtained by Tarvirdilu [23] will also be provided for comparison.

4.6.1. Three phase 6/4 SRM

The highest torque produced by the 6/4 SRM has been simulated by genetic algorithm to be achieved with the following configuration. Below are the genetic algorithm results for this SRM, with the previous research results given alongside it.

Table 4.6. *Optimal values of the independent variables for 6/4 SRM*

	λ/g	t_s/λ	t_r/λ	D_{or} (mm)	K	Excitation period (electrical degrees)	Firing angle (electrical degrees)	Target average torque (N.m.)
Optimized 6/4 SRM - [23]	144.77	0.342	0.351	141.3	1.28	136.3	-4.3	67.52
Optimized 6/4 SRM - This research	148.517	0.354	0.356	149.398	1.315	145.939	-3.8	119.39

From these values, dimensions of the motor have been calculated as presented in Table 4.7.

Table 4.7. *Dimensions for the 6/4 SRM calculated from genetic algorithm results*

Dimension	**Optimized 6/4 SRM - This research**	**Optimized 6/4 SRM – [23]**
Rotor outer diameter	149.398 mm	141.3 mm
Stator outer diameter	269 mm	269 mm
Core length	115.5 mm	116.2 mm
Axial length	155 mm	155 mm
Stator back-core width	27.3 mm	24.3 mm
Shaft diameter	31.6 mm	31.4 mm
Air gap length	0.79 mm	0.77 mm
Rotor back-core width	27.3 mm	24.3 mm
Stator tooth tapering angle	2.215 degrees	2.215 degrees
Stator tooth width	41.5 mm	37.9 mm
Rotor tooth width	41.8 mm	38.9 mm
Stator pole depth	31.6 mm	39.1mm
Rotor pole depth	31.6 mm	30.7 mm
Number of turns per pole	72 turns	79 turns
One strand diameter	0.6 mm	0.6 mm
Number of strands	15	20

The operating pattern of the 6/4 optimized SRM is shown in the following Table 4.8.

Table 4.8. *Operating conditions for the 6/4 SRM*

Value	**Optimized 6/4 SRM – This research**	**Optimized 6/4 SRM – [23]**
I_{max}	138.01 A	127.5 A
I_{min}	127.4 A	117.68 A
Excitation period	0.8108 p.u. (145.939 electrical degrees)	0.7572 p.u. (136.3 electrical degrees)
Phase turn on angle	-3.8 electrical degrees	-4.3 electrical degrees
Speed	1200 rpm	1200 rpm

Table 4.9 shows the comparison of results previously calculated in [23] and the results obtained through optimization.

Table 4.9. *6/4 optimized SRM performance at 1200 rpm*

	Speed (rpm)	Average torque (N.m.)	Output power (kW)	RMS current (A)	RMS current density (A/mm^2)	Peak tooth flux density (T)	Copper loss (kW)	Core loss (W)	Total loss (kW)	Input power (kW)	Efficiency (%)
Optimized 6/4 SRM - [23]	1200	67.52	8.49	17.46	3.1	2	1.8	162.1	1.96	10.45	81
Optimized 6/4 SRM - This research	1200	119.4	15	64.47	15.2	2	3.47	139	3.61	18.61	80.6

Comparison shows that results in [23] are highly flawed in prediction of SRM characteristics. It needs to be mentioned that Tarvirdilu stated his optimization results for lower pole combinations were likely to be flawed [23]. This research has fixed those errors. It should be noted that the rms current density does not reach $33A/mm^2$. It will be seen in Section 4.8 that this is due to the supply DC voltage not being sufficient enough to increase the current further. The output power does not reach 50kW. Better results are obtained when number of poles are changed, which will be observed in the following configurations. Torque density, copper mass, iron mass and active mass of the 6/4 SRM can be observed at the Table 4.10.

Table 4.10. *Active mass and torque density results of the optimized 6/4 SRM*

	Iron mass (kg)	Copper mass (kg)	Total active mass (kg)	Torque density (N.m./kg)
Optimized 6/4 SRM – [23]	32.88	9.4	42.28	1.597
Optimized 6/4 SRM – This research	34.6	6.35	40.945	2.916

4.6.2. Four phase 8/6 SRM

The highest torque produced by the 8/6 SRM has been simulated by genetic algorithm to be achieved with the following configuration. Below are the genetic algorithm results for this SRM, with the previous research results given alongside it.

Table 4.11. *Optimal values of the independent variables for 8/6 SRM*

	λ/g	t_s/λ	t_r/λ	D_{or} (mm)	K	Excitation period (electrical degrees)	Firing angle (electrical degrees)	Target average torque (N.m.)
Optimized 8/6 SRM - [23]	121.92	0.339	0.339	165.22	1.522	127.04	-7.68	123.71
Optimized 8/6 SRM - This research	124.634	0.37	0.372	165.268	1.454	134.715	-7.388	146.4

Table 4.12. *Dimensions for the 8/6 SRM calculated from genetic algorithm results*

Dimension	**Optimized 8/6 SRM - This research**	**Optimized 8/6 SRM - [23]**
Rotor outer diameter	165.268 mm	165.22 mm
Stator outer diameter	269 mm	269 mm
Core length	119.6 mm	116.9 mm
Axial length	155 mm	155 mm
Stator back-core width	23.3 mm	22.3 mm
Shaft diameter	63.2 mm	63.8 mm
Air gap length	0.69 mm	0.71 mm
Rotor back-core width	23.3 mm	22.3 mm
Stator tooth tapering angle	2.215 degrees	2.215 degrees
Stator tooth width	32 mm	29.3 mm
Rotor tooth width	32.2 mm	29.3 mm
Stator pole depth	27.8 mm	28.4 mm
Rotor pole depth	27.8 mm	28.4 mm
Number of turns per pole	45 turns	51 turns
One strand diameter	0.6 mm	0.6 mm
Number of strands	12	11

Using the values at Table 4.11, dimensions of the motor have been calculated. These values are presented in Table 4.12.

The operating pattern of the 8/6 optimized SRM is shown in the Table 4.13.

Table 4.13. *Operating conditions for the 8/6 SRM*

Value	**Optimized 8/6 SRM -This research**	**Optimized 8/6 SRM – [23]**
I_{max}	181.9 A	165 A
I_{min}	167.9 A	152.3 A
Excitation period	0.7484 p.u. (134.715 electrical degrees)	0.706 p.u. (127.04 electrical degrees)
Phase turn on angle	-7.388 electrical degrees	-7.68 electrical degrees
Speed	1200 rpm	1200 rpm

Table 4.14 shows the comparison of results previously calculated in [23] and the results obtained through optimization.

Table 4.14. *8/6 optimized SRM performance at 1200 rpm*

	Speed (rpm)	Average torque (N.m.)	Output power (kW)	RMS current (A)	RMS current density (A/mm^2)	Peak tooth flux density (T)	Copper loss (kW)	Core loss (W)	Total loss (kW)	Input power(kW)	Efficiency (%)
Optimized 8/6 SRM - [23]	1200	123.7	15.55	23.6	7.6	2	4.9	305	5.2	20.75	74.9
Optimized 8/6 SRM - This research	1200	146.4	18.4	86.3	25.4	2	5.9	229	6.12	24.5	75.1

Examining the results at display at Table 4.14, it can be observed that this motor also cannot provide 50kW power output. Comparison with previous data shows a high error in calculations of [23]. Again it needs to be set clear that Tarvirdilu in [23] stated that optimization calculations at low pole combinations were very likely flawed.

Torque density, copper mass, iron mass and active mass of the motor can be observed at the Table 4.15.

Table 4.15. *Active mass and torque density results of the optimized 8/6 SRM*

	Iron mass (kg)	Copper mass (kg)	Total active mass (kg)	Torque density (N.m./kg)
Optimized 8/6 SRM – [23]	31.45	4.26	35.71	3.46
Optimized 8/6 SRM – This research	33.83	4.21	38.04	3.85

4.6.3. Three phase 12/8 SRM

The highest torque produced by the 12/8 SRM has been simulated by genetic algorithm to be achieved with the following configuration. Below are the genetic algorithm results for this SRM, with the previous research results given alongside it.

Table 4.16. *Optimal values of the independent variables for 12/8 SRM*

	λ/g	t_s/λ	t_r/λ	D_{or} (mm)	K	Excitation period (electrical degrees)	Firing angle (electrical degrees)	Target average torque (N.m.)
Optimized 12/8 SRM - [23]	81.2	0.431	0.452	166.2	1.297	149.35	-4.9	288.64
Optimized 12/8 SRM - This research	88.66	0.426	0.443	170.131	1.302	149.903	-3.905	298.94

From these values, dimensions of the motor have been calculated and presented in Table 4.17. As a follow-up, the operating pattern of the 12/8 optimized SRM is shown in the Table 4.18.

Table 4.17. *Dimensions for the 12/8 SRM calculated from genetic algorithm results*

Dimension	**Optimized 12/8 SRM - This research**	**Optimized 12/8 SRM - [23]**
Rotor outer diameter	170.131 mm	166.2 mm
Stator outer diameter	269 mm	269 mm
Core length	136.5 mm	137.2 mm
Axial length	155 mm	155 mm
Stator back-core width	18.5 mm	18.2 mm
Shaft diameter	72.8 mm	65.4 mm
Air gap length	0.754 mm	0.804 mm
Rotor back-core width	18.5 mm	18.2 mm
Stator tooth tapering angle	2.215 degrees	2.215 degrees
Stator tooth width	28.5 mm	28.1 mm
Rotor tooth width	29.6 mm	29.5 mm
Stator pole depth	30.1 mm	32.1 mm
Rotor pole depth	30.1 mm	32.1 mm
Number of turns per pole	22 turns	22 turns
One strand diameter	0.6 mm	0.6 mm
Number of strands	24	24

Table 4.18. *Operating conditions for the 12/8 SRM*

Value	**Optimized 12/8 SRM - This research**	**Optimized 12/8 SRM – [23]**
I_{max}	348.9 A	357.19 A
I_{min}	322.1 A	329.7 A
Excitation period	0.8328 p.u. (149.903 electrical degrees)	0.8297 p.u. (149.35 electrical degrees)
Phase turn on angle	-3.905 electrical degrees	-4.9 electrical degrees
Speed	1200 rpm	1200 rpm

Using the calculated dimensions and the operating patterns, the performance of the 12/8 optimized motor has been calculated. Table 4.19 shows the comparison of results previously calculated in [23] and the results obtained through optimization process of this research.

Table 4.19. *12/8 optimized SRM performance at 1200 rpm*

	Speed (rpm)	Average torque (N.m.)	Output power (kW)	RMS current (A)	RMS current density (A/mm^2)	Peak tooth flux density (T)	Copper loss (kW)	Core loss (W)	Total loss (kW)	Input power (kW)	Efficiency (%)
Optimized 12/8 SRM – [23]	1200	288.64	36.27	132.16	19.5	2	11.38	717	12.1	48.37	75
Optimized 12/8 SRM – This research	1200	298.94	37.57	195.34	28.79	2	11.33	807	12.14	49.7	75.6

Observation of Table 4.19 shows that rms current density and peak flux density are within the boundaries set for the optimization, however the motor is not able to achieve the 50kW output power. It needs to be mentioned that the rms current value and current density values calculated in [23] were inserted in the research with a mistake. The dimensions in both researches are highly similar and other performance results are calculated similarly. Checking the copper loss values, it can be made certain the current values provided in previous research are entered incorrectly. In [23], rms current is written divided by number of phases, whereas it should have been written divided by number of simultaneously excited pole pairs, which is 2 for a 12/8 SRM.

Torque density, copper mass, iron mass and active mass of the motor can be observed at the Table 4.20.

Table 4.20. *Active mass and torque density results of the optimized 12/8 SRM*

	Iron mass (kg)	Copper mass (kg)	Total active mass (kg)	Torque density (N.m./kg)
Optimized 12/8 SRM - [23]	39.95	5.94	45.88	6.29
Optimized 12/8 SRM - This research	39.42	5.81	45.23	6.61

4.6.4. Three phase 18/12 SRM

The highest torque produced by the 18/12 SRM has been simulated by genetic algorithm to be achieved with the following configuration. Given in Table 4.21 are the genetic algorithm results for this SRM, with the previous research results given alongside it. The dimensions calculated from these values are presented in Table 4.22.

Table 4.21. *Optimal values of the independent variables for 18/12 SRM*

	λ/g	t_s/λ	t_r/λ	D_{or} (mm)	K	Excitation period (electrical degrees)	Firing angle (electrical degrees)	Target average torque (N.m.)
Optimized 18/12 SRM - [23]	98.73	0.391	0.432	190.578	1.376	150.09	-4.61	401.7
Optimized 18/12 SRM - This research	86.161	0.391	0.433	186.501	1.354	153.692	-8.974	393.2

Table 4.22. *Dimensions for the 18/12 SRM calculated from genetic algorithm results*

Dimension	**Optimized 18/12 SRM - This research**	**Optimized 18/12 SRM - [23]**
Rotor outer diameter	186.501 mm	190.578 mm
Stator outer diameter	269 mm	269 mm
Core length	139.3 mm	139.1 mm
Axial length	155 mm	155 mm
Stator back-core width	12.9 mm	13.4 mm
Shaft diameter	115.3 mm	123.3 mm
Air gap length	0.567 mm	0.505 mm
Rotor back-core width	12.9 mm	13.4 mm
Stator tooth tapering angle	2.215 degrees	2.215 degrees
Stator tooth width	19.1 mm	19.5 mm
Rotor tooth width	21.1 mm	21.6 mm
Stator pole depth	27.8 mm	25.3 mm
Rotor pole depth	22.7 mm	20.2 mm
Number of turns per pole	14 turns	14 turns
One strand diameter	0.6 mm	0.6 mm
Number of strands	26	23

The operating pattern of the 18/12 optimized SRM is shown in the following Table 4.23.

Table 4.23. *Operating conditions for the 18/12 SRM*

Value	**Optimized 18/12 SRM -This research**	**Optimized 18/12 SRM - [23]**
I_{max}	378.5 A	343.1 A
I_{min}	349.4 A	316.7 A
Excitation period	0.8531 p.u. (153.7 electrical degrees)	0.834 p.u. (150.1 electrical degrees)
Phase turn on angle	-3.974 electrical degrees	-4.61 electrical degrees
Speed	1200 rpm	1200 rpm

Table 4.24 shows the comparison of results previously calculated in [23] and the results obtained through optimization.

Table 4.24. *18/12 optimized SRM performance at 1200 rpm*

	Speed (rpm)	Average torque (N.m.)	Output power (kW)	RMS current (A)	RMS current density (A/mm^2)	Peak tooth flux density (T)	Copper loss (kW)	Core loss (W)	Total loss (kW)	Input power (kW)	Efficiency (%)
Optimized 18/12 SRM – [23]	1200	401.4	50.44	200.8	30.9	2	11.03	1131	12.16	62.6	80.58
Optimized 18/12 SRM – This research	1200	393.2	49.4	225.3	30.65	2	12.59	1710	14.3	63.7	77.6

It can be seen that the optimization constraints are met. The current density rms value and tooth flux density are within the imposed constraints. The output power of the optimized 18/12 SRM is in very close boundary of the desired 50kW output power. This combination is seen to have the best desired results for the pole combinations tested on this research.

Torque density, copper mass, iron mass and active mass of the motor can be observed at the Table 4.25.

Table 4.25. *Active mass and torque density results of the optimized 18/12 SRM*

	Iron mass (kg)	Copper mass (kg)	Total active mass (kg)	Torque density (N.m./kg)
Optimized 18/12 SRM – [23]	33.07	5.18	38.25	10.2
Optimized 18/12 SRM – This research	33.51	5.7	39.21	10.03

4.6.5. Four phase 24/18 SRM

The highest torque produced by the 24/18 SRM has been simulated by genetic algorithm to be achieved with the following configuration. Below are the genetic algorithm results for this SRM, with the previous research results given alongside it.

Table 4.26. *Optimal values of the independent variables for 24/18 SRM*

	λ/g	t_s/λ	t_r/λ	D_{or} (mm)	K	Excitation period (electrical degrees)	Firing angle (electrical degrees)	Target average torque (N.m.)
Optimized 24/18 SRM - [23]	86.53	0.392	0.44	191.05	1.5	140	-10	353.5
Optimized 24/18 SRM - This research	82.147	0.388	0.438	193.063	1.544	135.109	-10.4	347.2

From these values, dimensions of the SR motor have been calculated and are presented in Table 4.27. The operating pattern of the 24/18 optimized SRM is further given in the Table 4.28. Both tables can be observed in the following page.

Table 4.27. *Dimensions for the 24/18 SRM calculated from genetic algorithm results*

Dimension	**Optimized 24/18 SRM - This research**	**Optimized 24/18 SRM - [23]**
Rotor outer diameter	193.063 mm	191.05 mm
Stator outer diameter	269 mm	269 mm
Core length	140.7 mm	141 mm
Axial length	155 mm	155 mm
Stator back-core width	10.1 mm	9.8 mm
Shaft diameter	140.1 mm	140.6 mm
Air gap length	0.41 mm	0.39 mm
Rotor back-core width	10.1 mm	9.8 mm
Stator tooth tapering angle	2.215 degrees	2.215 degrees
Stator tooth width	13.1 mm	13.1 mm
Rotor tooth width	14.8 mm	14.7 mm
Stator pole depth	27.5 mm	28.5 mm
Rotor pole depth	16.4 mm	15.4 mm
Number of turns per pole	10 turns	10 turns
One strand diameter	0.6 mm	0.6 mm
Number of strands	30	31

Table 4.28. *Operating conditions for the 24/18 SRM*

Value	**Optimized 24/18 SRM - This research**	**Optimized 24/18 SRM – [23]**
I_{max}	447.68 A	458.1
I_{min}	413.24 A	422.9
Excitation period	0.7506 p.u. (135.109 electrical degrees)	0.778 p.u. (140 electrical degrees)
Phase turn on angle	-10.4 electrical degrees	- 10 electrical degrees
Speed	1200 rpm	1200 rpm

Using the dimensional values and operating pattern calculated via the optimization process, performance of the 24/18 SRM is calculated. Table 4.29 shows the comparison of results previously calculated in [23] and the results obtained through optimization.

Table 4.29. *24/18 optimized SRM performance at 1200 rpm*

	Speed (rpm)	Average torque (N.m.)	Output power (kW)	RMS current (A)	RMS current density (A/mm^2)	Peak tooth flux	Copper loss (kW)	Core loss (W)	Total loss (kW)	Input power (kW)	Efficiency (%)
Optimized 24/18 SRM – [23]	1200	353.5	44.42	249.3	28.5	2	11.7	1287	12.98	57.4	77.4
Optimized 24/18 SRM – This research	1200	347.2	43.63	250	29.47	2	12.03	2532	14.56	58.2	75

The results show that the optimization constraints are met, however the motor cannot provide the desired output power of 50kW.

Torque density, copper mass, iron mass and active mass of the motor can be observed at the Table 4.30.

Table 4.30. *Active mass and torque density results of the optimized 24/18 SRM*

	Iron mass (kg)	Copper mass (kg)	Total active mass (kg)	Torque density (N.m./kg)
Optimized 24/18 SRM – [23]	28.44	6.34	34.78	10.16
Optimized 24/18 SRM – This research	28.69	6.2	34.89	9.95

4.6.6. Four phase 32/24 SRM

The 32/24 SRM is an addition to this research and is not provided within the research of Tarvirdilu [23]. The highest torque produced by the 32/24 SRM has been simulated by genetic algorithm to be achieved with the configuration provided at Table 4.31.

Table 4.31. *Optimal values of the independent variables for 32/24 SRM*

	λ/g	t_s/ λ	t_r/ λ	D_{or} (mm)	K	Excitation period (electrical degrees)	Firing angle (electrical degrees)	Target average torque (N.m.)
Optimized 32/24 SRM - This research	74.415	0.311	0.425	198.969	1.6	142.082	-15.784	348.6

From these values, dimensions of the motor have been calculated and presented in Table 4.32.

Table 4.32. *Dimensions for the 32/24 SRM calculated from genetic algorithm results*

Dimension	**Optimized 32/24 SRM - This research**
Rotor outer diameter	198.969 mm
Stator outer diameter	269 mm
Core length	141.5 mm
Axial length	155 mm
Stator back-core width	6.6 mm
Shaft diameter	157.8 mm
Air gap length	0.35 mm
Rotor back-core width	6.6 mm
Stator tooth tapering angle	2.215 degrees
Stator tooth width	8.1 mm
Rotor tooth width	11.1 mm
Stator pole depth	28.3 mm
Rotor pole depth	14 mm
Number of turns per pole	9 turns
One strand diameter	0.6 mm
Number of strands	31

The operating pattern of the 32/24 optimized SRM is shown in the following Table 4.33 which can be observed in the following page.

Table 4.33. *Operating conditions for the 32/24 SRM*

Value	**Optimized 32/24 SRM – This research**
I_{max}	455.2 A
I_{min}	420.2 A
Excitation period	0.7893 p.u. (142.082 electrical degrees)
Phase turn on angle	-15.784 electrical degrees
Speed	1200 rpm

Table 4.34 shows the performance results obtained through optimization.

Table 4.34. *32/24 optimized SRM performance at 1200 rpm*

	Speed (rpm)	Average torque (N.m.)	Output power (kW)	RMS current (A)	RMS current density (A/mm^2)	Peak tooth flux density (T)	Copper loss (kW)	Core loss (W)	Total loss (kW)	Input power (kW)	Efficiency (%)
Optimized 32/24 SRM – This research	1200	348.6	43.8	264.45	30.17	2	15.42	5484	20.9	64.7	67.7

The results for the 32/24 SRM show that the output power of 50kW cannot be reached. It can be seen that in this SRM copper losses and especially core losses are high, resulting in a lower efficiency.

Torque density, copper mass, iron mass and active mass of the motor can be observed at the Table 4.35.

Table 4.35. *Active mass and torque density results of the optimized 32/24 SRM*

	Iron mass (kg)	Copper mass (kg)	Total active mass (kg)	Torque density (N.m./kg)
Optimized 32/24 SRM - This research	28.69	6.2	34.89	9.99

4.7. Comparison of the results

In this section, the optimization results obtained in this research will be presented for each pole ratio. Table 4.36 shows the genetic algorithm results obtained for different pole combinations as well as the target average torque. It should be noted that 32/24 SRM is calculated under this research and is not included within the previous research [23].

Table 4.36. *The independent variables and average torque results for different combinations of poles*

	λ/g	t_s/λ	t_r/λ	D_{or} (mm)	K	Excitation period (electrical degrees)	Firing angle (electrical degrees)	Target average torque (N.m.)
Optimized 6/4 SRM - This research	148.517	0.354	0.356	149.398	1.315	145.939	-3.8	119.39
Optimized 8/6 SRM - This research	124.634	0.37	0.372	165.268	1.454	134.715	-7.388	146.4
Optimized 12/8 SRM - This research	88.66	0.426	0.443	170.131	1.302	149.903	-3.905	298.94
Optimized 18/12 SRM - This research	86.161	0.391	0.433	186.501	1.354	153.692	-8.974	393.2
Optimized 24/18 SRM - This research	82.147	0.388	0.438	193.063	1.544	135.109	-10.4	347.2
Optimized 32/24 SRM - This research	74.415	0.311	0.425	198.969	1.6	142.082	-15.784	348.6

The dimensional results corresponding to the six optimized switched reluctance motors can be observed in the following Table 4.37.

Table 4.37. *Optimized SRM dimensions calculated in this research*

	Optimized SRM pole combinations - This research					
Dimension	**6/4**	**8/6**	**12/8**	**18/12**	**24/18**	**32/24**
Rotor outer diameter	149.398 mm	165.268 mm	170.131 mm	186.501 mm	193.063 mm	198.969 mm
Stator outer diameter	269 mm	269 mm	269 mm	269 mm	269 mm	269 mm
Core length	115.5 mm	119.6 mm	136.5 mm	139.3 mm	140.7 mm	141.5 mm
Axial length	155 mm	155 mm	155 mm	155 mm	155 mm	155 mm
Stator back-core width	27.3 mm	23.3 mm	18.5 mm	12.9 mm	10.1 mm	6.6 mm
Shaft diameter	31.6 mm	63.2 mm	72.8 mm	115.3 mm	140.1 mm	157.8 mm
Air gap length	0.79 mm	0.69 mm	0.754 mm	0.567 mm	0.41 mm	0.35 mm
Rotor back-core width	27.3 mm	23.3 mm	18.5 mm	12.9 mm	10.1 mm	6.6 mm
Stator tooth tapering angle	2.215 degrees	2.215 degrees	2.215 degrees	2.215 degrees	2.215 degrees	2.215 degrees
Stator tooth width	41.5 mm	32 mm	28.5 mm	19.1 mm	13.1 mm	8.1 mm
Rotor tooth width	41.8 mm	32.2 mm	29.6 mm	21.1 mm	14.8 mm	11.1 mm
Stator pole depth	31.6 mm	27.8 mm	30.1 mm	27.8 mm	27.5 mm	28.3 mm
Rotor pole depth	31.6 mm	27.8 mm	30.1 mm	22.7 mm	16.4 mm	14 mm
Number of turns per pole	72 turns	45 turns	22 turns	14 turns	10 turns	9 turns
One strand diameter	0.6 mm	0.6 mm	0.6 mm	0.6 mm	0.6 mm	0.6 mm
Number of strands	15	12	24	26	30	31

Following Table 4.38 shows the combined performance results for optimized SRMs with different pole numbers.

Table 4.38. *Results of the optimized SRM performance calculations*

	Speed (rpm)	Average torque (N.m.)	Output power (kW)	RMS current (A)	RMS current density (A/mm^2)	Copper loss (kW)	Core loss (W)	Total loss (kW)	Input power (kW)	Efficiency (%)
Optimized 6/4 SRM - This research	1200	119.4	15	64.47	15.2	3.47	139	3.61	18.61	80.6
Optimized 8/6 SRM - This research	1200	146.4	18.4	86.3	25.4	5.9	229	6.12	24.5	75.1
Optimized 12/8 SRM - This research	1200	298.94	37.57	195.34	28.79	11.33	807	12.14	49.7	75.6
Optimized 18/12 SRM - This research	1200	393.2	49.4	225.3	30.65	12.59	1710	14.3	63.7	77.6
Optimized 24/18 SRM - This research	1200	347.2	43.63	250	29.47	12.03	2532	14.56	58.2	75
Optimized 32/24 SRM - This research	1200	348.6	43.8	264.45	30.17	15.42	5484	20.9	64.7	67.7

4.8. Discussion of the results

In this section, the results obtained from the optimization will be evaluated and compared with the test results obtained by Chiba [3].

This evaluation firstly will consider the geometrical results obtained from the optimization and discuss the consequence of the constraints imposed. Later, performance related results for the optimized motors for each pole combination will be presented and in the light of these results, whether the constraints imposed are reasonable and whether better results would be obtained with different constraints will be discussed.

It can be seen from Table 4.37 that all the optimized motors have a common axial length of 155 mm and a stator outer diameter value of 269mm. Also, the performance results in Section 4.6 show that for all the optimized designs of the SRMs with different pole combinations, the stator tooth flux density reaches the limit of 2T, in order to produce the maximum value of torque.

It should be noted that the normalized data that are used to design the optimized SRMs come from the model given in Figure 1.1, which has a core material of M36 steel. However, core losses of the optimized SRMs are calculated from the B-H data of 10JNEX900 material. This can result in slight inaccuracies in the performances calculated for the optimized SRMs. Comparison of the B-H data of M36 steel and 10JNEX900 material can be found in Figure A.6 located in Appendices Section A.

Another issue to be noted is that the optimizations are done with dimensional boundaries. In further research, the results can be generalized and presented in a dimensionless manner in order to provide a method to help choose the optimal pole combinations for different motors.

Geometry related results for the SRMs are given from Figure 4.12 to Figure 4.17. Performance related results at 1200 rpm are given from Figure 4.17 to Figure 4.26. The values for the existing SRM are given in the description of these figures.

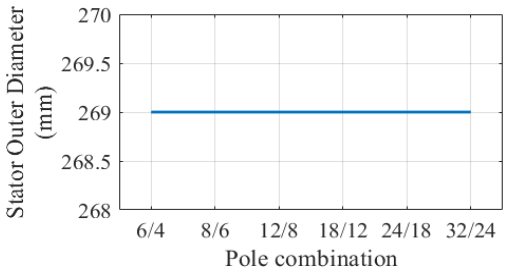

Figure 4.12. Stator outer diameter for different pole combinations (Existing: 269mm)

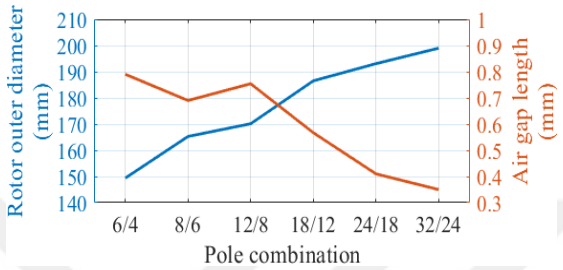

Figure 4.13. Rotor outer diameter and air gap length for different pole combinations (Existing: D_{or}=179mm, g=0.5mm)

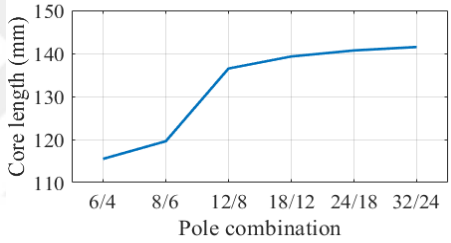

Figure 4.14. Core length for different pole combinations (Existing: 135mm)

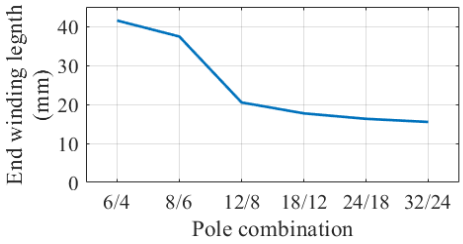

Figure 4.15. End winding length for different pole combinations (Existing: 20mm)

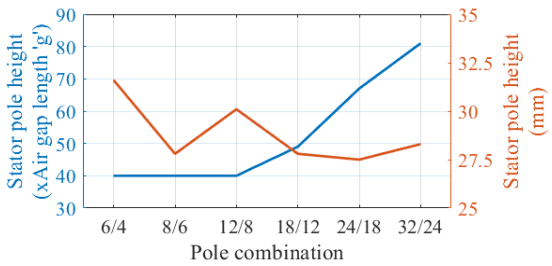

Figure 4.16. Stator pole height for different pole combinations (Existing: 54.5g=27.25mm)

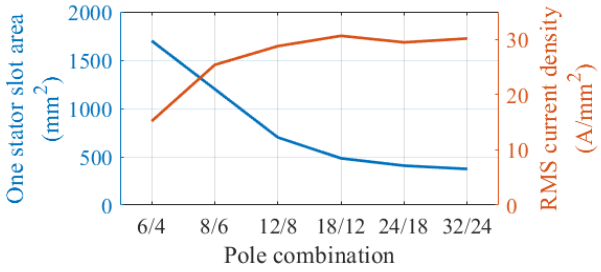

Figure 4.17. Stator slot area and rms current density for different pole combinations (Existing: A_{slot}=508mm^2, J_{rms}=33A/mm^2)

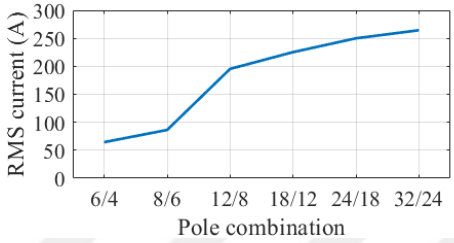

Figure 4.18. RMS current for different pole combinations (Existing: 206A)

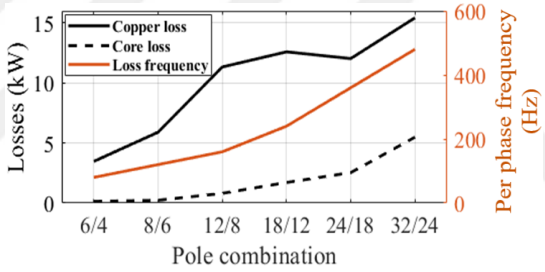

Figure 4.19. Losses for different pole combinations (Existing: P_{cu}=13.49 kW, P_c=1.38 kW)

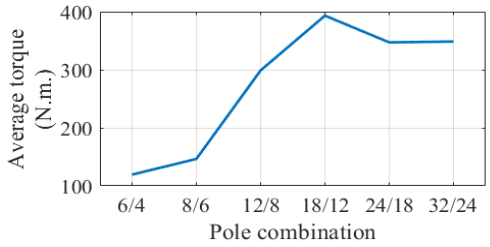

Figure 4.20. Average torque for different pole combinations (Existing: 366 N.m.)

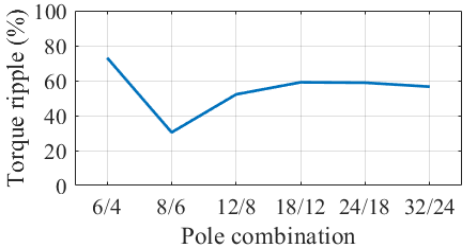

Figure 4.21. Torque ripple for different pole combinations (Existing: 37.6 %)

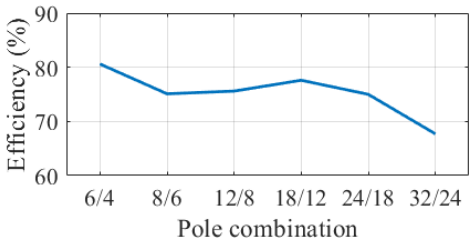

Figure 4.22. Efficiency for different pole combinations (Existing: 75.83 %)

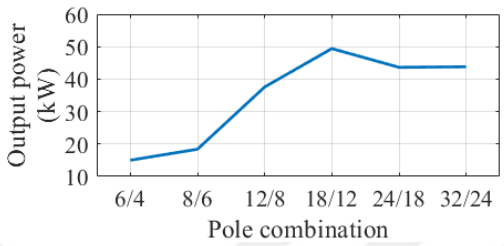

Figure 4.23. Output power for different pole combinations (Existing: 45.99 kW)

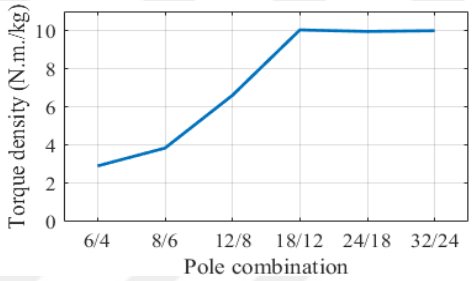

Figure 4.24. Torque density for different pole combinations (Existing: 9.17 N.m./kg)

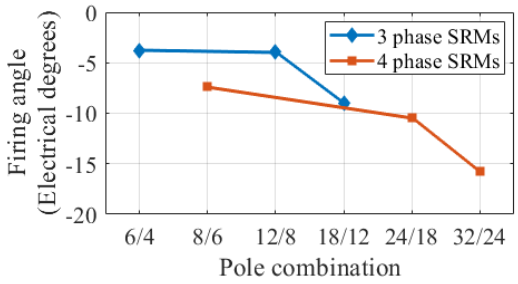

Figure 4.25. Firing angle for different pole combinations (Existing: -4 degrees electrical)

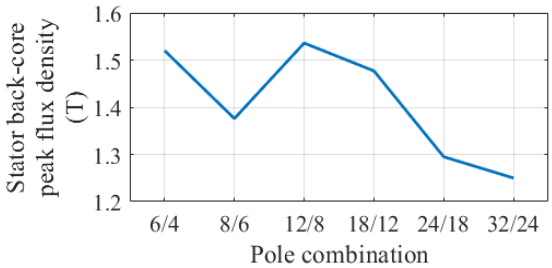

Figure 4.26. Peak values of the stator back-core flux densities (Existing: 0.96 T)

Following are the discussions on the presented figures.

1- Figure 4.12 shows that stator outer diameters of all the optimized SRMs with different pole combinations reach 269mm, which is the limit set for the optimization. This is expected as the output torque is highly dependent on size.

2- Figure 4.13 shows that, with increasing number for the pole combinations, rotor outer diameter values increase, and air gap length tends to decrease. As the number of turns decrease with increasing number of pole combinations, required stator slot area decreases, thus the stator pole height decreases. As the torque is proportional to the bore diameter, lower number of turns per pole are preferred due to the fact that increasing bore diameter values give higher average torque values.

3- Figure 4.14 shows that core length increases with increasing number of pole combinations. As there are lower number of turns for higher pole combinations, the core can have a larger space since the axial length of the motor has a fixed value in this optimization process.

4- Figure 4.15 shows that the end winding lengths decrease with increasing number of pole combinations. This is due to the number of turns per pole becoming lower as the pole combinations reach higher values. Thus, increasing number of turns per pole which is observed as the number of pole combinations decrease result in a higher end winding length and consequently a lower core length, which results in lower torque values as the active mass decreases.

5- Figure 4.16 shows that stator pole height to air gap ratio tends to increase for higher number of pole combinations.

6- Figure 4.17 shows that slot area decreases with increasing number of pole combinations. This is because smaller amount of flux is needed to achieve flux density of 2T. Also, rms value of the current density tends to increase and come closer to the limit of 33A/mm^2 with increasing number of pole combinations, which is expected to produce the highest possible torque. However, this is not the case for lower pole combinations. From Figure 4.16, it can be seen that stator pole height over air gap length values are at the lowest limit of 40g for lower pole combinations, and Figure 4.26 shows that peak values of the stator back-core flux densities do not reach the limit of 2T. This suggests that, for lower pole combinations, increasing DC supply voltage can provide higher currents, thus increasing average torque, current density and output power. It should be noted in this case, optimized dimensions should be recalculated.

7- Figure 4.18 shows that rms current values tend to increase with increasing number of pole combinations. Increasing number of simultaneously excited pole pairs and number of phases contribute to this result.

8- Figure 4.19 shows the copper and core losses. Table 4.38 and Figure 4.18 show that rms value of the current increases with increasing number of pole combinations. Also, total winding length and number of simultaneously excited pole pairs affect the copper loss values. Core losses increase with increasing number of simultaneously excited pole pairs as well as increasing switching frequency. In 32/24 SRM, 4 pole pairs are simultaneously excited, and the switching frequency is high. Thus, high copper and core losses are observed. It should be noted that in a 32/24 SRM, due to the high values of copper and core losses, the cooling method becomes of great importance and will have a big effect on the maximum value of both the rms current and the average torque, especially when the dimensions are limited for the design. In this research, thermal analysis is not conducted, and the copper losses are calculated with the copper resistivity at 80°C.

9- For better understanding the average torque vs pole combination data given at Figure 4.20, the number of simultaneously excited pole pairs needs to be mentioned. In 6/4 and 8/6 SRMs, one pole pair is excited for each phase. This value is 2 simultaneous pole pair excitations for 12/8 SRM, 3 simultaneous pole pair excitations for 18/12 and 24/18 SRM and 4 simultaneous pole pair excitations for the 32/24 SRM. Up until 18/12 SRM, the average torque increases as the number of simultaneously excited pole pairs increase. The average torque result shows that 18/12 pole combination provides the highest torque for the SRM. This value is higher than the average torque of the 24/18 SRM, thus concluding that the SRM has a higher torque at three phase operation compared to four phase operation when there are three simultaneous pole pair excitations, as the active mass is higher for the 18/12 SRM. It is important to note that the stator tooth flux density constraints are the same for all pole combinations. The 32/24 SRM has just slightly higher torque compared to 24/18 SRM. This is where the dimensional boundaries start to be a very important limiting factor. 32/24 SRM and 24/18 SRM both have similar active masses, which is lower than the active mass of 18/12 SRM. Thus, it can be said that after a certain pole combination, average torque is mainly dependent on the active mass of the motor. Also, for lower number of pole combinations where the rms value of the current density does not reach $33A/mm^2$, increasing DC supply voltage would provide a higher torque value.

10- Figure 4.21 shows the torque ripple values for the optimized SRMs. The ripple values are in general higher than the existing motor. Overlaps in phases where positive torque is produced is a main reason for this, as the optimization is done to achieve the maximum possible average torque value.

11- Figure 4.22 shows the efficiency values for the optimized SRMs. It should be noted that copper and core losses increase for higher number of pole combinations.

12- Figure 4.23 shows that until 18/12 SRM, output power increases with increasing number of pole combinations. After this value, output power decreases as the active mass of the motor that contributes to the torque production decreases, as can be seen in the results given in Section 4.6.

13- Figure 4.24 shows that rising number of pole pairs lead to a higher torque density value, in other words a higher torque per active mass value. It should be noted that the torque density of 3 phase 18/12 SRM, although being slightly higher, has almost the same value as the 24/18 SRM and 32/24 SRM. This means that after a certain pole combination, torque densities become very similar and selection in between becomes a matter of average torque and efficiency values, in which 18/12 SRM excels above the other pole combinations.

14- Figure 4.25 shows that with increasing number for the pole pairs, earlier firing is required to allow the current enough time to rise. For similar number of simultaneously excited pole pairs, it can be seen that compared to 3 phase SRMs, 4 phase SRMs require an earlier firing.

15- Figure 4.26 shows the peak values of the stator back-core flux densities. It should be noted that flux densities in the stator back-core do not reach the set peak limit of 2T. This is expected as K value is taken greater than 1 and stator tooth flux density limit is set to 2T.

Obtained results show that the best pole combination for the SRM is reached at the 18/12 pole combination. Table 4.39 provides comparisons of the measurement results, simulated performance results for the existing SRM and optimized performance results of the 18/12 SRM.

Table 4.39. *Comparison of the existing and optimized 18/12 SRMs*

	Speed (rpm)	Average torque (N.m.)	Output power (kW)	RMS current (A)	Copper loss (kW)	Core loss (kW)	Total loss (kW)	Input power (kW)	Efficiency (%)
Measurement results	1200	366	45.99	206	-	-	-	-	-
Simulated performance results of the existing 18/12 SRM	1200	371.3	46.65	196.8	13.49	1.38	14.87	61.52	75.83
Optimized performance of the 18/12 SRM	1200	393.2	49.4	225.3	12.59	1.71	14.3	63.7	77.6

Comparing the simulated performance results for existing and optimized 18/12 SRMs, it can be seen from Table 4.39 that optimized SRM has a 5.9 percent higher output torque and efficiency has increased by 1.8 percent. Output power is also much closer to the desired 50kW value.

A final comparison is made for the change in active mass and torque density for the existing and optimized 18/12 SRMs. These values can be seen at Table 4.40. It should be noted that switching frequencies and cooling methods are taken the same.

Table 4.40. *Differences of the torque density and active mass of existing and optimized 18/12 SRMs*

	Iron mass (kg)	Copper mass (kg)	Total active mass (kg)	Torque density (N.m./kg)
Existing 18/12 SRM (Simulated)	34.7	5.81	40.51	9.17
Optimized 18/12 SRM	33.51	5.7	39.21	10.03
Change (%)	-3.43	-1.2	-3.21	+9.38

It is seen on Table 4.40 that the total active mass of the motor has been reduced while sustaining a 9.4 percent increase on the torque density of the motor. By the results and changes provided in Table 4.39 and Table 4.40, it can be said that the optimization has been successful.

CHAPTER 5

CONCLUSIONS AND FUTURE WORK

5.1. Conclusions

This research has focused on calculating the performance of different switched reluctance motors and finding an optimum pole combination for the desired SRM. For this purpose, firstly the mistakes found in previous research [23] have been corrected. The calculation time has been reduced from hours to minutes with the usage of polynomial fitting instead of neural networks. With the comparisons done on the results of developed software, previous research and the measurement results, the validity of the approach has been confirmed.

A user interface has been created and introduced to the SR motor performance calculation software in this research. This interface holds a high importance as it allows the SRM performances to be easily calculated. Microsoft Visual Studio and MATLAB have been utilized in this research, both programs being highly supported thus ensuring not to be obsolete in the foreseeable future. The user interface is now also capable of warning the user if faulty data is entered. Data can be saved and reloaded, and the results can be saved.

Optimization process to find the pole combination delivering the highest possible output torque has been introduced after assuring the validity of the calculations. This is done by defining the desired range in which the independent variables are to change and using genetic algorithm optimization method of MATLAB [30]. A design method has been introduced to calculate the motor dimensions and the optimization results are calculated within specified boundaries.

This research has found with comparison of different pole combinations that pole combination of 18/12 gives the highest torque for the SRM, while staying inside optimization boundaries. It is important to note that previous study by Tarvirdilu [23] has also reached this pole combination, however, performance calculations in [23] have faulty results. Especially for 6/8 and 8/6 SRMs, performance results have been considerably corrected. The existing motor (SRM2) is also a 18/12 SRM [3], however, the optimized results show how the design of the existing SRM could be changed to utilize its performance. Existing performance of SRM2 has been calculated to deliver 46.65 kW of power under 1200 rpm (measured value being 45.99 kW), with a torque density of 9.17 N.m./kg. The optimized motor delivers 49.4 kW power under 1200 rpm, with a torque density of 10.03 N.m./kg. Torque density has been increased by 9.38 percent and efficiency has been increased from 75.83 percent to 77.6 percent.

5.2. Future Work

For future work purposes, the following statements are offered.

1- The SRM, by changing firing angles, can be modelled to work as a generator.
2- Polynomial fitting can be changed with a method providing higher accuracy.
3- Core loss calculations can be done with a more accurate method.
4- Number of independent variables in optimization procedure can be increased to achieve higher accuracies and better results, such as addition of DC supply voltage as an independent variable. Also, multi-purpose optimization for more than one objective function can be implemented, such as maximizing torque while keeping the torque ripple to a minimum, or weight and efficiencies can be used as the objective functions.
5- Thermal analysis needs be added to find the operating temperature within the SRM, considering the cooling method and isolation type.
6- Optimization could be changed to provide generalized dimensionless data which can help choose optimal pole combinations for different motors.

REFERENCES

[1] Xue, X. D., Cheng, K. W., and Cheung, N. C. 2008. Selection of electric motor drives for electric vehicles. Australasian Universities Power Engineering Conference AUPEC'08. pp. 1–6.

[2] Lawrenson, P., Stephenson, J., Blenkinsop, P., Corda, J., and Fulton, N. 1980. Variable-speed switched reluctance motors. Proceedings of IEE, 127 (B). pp. 253-265.

[3] Chiba, A., Kiyota, K., Hoshi, N., Takemoto, M., and Ogasawara, S. 2015. Development of a rare-earth-free SR motor with high torque density for hybrid vehicles. IEEE Transactions on Energy Conversion, 30. pp. 175-182.

[4] Kiyota , K., Kakishima, T., and Chiba, A. 2014. Cylindrical rotor design for acoustic noise and windage loss reduction in switched reluctance motor for HEV applications. Energy Conversion Congress and Exposition IEEE. pp. 1814-1821.

[5] Miller, T.J.E. 1989. Brushless Permanent-Magnet and Reluctance Motor Drives: New York, NY. pp. 149-156.

[6] Ertan, H. B., Harris, M. R., Andjargholi, V., Lawrenson, P. J., and Hughes, A. 1977. Unifying approach to the static torque of stepping-motor structures. doi:10.1049/piee.1977.0254.

[7] Rahman, K. M., and Schulz, S. E. 2002. Design of high-efficiency and high-torque-density switched reluctance motor for vehicle propulsion. IEEE Transactions on Industry Applications, 38. pp. 1500-1507.

[8] Chiba, A., Takano, Y., Takeno, M., Imakawa, T., Hoshi, N., and Takemoto, M. 2011. Torque density and efficiency improvements of a switched reluctance motor without rare-earth material for hybrid vehicles. IEEE Transactions on Industry Applications, 47. pp. 1240-1246.

[9] Gao, J., Sun, H., He, L., Dong, Y., and Zheng, Y. 2011. Optimization design of switched reluctance motor based on particle swarm optimization. International Conference on Electrical Machines and Systems ICEMS'11. pp. 1-5.

[10] Ma, C., and Qu, L. 2015. Multiobjective Optimization of Switched Reluctance Motors Based on Design of Experiments and Particle Swarm Optimization. IEEE Transactions on Energy Conversion, 30. pp. 1144-1153.

[11] Rafajdus, P., Peniak, A., Peter, D., Makys, P., and Szabo, L. 2014. Optimization of switched reluctance motor design procedure for electrical vehicles. International Conference on Optimization of Electrical and Electronic Equipment OPTIM'14. pp. 397-404.

[12] Xue, X., Cheng, K. W. E., Ng, T. W., and Cheung, N. C. 2010. Multi-objective optimization design of in-wheel switched reluctance motors in electric vehicles. IEEE Transactions on Industrial Electronics, 57. pp. 2980-2987.

[13] Ertan, H. B., and Leblebicioğlu, K. 2000. Optimum geometry for torque ripple minimization of switched reluctance motors. IEEE Transactions on Energy Conversion, 15. pp. 30-39.

[14] Sahin, F. 1996. Optimum geometry for torque ripple minimization of switched reluctance motors. MSc, Electrical and Electronics Engineering, Middle East Technical University.

[15] Bizkevelci, E., 2008. A control algorithm to minimize torque ripple and acoustic noise of switched reluctance motors. Ph.D., Electrical and Electronics Engineering, Middle East Technical University.

[16] Yıldız, A., and Polat, M., 2019. Investigation of the effect of stator and rotor pole ratios on torque and efficiency in Inverted Switched Reluctance Motor. Journal of Engineering and Technology, 3. pp. 12-24.

[17] Bilgin, B, Jiang, J. W., and Emadi, A., 2018. Switched Reluctance Motor Drives: Fundamentals to Applications, Boca Raton, FL.

[18] Ertan, H. B. 1986. Analytical prediction of torque and inductance characteristics of identically slotted doubly-salient reluctance motors. IEE Proceedings, 133 (B), 4.

[19] Ertan, H. B., and Tohumcu, M. 1982. A method for optimum design of switched reluctance motors, Ankara, Turkey. pp. 551-555.

[20] Beşenek, M. 1988. Numerically calculated force and permeance data for doubly salient geometries. MSc, Electrical and Electronics Engineering, Middle East Technical University.

[21] Mahariq, I. 2009. A Normalized set of force and permeance data for doubly-salient magnetic geometries. MSc, Electrical and Electronics Engineering, Middle East Technical University.

[22] Göynük, Y. 2008. Development of an electrical machines analysis and optimum design software package. MSc, Electrical and Electronics Engineering, Middle East Technical University.

[23] Tarvirdilu, R. A. 2016. Optimum pole combination to maximize torque density in switched reluctance motors for electric vehicle applications. MSc, Electrical and Electronics Engineering, Middle East Technical University.

[24] O'Connell, T.C. 2008. An investigation of boundary-based field analysis methods for electric machines: The Schwarz-Christoffel and boundary element methods: ProQuest.

[25] Tohumcu, M. 1985. Optimum design of switching reluctance motors. Ph.D., Electrical and Electronics Engineering, Middle East Technical University.

[26] Akiror , J. C., and Pillay, P. 2012. On the coefficients of core loss formulas for electrical machines. IEEE Industrial Electronics Society 38th Annual Conference IECON'12. pp. 1927-1933.

[27] Chen, Y., and Pillay, P. 2002. An improved formula for lamination core loss calculations in machines operating with high frequency and high flux density excitation. Industry Applications Conference 37th IAS Annual Meeting. pp. 759-766.

[28] Mthombeni, T. L., and Pillay, P. 2006. Physical basis for the variation of lamination core loss coefficients as a function of frequency and flux density. 32nd Annual Conference on IEEE Industrial Electronics IECON'06. pp. 1381-1387.

[29] Black, S., and Bilal, H. Z. 2006. Computing ripple effect for object oriented software. London South Bank University, London. pp. 3-7.

[30] The MathWorks, I. 2019. MATLAB Optimization Toolbox. Natick, Massachusetts, United States. Retrieved December 5, 2019, from mathworks.com/discovery/genetic-algorithm.html

APPENDICES

A. Material properties of the 10JNEX900 material and M36 steel material

Given in the following are the B-H curve values of M36 steel with 0.63mm laminations and 24 gauge, which is used in SRM1 [14, 18, 23].

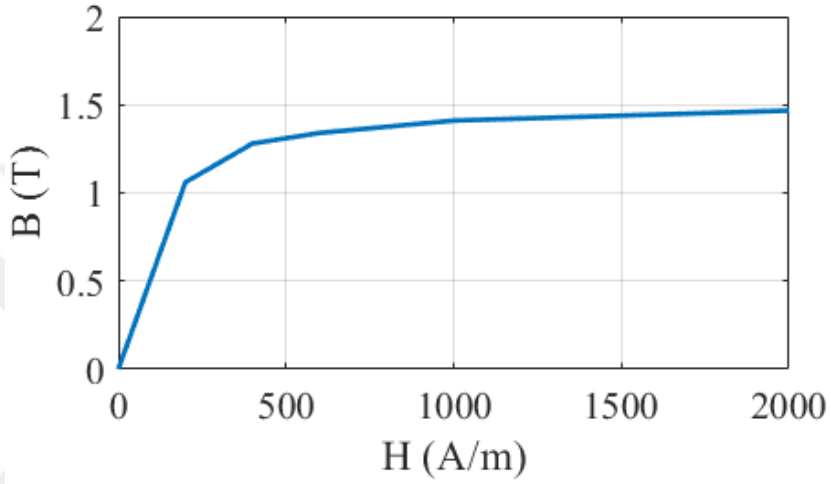

Figure A.1. B-H curve of M36 steel

Table A.1. *B-H curve values of the M36 steel*

H (A/m)	B (T)
0	0
200	1.06
400	1.28
600	1.34
1000	1.41
4000	1.58
10000	1.72
20000	1.85
30000	1.9
60000	2

The following data are used to calculate the core losses of M36 steel core.

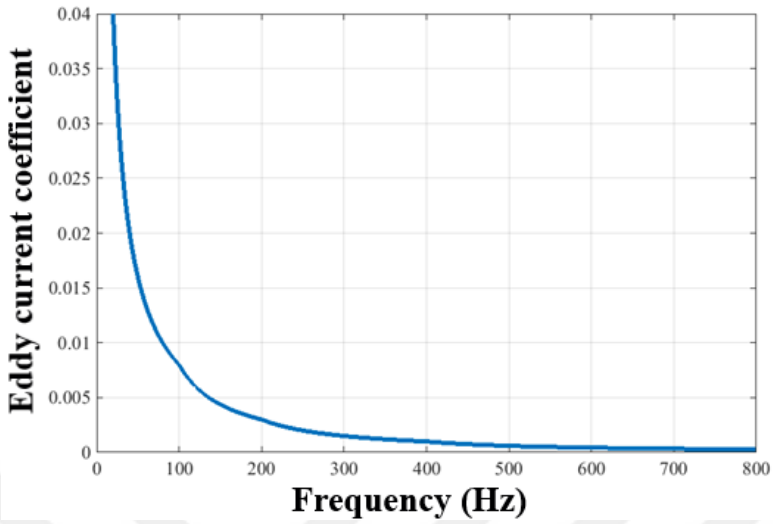

Figure A.2. Eddy current coefficient vs frequency of M36 steel

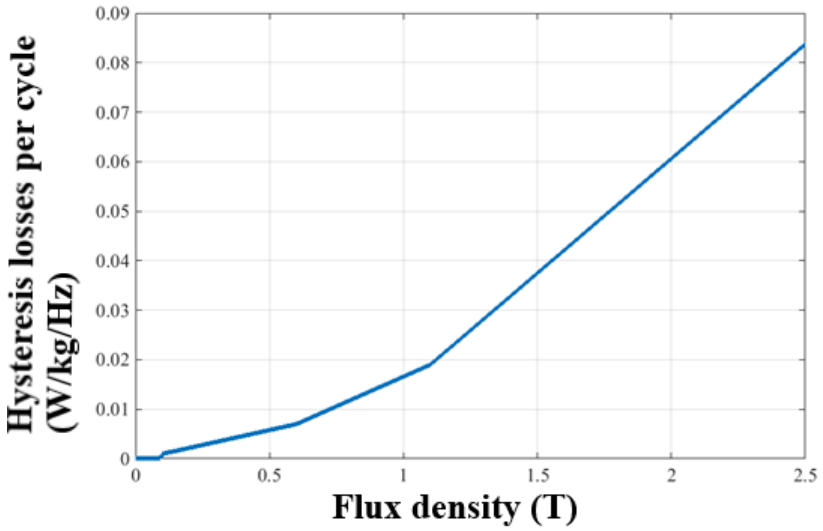

Figure A.3. Hysteresis loss per cycle vs flux density of M36 steel

Given in the following are the B-H curve data of 10JNEX900 material with 0.1 mm laminations, which is used in SRM2 [23].

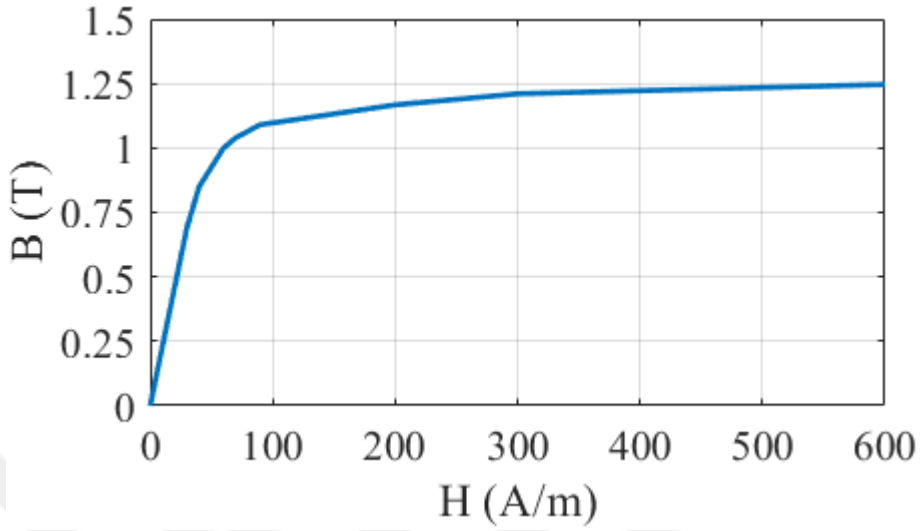

Figure A.4. B-H curve of 10JNEX900 material

Table A.2. *B-H curve values of 10JNEX900 material*

H (A/m)	B (T)	H (A/m)	B (T)
0	0	2000	1.367
30	0.69	4000	1.488
40	0.85	5000	1.508
60	1	7000	1.58
70	1.04	9000	1.65
90	1.09	10000	1.67
200	1.167	30000	1.82
300	1.21	50000	1.85
500	1.234	70000	1.88
800	1.27	90000	1.905
1000	1.284	100000	1.917

Figure A.5 shows the core loss curves of 10JNEX900 material at 400Hz and 1kHz [23].

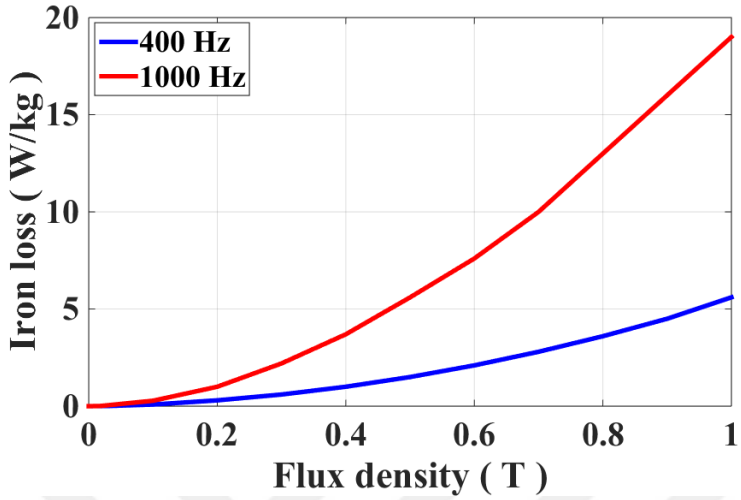

Figure A.5. The core loss curves of 10JNEX900 material

Figure A.6 provides a comparison of the B-H curves of M36 steel and 10JNEX900 material.

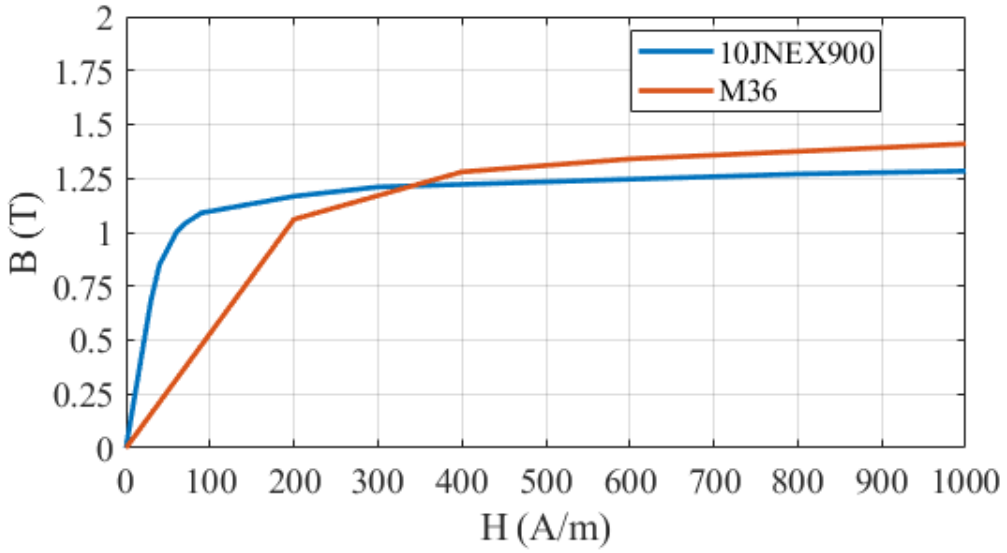

Figure A.6. B-H curves of M36 steel and 10JNEX900 material